Dynamics of water circulation and anthropogenic activities in paddy dominant watersheds : From field-scale processes to catchment-scale models

Dynamics of water circulation and anthropogenic activities in paddy dominant watersheds

— From field-scale processes to catchment-scale models —

Takeo Yoshida

Hydrology and Water Resources Management, Hydraulic Engineering Research Division

Abstract

Irrigation in Japan accounts for 70% of total water diversion and is predominantly used for rice cultivation. Water movement within irrigated areas is complicated not only by the substantial volumes involved but also by repeated cycles of diversion and return flow, by which diverted water gradually drains from irrigated areas. Thus, understanding tivater use and its management is crucial for characterizing flow regimes in watersheds where irrigated paddies predominate. Recent changes in our natural and social environments are increasing the vulnerability of the water resources used for rice irrigation, which has been designed and operated under the assumption of stationarity. Distributed hydrological models have often been used to assess the vulnerability of water resources. However, although the importance of such assessments in analyzing anthropogenic water use in catchment-scale hydrological systems is being increasingly recognized, few models have attempted to incorporate the dynamics of water circulation associated with rice paddy irrigation. A model suitable for assessing water resources for rice irrigation must have the following capabilities. First, it must simulate water movements within irrigated rice fields, including water diversion from rivers, allocation through channels, and return flow from irrigated areas. Second, it should represent natural hydrological cycles in the whole watershed and should, integrate natural and anthropogenic water movement within the watershed.

In this thesis, the author presents an integrated model that couples catchment-scale natural hydrological cycles and human-related water cycles in irrigated paddy areas; hereafter the catchment-scale water circulation model. The main objective of model development is to assess the interaction between human-related and natural water cycles, especially in watersheds where densely irrigated paddies are dominant. Chapter 2 introduces the base model for this study. The base model simulates the interaction between catchment-scale hydrological cycles and paddy water uses. The author also traces some of the shortcomings of the base model and outlines the concept of the new model. In Chapter 3 presents the core issue of this thesis to be addressed: the representation of water circulation in densely developed irrigated paddy areas, and the integration of this model with natural hydrological cycles. The newly developed model is applied to a typical watershed in which irrigated paddies are dominant in Japan, and the interaction between natural and anthropogenic water cycles are evaluated. In Chapters 4 and 5, for extend the applicability of the new model, sub-models for snowmelt and flood inundation processes are introduced and validated. Finally, in Chapter 6, the catchment-scale water circulation model is applied to three experimental watersheds, each of which is donunated by different land uses and cultivation statures: namely cultivated paddies, abandoned paddies, and forest. We then discuss the ability of the new model to reproduce the hydrological changes associated with physical changes in paddy conditions.

The concepts in the model should contribute to ongoing discussions on how to incorporate anthropogenic impacts into distributed hydrological models. There are two potential beneficiaries of this model: the climate-change impact-assessment community and managers of water resources in paddy-dominant watersheds. A number of studies have examined the impacts of climate change on water resources. However, the effects of anthropogenic water cycles in paddy-dominant watersheds have not yet been examined explicitly, and thus the impact of climate change on paddy water-use systems is not fully understood. The proposed model calculates both natural and anthropogenic water cycles in watersheds. It thus provides not only stream flow changes, but also the potential effects of climate change on reservoir storages and the amounts of water diverted for paddy irrigation. Also, the model has the potential to contribute to water resources management, especially in watersheds undergoing rapid societal change. The expected societal changes in paddy-dominant watersheds in Japan will lead not only to an increase in the number of abandoned paddies, but also to increases in the number of crop varieties used and the length of irrigation periods, or increases in water demand due to changes in field water management. Moreover, in developing countries in the Asian Monsoon region, the area under irrigation and the number of reservoirs being developed are increasing at a tremendous rate. This model should be highly useful in the planning for optimum management of such watersheds.

Keywords : *catchment, distributed hydrological model, rice paddies, irrigation, water resources*

CONTENTS

1. Introduction

1.1 Background

Irrigation in Japan accounts for 70% of the total water diversion and is used predominantly for rice cultivation. Water movement within irrigated areas is complicated not only by the substantial volumes involved but also by repeated cycles of diversion and return flow, when diverted water gradually drains from the irrigated areas. Understanding the dynamics of return flow is crucial for characterizing flow regimes in watersheds where irrigated paddies predominate.

Recent changes in our natural and social environments are in creasing the vulnerability of the water resources used for rice irrigation, which uses systems that were designed and are operated under the assumption of stationarity (Milly et al., 2007). Distributed hydrological models are often used to assess the vulnerability of water resources. However, although the importance of such assessments in analyzing anthropogenic water use in catchment-scale hydrological systems is being increasingly recognized, few models have attempted to incorporate the dynamics of water circulation associated with rice paddy irrigation.

A model suitable for assessing water resources for rice irrigation must have the following capabilities. First, it must simulate water movements within irrigated rice fields, including water diversion from rivers, its allocation through channels, and the return flow from irrigated areas. Second, it should also represent natural hydrological cycles in the whole watershed and should integrate natural and anthropogenic water movements within the watershed.

In this thesis, I presents an integrated model that couples catchment-scale natural hydrological cycles with human-related water cycles in irrigated paddy areas. The main objective was to produce a model that could be used to assess the interaction between the human-related and natural water cycles, especially in watersheds where densely irrigated paddies are dominant. In addition, to extend the applicability of the model to a broad range of hydrological conditions, several sub-models were developed for representing flooding and snow-melting

processes and subsequently integrated into the catchment-scale water circulation model.

1.2 Previous research on modeling watersheds with rice paddy irrigation

1.2.1 Distributed hydrological models and their application in water resources assessment

Hydrological models are categorized into lumped models and distributed models according to how they spatially represent hydrological processes. Lumped models are developed to predict stream flow at a point of interest in a watershed based on the storage-discharge relationships. In contrast, Freeze and Harlan (1969) proposed that various hydrological processes could be represented by distributed hydrological models, in which catchment-scale hydrological cycles are modeled by combinations of equations based on laboratory results or plot-scale observations.

Numerous models based on the proposals of Freeze and Harlan (1969) have been developed, including SHE (Abbot et al., 1986) and IHDM (Calver and Wood, 1995). These distributed models are based on well-understood small-scale (local) processes (e.g., Richards' equation to describe flow in porous media), but they can be used to quantify large-scale processes (e.g., base-flow recession at the outlet of a catchment), as long as equivalent or effective values of scale-dependent (flow and transport) parameters can be identified. However, many of the needed parameters are not directly measurable, nor can they be determined by automated procedures, because hydrological modeling is subject to equifinality, which means that hydrological processes can potentially be well represented by multiple sets of parameters. Therefore, even models that produce a full physical representation of a hydrological system do not necessarily contribute to our understanding of complicated hydrological processes in watersheds (Beven, 2011).

Low-dimensional distributed models attempt to simulate hydrological cycles in a relatively simplified manner with only a few degrees of freedom. However, if the major processes that govern a watershed's hydrological cycles are not appropriately represented by such models, the perceived hydrological cycles may be false. An example of a low-dimensional model is TOPMODEL (Beven and Kirkby, 1979). Topographic similarity plays a crucial role in hydrological modeling with this model. TOPMODEL uses a topographic index of hydrological similarity for different points in a watershed, determined by analyzing topographic data. This index is calculated as $\ln(a/\tan \beta)$, where a is the area draining through a point from upslope and $\tan \beta$ is the local slope angle. A higher index value at a point means that the upslope contributing area is larger and the slope gradient is lower, and thus the soil is more likely to be saturated. In addition, Boorman et al. (1995) proposed a hydrological classification scheme for soil types of the UK that makes use of the fact that the physical properties of a catchment's soils, and the soil structure in particular, have a major influence on the catchment hydrology. Such semi-distributed models are easier to implement and require much less computer time than fully distributed models, and as a result, they have been applied to real-time flood forecasting and assessment studies of the impacts of climate change (Bell and Moore, 1998; Bell et al., 2009).

In addition, advances in computational and remote sensing techniques, by making it possible to assess water resources at large scale and in sparsely observed watersheds, have led to global-scale modeling of water resources. Fujihara et al. (2008) evaluated the impact of climate change on water resources, focusing on agricultural water use in a watershed in Turkey. Global models have been developed for assessing water resources, water trade, and climate change (Hanasaki et al.,2008a, 2008b; Rost et al.,2008). In those models, however, agricultural water use is simulated mainly for upland crops, and water flows in watersheds in humid climates where irrigated rice paddies are prevalent are not represented.

1.2.2 Catchment-scale interactions between rice paddy irrigation and hydrological cycles

Water-balance methods have been used to evaluate basic properties of water movement in irrigated paddies. For example, Okamoto (1973) proposed a water-balance method, called the critical block method, for evaluating actual water usage and return flow in irrigated paddy areas. However, water-balance approaches are based on observations of inflow and efflux within irrigated areas; hence, the scale at which they can be applied is limited, because even in small irrigated areas continuous observations at multiple influx and efflux points are laborious. Their application is also limited by the assumption of steady-state conditions, characterized, for example, by little rainfall and a constant intake of water for irrigation. In addition, the available water-balance methods were not designed to evaluate the interaction between natural and anthropogenic water flows but only to estimate the necessary water demand for irrigated areas.

Analytical methods that employ time series of measured river flows at multiple points in a watershed in which both water diversion and return flow takes place have been developed to evaluate time-variant water diversion and return flow (Shiraishi et al. 1976; Tanji, 1986). Although these approaches are quite effective for estimating the current status and time-variant nature of internal states within an irrigated area and for evaluating interactions between rivers and irrigated areas, they do not represent the physical structure of irrigated areas.

Hence, they cannot be used to properly assess the impacts of natural or social watershed changes on watershed environments.

To physically represent hydrological processes within watersheds with heterogeneous land uses and land covers, Maruyama et al. (1979) and Tomita et al. (1979) have proposed the complex tank model, a lumped model in which multiple tanks are used to account for rainfall-runoff processes from each land use or cover type. Nakagiri et al. (1998, 2000) extended this approach to evaluate the return flow of diverted water in a watershed with a highly developed irrigated system in Japan. However, lumped models generally require model parameters to be calibrated by using time series of river discharge data. Therefore, their application is limited to extensively observed watersheds. To quantify return flow in ungauged watersheds, a full understanding of the cumulative effects of natural and anthropogenic water interactions is needed.

Distributed hydrological models have been developed to model Japanese rivers strongly influenced by anthropogenic activities, including rice paddy irrigation (Goto, 1983), as well as to model the wide variety of rice cultivation systems in use in the Mekong River basin, which is a typical large watershed of the Asian monsoon region (Taniguchi et al., 2009a, 2009b, 2009c; Masumoto et al., 2009). Because these models do not only represent hydrological cycles in the watershed but also simulate spatial and temporal variations in planting area and water use, they can be used to evaluate the interaction between natural and anthropogenic water use cycles. However, most rice paddies in the Mekong River basin are rainfed or irrigated from small irrigation facilities. As a result, those models simulate water flows associated with each irrigated paddy area within a single grid cell. In addition, reservoir operations in the watershed are not fully implemented, although they can strongly impact flow regimes in highly developed watersheds.

To explicitly represent anthropogenic water flows in watershed with highly developed rice paddy irrigation systems, a model able to represent water diversion, allocation, and return flow within irrigated paddy areas is required. Moreover, such a model could be used to evaluate the interaction between natural and anthropogenic water flows as well as to assess the impacts of recent changes in the natural and social environment on the vulnerability of water resources.

1.2.3 Status of paddy cultivation and runoff characteristics

Watersheds in which paddy cultivation is predominant have different runoff characteristics than pristine watersheds because the water management systems used by rice paddies are unique.

In mountainous areas in particular, rice paddies are typically surrounded by high levees to keep the ponding water level high.

Thus, some portion of the surface runoff during storm events remains in the paddies. If the storage capacity of the paddies is larger than that of the surrounding environment, in fact, paddy areas can fill a flood reduction function by reducing peak flows during floods. However, recent social changes, including abandonment of rice paddy cultivation, have decreased this function of rice paddies (Hayase, 1994).

Changes in runoff characteristics caused by the abandonment of paddy cultivation have been investigated by carrying out fieldscale observations of the physical structures of rice paddies that dominantly account for the changes in runoff characteristics from abandoned paddies, for example, modified soil surface properties, including soil porosity changes and the development of large cracks (Yoshida et al., 1997; Masumoto et al., 1997; Koga et al., 1997), and changes in the height of the levees and outlet of the paddies (Hayase et al., 1992).

Moreover, several studies have modeled such field-scale changes of paddies (Chiba et al., 1997; Masumoto et al., 2003). Physically based hydrological models, which are able to take such changes into account, are particularly useful for predicting changes in flow regimes caused by changes of land use and land cover. However, watershed-scale observations of runoff characteristics that focus on changes of land use and management are rare, although Tanakamaru and Kadoya (1994 a, 1995b) investigated differences in long-term runoff characteristics due to farm land reclamation in Japan.

1.3 Objective and methods

The objective of this thesis is to present an integrated model, called the distributed water circulation model incorporating agricultural water use (DWCM-AgWU) that couples watershed-scale hydrological cycles and human-related water cycles in irrigated paddy areas. The integrated model was developed as follows:

1) To represent water management in paddy fields, the model developed by Taniguchi et al. (2009a, 2009b, 2009c) for the Mekong River basin was used as a base model. In particular, two modules from this base model were used, the cropping pattern and area module and the paddy water use module. The first simulates spatial and temporal variations in the planting area and the second simulates water use within each model grid cell.

2) To explicitly represent human-related water flow in a watershed predominated by irrigated rice paddies, including reservoir management for irrigation, allocation of diverted water to large irrigated paddies, and return flow from irrigated paddies to rivers, a new water allocation and management module was

developed. What is novel about this module, and the core theme of this thesis, is that it represents water fluxes across multiple grid cells.

3) To assess the interaction between hydrological characteristics and paddy conditions, the integrated model's ability to reproduce differences in runoff characteristics between a watershed with highly developed irrigation systems and a mountainous watershed in which terraced paddy fields are prevalent was investigated. To represent near-surface hydrological processes in abandoned paddies in mountainous watersheds, a sub-module was developed and incorporated into DWCM-AgWU.

4) To extend the applicability of the model to a broader range of hydrological conditions, snowfall/snowmelt and flood inundation modules were developed and integrated into the main model.

1.4 Thesis outline

Section 2 introduces the base model, which simulates water use associated with both rice paddy irrigation and watershed hydrological cycles. Some of the shortcomings of the base model are described, and the conceptual basis of the new model is outlined. Section 3 presents the core theme of this thesis: the water allocation and management module, which represents water circulation in densely developed irrigated paddy areas and its integration with natural hydrological cycles. The newly developed model with this new module is applied to a typical watershed in Japan in which irrigated paddies are dominant, and the interaction between natural and anthropogenic water cycles in the watershed are evaluated. In Sections 4 and 5, the applicability of the new model is extended by introducing and validating modules for snowmelt and flood inundation processes. Finally, in Section 6, the developed model is applied to three experimental watersheds, each of which is dominated by different land uses and cultivation statuses: namely, cultivated paddies, abandoned paddies, and forest. Then, the ability of the new model to reproduce the hydrological changes associated with physical changes in paddy conditions is discussed.

2. Structure of the base model and novel concepts in the newly developed model

2.1 Introduction

This section describes the structure of the base model and some of its shortcomings (Taniguchi et al., 2009a, 2009b, 2009c), along with the modifications and novel concepts introduced in developing the new model.
 While the calculation time step dt is a day, we shorten the time step (e.g., to 1 h) in the module that simulates the generation of surface runoff (2.2.1.2) and routing of surface and stream flow (2.2.1.3). It should be noted that in the description of the base model, the spatial and temporal dimensions of the variables are omitted because each calculation is completed within a single grid cell and time step.

2.2 Basic structure of the base model

The base model consists of four modules: runoff, actual evapotranspiration, cropping pattern and area, and paddy water use. The base model can simulate both natural and anthropogenic water flow. The hydrological components of the catchment are represented in a grid cell composed of three conceptual soil layers: the root zone, the unsaturated zone, and the saturated zone (**Fig. 1**). There are various land uses associated with each grid cell, and the model simulates the generation of surface runoff and actual evapotranspiration (ET) for each land use type. Then, actual ET (Allen et al., 1998), the amounts of overland flow and agricultural water use are calculated for the whole grid cell . The generated surface runoff is routed by using a one-dimensional kinematic wave for channel flow (Li et al., 1975) so that the daily flow rate can be calculated at any point of interest.

2.2.1 Runoff module
(1) Water fluxes and storage in a grid cell

The grid cells are dynamically connected by various processes, including surface runoff, vertical drainage, and water fluxes via surface and subsurface flow pathways. The maximum capacity of root zone storage in each grid cell S_{rmax} (mm) is calculated as the areal average of the storage for each land use type. The change in the root zone storage S_r (mm) is calculated from the water budget as follows:

$$\frac{dS_r}{dt} = I - E_a - Q_v, \tag{1}$$

where I is infiltration rate (mm/dt), E_a is actual evapotranspiration (mm/dt). Each term in (1) will be discussed in more detail later.
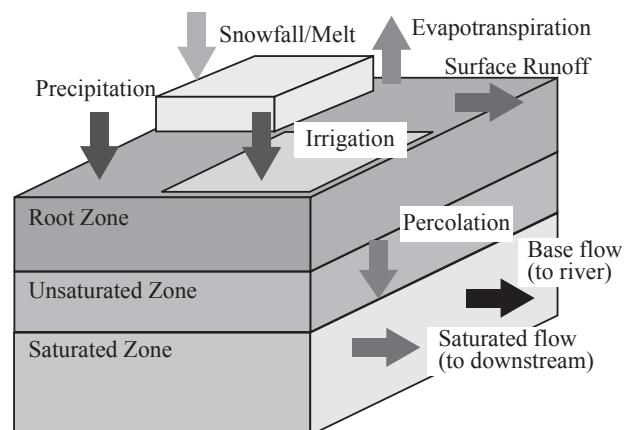

Fig. 1 Storage and runoff structure in a grid cell

Vertical drainage by gravity is generated when S_r exceeds S_{rmax}. Although the base model assumes that all vertical drainage reaches the saturated zone immediately after it is generated, the new model assumes gradual water movement and accounts for the time delay by introducing unsaturated zone storage. Q_v (mm/d) is estimated by the following equation (Beven and Wood, 1983):

$$Q_v = \begin{cases} \dfrac{S_u}{D_s T_d} & (D_s > 0) \\[2mm] \dfrac{1}{T_d} & (D_s = 0), \end{cases} \tag{2}$$

where S_u is storage in unsaturated zone (mm), D_s is the water deficit in saturated zone (mm), and T_d is a parameter to account for the time delay (dt/mm). The fraction of water that does not reach the saturated zone remains in the unsaturated zone.

$$\frac{dS_u}{dt} = \begin{cases} S_r - S_{rmax} - Q_v & (S_r > S_{rmax}) \\[2mm] -Q_v & (S_r < S_{rmax}) \end{cases} \tag{3}$$

Water flux from the saturated zone has two components: lateral flux Q_b (m³/dt) and direct runoff to river channel Rc (m³/dt). Thus, the water budget of the saturated zone is calculated by the following equation:

$$\frac{dD_s}{dt} = Q_v - Q_b - R_c \tag{4}$$

The lateral flux Q_b is simulated by assuming that the flux decreases exponentially with storage in the saturated zone and that it flows in the direction of the surface flow and slope (equation (5)).

$$Q_b = Q_{b0} \exp(-D_s/f_b) S_c L_s, \tag{5}$$

where Q_{b0} is the water flux when the saturated zone is full (m²/dt), S_c is the surface slope, L_s is the length of the grid cell(m), and f_b is the recession parameter (mm).

The base flow is estimated by assuming the storage in the saturated zone. The base model generates base flow when the storage in the saturated zone exceeds a certain threshold, whereas the modified model assumes that the generation of base flow is continuous:

$$R_c = R_{c0} \exp(-D_s/f_r) L_c, \tag{6}$$

where R_{c0} is the base flow when the saturated zone storage is full (m²/dt), f_r is a recession paramter (mm), L_c is the river length within the grid-cell (m).

(2) Generation of overland flow
Overland flow is assumed to be generated by two processes: infiltration excess overland flow occurs during heavy rainfall, and saturation excess overland flow occurs around wet riparian zones.

Infiltration excess overland flow is generated when the rainfall intensity p_t (mm/dt) exceeds the infiltration rate f (mm/dt), which is calculated with the Green-Ampt

equation (Green and Ampt, 1911). The changes in infiltration rate f in one calculation time step (from time t to t+dt) is estimated as follows (Chow et al., 1988). First, the current potential infiltration rate f_t is calculated from the known value of cumulative infiltration F_t (mm) .

$$f_t = K_{sat}\left(\frac{\psi\Delta\theta}{F_t} + 1\right), \tag{7}$$

where K_{sat} is hydraulic conductivity (cm/dt), ϕ is the suction of wetting front (mm), and effective porosity $\Delta\theta$ = 1 - S_r/S_{rmax}. The resulting value of f_t is compared to the rainfall intensity p_t (mm/dt). If f_t is less than or equal to p_t overland flow is generated throughout the calculation time step.

In contrast, if f_t is larger than p_t and there is no ponding at the beginning of the time interval, it is assumed that no ponding will occur throughout the interval; then, the infiltration rate is f_t and the tentative cumulative infiltration value at the end of the time interval is

$$F'_{t+dt} = F_t + p_t dt \tag{8}$$

Next, the corresponding infiltration rate f'_{t+dt} is calculated from F'_{t+dt}. If F'_{t+dt} is greater than p_t, there is no ponding throughout the interval. Thus, $F_{t+dt} = F'_{t+dt}$ and the problem is solved for this interval.

If f'_{t+dt} is less than or equal to p_t, ponding occurs during the interval. The cumulative infiltration F_p at the ponding time is found by setting $f_t = p_t$ and $F_t = F_p$ in equation (7) and solving for F_p to give, for the Green-Ampt equation,

$$F_p = \frac{K\psi\Delta\theta}{p - K} \tag{9}$$

Excess rainfall is calculated by subtracting cumulative infiltration from cumulative rainfall.

Saturation excess overland flow occurs in completely saturated grid cells: that is, $S_r = S_{rmax}$ and $D_s = 0$. Once the grid cell meets these conditions at time t, all precipitation p_t becomes saturation excess overland flow; if these conditions are met after the beginning of the time interval, then the precipitation that falls after they are met becomes overland flow.

(3) Routing scheme for overland flow
The flow routing module is configured to convert estimates of overland runoff to river flow with a delay associated with surface flow in the grid cells. The routing scheme is based on a discrete approximation of a one-dimensional kinematic wave equation with lateral inflow that relates channel flow Q (m³/s) to lateral inflow per unit length of the river q (m²/s).

$$\frac{\partial A}{\partial t} + \frac{\partial Q}{\partial x} = q \tag{10}$$

$$A = KQ^P, \tag{11}$$

where A is cross-section of the channel (m²), and K and P are parameters that are determined for each of sub-

watershed from the channel width and average slope of the sub-watershed.

In the base model, the routing scheme uses a 5-day moving average of generated overland flow to account for the delay caused by surface flow in a grid cell with a length of 10 km (Taniguchi et al., 2009c); however, the averaging period must be objectively determined. Thus, to account for the delay, the new model assumes that overland flow in the grid cells can be schematically represented by a channel between two slopes. The generated overland flow r_e (m/dt) is then treated as flow on the slopes.

$$\frac{\partial h}{\partial t} + \frac{\partial q}{\partial x} = r_e \qquad (12)$$

$$h = kq^p, \qquad (13)$$

where h is water depth (m), and k and p are flow parameters. Parameter k is represented as $k = (N/\sqrt{s})^p$, where N is a friction parameter and s is the gradient of slope. The standard value of N are 1.5 (sm$^{-1/3}$) for forest, 0.4 (sm$^{-1/3}$) for upland fields, and 2.5 (sm$^{-1/3}$) for rice paddies, and p is normally set to 0.6. The gradient of slope s is estimated with the standard deviation of elevation in the grid-cells S_{elv}. Here, a digital elevation map with a spatial resolution of 50 m was used to calculate s as $s = 2 \times S_{elv}/L_c$.

Equation (10) can be expressed by the following finit-edifference equation:

$$\frac{A_{i+1}^{j+1} - A_{i+1}^j}{dt} + \frac{Q_{i+1}^{j+1} - Q_i^{j+1}}{dx} = \frac{q_{i+1}^{j+1} + q_{i+1}^j}{2} \qquad (14)$$

This equation has been arranged so that it can be numerically solved for the unknown discharge Q_{i+1}^{j+1}. Li et al. (1975) performed a stability analysis and showed that the scheme using equation (14) is unconditionally stable. They also showed that a wide range of values of dt/dx could be used without introducing large errors in the shape of the discharge hydrograph.

2.2.2 Cropping pattern and area module

Because a wide variety of water use and irrigation systems are used in the Mekong River basin, the base model represents temporal and spatial differences in the planting pattern and area used for rice. To do this, it categorizes rice paddies into four classes: namely, rainfed without supplemental irrigation, rainfed with supplemental irrigation, irrigated, and flood utilization paddies. It also categorizes irrigation systems into six classes: namely, gravitational, pump, reservoir, colmatage, groundwater, and tidal irrigation. Rice varieties are also grouped into two classes: photosensitive and non-photosensitive rice. Please see Taniguchi et al. (2009) for details regarding the planting pattern and area module.

The basic idea of the planting pattern and area module is that the planting starts when required water P_{cum}

(mm) is supplied to paddies, and the planted area steadily increases once planting begins:

$$A_c = A_p \frac{D}{T_{tra}}, \qquad (15)$$

where A_c is the actual planted area (m^2), A_P is the potential planted area for rice in each grid cell (m^2), D is the number of days elapsed since the start of transplanting, and T_{tra} is the duration (days) of the transplanting period .

2.2.3 Actual ET module

The actual ET module calculates ET from the land surface by using the reference ET (E_{T0}) estimated by the Modified Penman-Monteith equation (Allen et al., 1998).

$$E_{T0} = \frac{0.408\Delta(R_n - G) + \gamma \dfrac{900}{T_a + 273} U(e_s - e_a(T_a))}{\Delta + \gamma(1 + 0.34U)}, \qquad (16)$$

where, R_n is net radiation (MJ/m^2/dt), G is ground heat flux (= 0) (MJ/m^2/dt), U is wind speed (m/s), T_a is air temperature (℃), e_s is saturated vapor pressure (kPa), e_a (T_a) is vapor pressure at temperature T_a (kPa), Δ is the slope of saturation vapor pressure curve (kPa/℃), γ is psychrometeric constant (kPa/℃). The detailed procedure for calculating each term of equation (16) is described in appendix of this section.

Actual ET (E_a) is estimated from the areal average of each land use type in the grid cell:

$$E_a = \frac{E_l A_l + E_w A_w}{A_{gc}}, \qquad (17)$$

where A_{gc}, A_{wt}, A_l are areas of the grid cell, water surface and land surface areas (m^2), and E_w is evaporation from water surface(= E_{T0}). Evapotranspiration from land surface E_l (mm/d) is the averaged value from land use i:

$$E_l = \sum_i K_c(i, t) \frac{A(i)}{A_c} \frac{S_r}{S_{rmax}} E_{T0}, \qquad (18)$$

where crop coefficient $K_c(i, t)$ is a function of the land use i and time t; its value is 1.1 for planted paddies and forest, 0.6 for upland crops, and 0.3 for non-planted paddies (Allen et al., 1998).

2.2.4 Paddy water use module

The paddy water use module simulates the water supply to and runoff from the paddies; here, the ponding depth of the paddies governs the entire process. The ponding depth is calculated by using the output of planting pattern and area, runoff, and actual ET modules.

The actual water supply to paddies Q_i (m^3/dt) depends on the gross water requirement Q_{gw} (m^3/dt), flow rate in the grid cell Q_{ch} (m^3/dt), and the capacity for diversion Q_{if} (m^3/dt). Because both Q_{ch} and Q_{if} constrain the amount of water farmers can supply to the paddies, Q_i is estimated as follows:

$$Q_i = \min\left(Q_{gw}, Q_{ch}, Q_{if}\right) \qquad (19)$$

The gross water requirement Q_{gw} is calculated from the irrigation efficiency I_e and the net water requirement Q_{nw} (m³/d).

$$Q_{gw} = \frac{Q_{nw}}{I_e} \tag{20}$$

$$Q_{nw} = A_{ia}(ET_a + I_p - p) \times 10^3, \tag{21}$$

where p is precipitation (mm/dt), Ip is infiltration at paddies (mm/dt), E_a is actual ET (mm/dt). The difference between Q_{gw} and Q_{nw} is regarded as water loss through water allocation in a grid cells; thus, it is water supplied to the root zone.

The ponding depth of the paddies is estimated from the actual water supply Q_i as follows:

$$\frac{dH_p}{dt} = p - I_p - E_{Tpad} - H_{pout} + Q_i/A_{ia} \times 10^{-3}, \tag{22}$$

where H_{pout} (mm/dt) is flow out of the paddies, which is calculated with overflow weir formula.

2.3 Novel concepts introduced in the new model

The base model simulates the planting pattern and water uses of rice paddies (**Fig. 2**). Because the base model was developed for application to the Mekong River basin, where most rice paddies are rainfed and irrigation reservoirs when present are small, complex irrigation systems covering multiple grid cells and large reservoirs are not modeled.

The new model represents not only processes applicable to individual grid cells but also water fluxes across multiple grid cells. The included water fluxes are flows from reservoirs for irrigation, diverted water flows allocated to large irrigated paddies, and return flows from irrigated paddies to rivers. In particular, representation of water fluxes across multiple grid cells is essential for assessing the return flow of diverted water from large irrigated areas. A distinguishing characteristic of the new model is that these components are managed in a unified manner by a water allocation and management module (**Fig. 2**; see Section 3).

2.4 Summary

This section describes the basic structure of the four modules that compose the base model, and the novel concepts introduced during new model development. The base model and the novel aspects of the new model can be summarized as follows:

1) The base model simulates planting patterns and areas and water use in rice paddies, including its interaction with natural hydrological cycles in a river basin where rice paddies are prevalent. The model explicitly represents water cycles in paddy areas as well as natural hydrological cycles, thus enabling water management for irrigated paddies to be assessed.
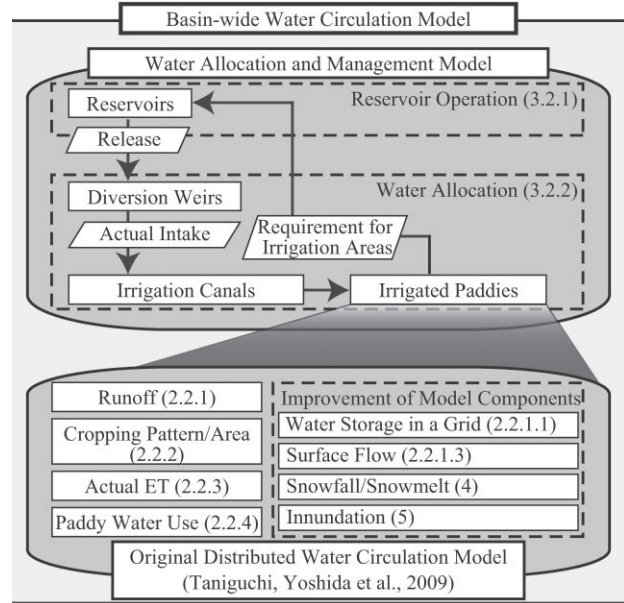
2) In addition to the processes represented in the base

Fig. 2 Structure of the distributed water circulation model (base model) incorporating the new water allocation and management module (Numbers in the figure indicate corresponding sections in this paper

model, the new model accounts for water fluxes, including flows from reservoirs for irrigation, diverted water flows to large irrigated paddies, and return flows from irrigated paddies to rivers. To simulate such anthropogenic water flows in a unified manner, a new water allocation and management module was developed. This module is described in the next section.

Appendix 2: Calculation of Reference Evapotranspiration

The variables used in the equation (16) are calculated by the following equations (Allen et al., 1998).

$$\Delta = \frac{4098 \times 0.6108 \exp\left(17.27 T_a/(T_a + 237.3)\right)}{(T_a + 237.3)^2} \tag{23}$$

$$\gamma = 0.065 \times 10^{-3} P_{atm} \tag{24}$$

$$P_{atm} = 101.3 \left(\frac{293 - 0.0065z}{293}\right)^{5.26} \tag{25}$$

$$e_a = \frac{e^0(T_n)(H_n/100) + e^0(T_x)(H_x/100)}{2} \tag{26}$$

$$e_s = \frac{e^0(T_x) + e^0(T_n)}{2}, \tag{27}$$

where P is atmospheric pressure (kPa), z is elevation (m), H_x and H_n are daily maximum and minimum of relative humidity (%), and T_x and T_n are daily maximum and minimum of temperature (℃). Saturated vapor pressure e_0 (T) (kPa) for a given temperature T is estimated with e_0 $(T) = 0.6108 \exp((17.27T)/(T+ 237.3))$.

Net radiation R_n is calculated as follows:

$$R_n = R_{ns} - R_{nl} \tag{28}$$

$$R_{ns} = (1 - \alpha)R_s \tag{29}$$

$$R_{nl} = \sigma \left(\frac{TK_n^4 + TK_x^4}{2} \right) \left(0.34 - 0.14\sqrt{e_a} \right)$$
$$(1.35R_s/R_{s0} - 0.35), \tag{30}$$

where R_{ns} is net short-wave radiation (MJ/m^2/d), R_{nl} is net longwave radiation (MJ/m^2/d), α is albedo (= 0.23), R_s is shortwave radiation (MJ/m^2/d), R_{s0} is clear-sky short wave radiation (MJ/m^2/d), TK_n and TK_x are minimum and maximum temperature (K), and σ is Stefan-Boltzmann constant (= 4.903 x 10^{-9}(MJ/K^4/m^2/d)).

$$R_{s0} = \left(0.75 + 2 \times 10^{-5}z \right)R_a \tag{31}$$

$$R_s = 0.16\sqrt{T_x - T_n}\,R_a \tag{32}$$

$$R_a = \frac{24 \times 60}{\pi}d_r \left(\omega\sin\phi\sin\sigma + \cos\phi\cos\sigma\sin\omega \right) \tag{33}$$

$$d_r = 1 + 0.033\cos\left(\frac{2\pi}{365}D \right) \tag{34}$$

$$\delta = 0.409\sin\left(\frac{2\pi}{365}D - 1.39 \right) \tag{35}$$

$$\omega = \arccos\left(-\tan\phi\tan\delta \right), \tag{36}$$

where R_a is extraterrestrial radiation (MJ/m^2/d), d_r is inverse relative distance Earth-Sun, ω sunset hour angle (rad), ϕ is latitude (rad), δ is solar delination (rad), D is julian day.

3. Modeling of water circulation in river basins possessing large areas of irrigated paddy by incorporation of a water allocation and management module

3.1 Introduction

Section 3 presents the core of this thesis: the representation of water circulation in densely developed irrigated paddy areas and its integration with the natural hydrological cycle. Then the newly developed model, DWCM-AgWU, is applied to a typical watershed in Japan in which nearly 20% of the watershed is irrigated paddies, and the interaction between natural and anthropogenic water cycles is evaluated.

DWCM-AgWU consists of five modules: water allocation and management, planting pattern and area, paddy water use, actual evaporation, and runoff. Two modules from the base model are employed to represent spatial and temporal variations in planting area and water use in a watershed, namely, the cropping pattern and area and paddy water use modules. In the new model, however, a novel approach that represents water fluxes over multiple grid cells is used, and the development of this approach is the core theme of this thesis. The included water fluxes are flows from reservoirs for irrigation, diverted water flows allocated to large irri-

gated paddies, and return flows from irrigated paddies to rivers.

Although the default calculation time step dt is one day, the time step can be shortened (e.g., to 1 hour) in the reservoir operation scheme (3.2.1). It should be noted that the spatial and temporal dimensions of each variable are omitted because each calculation is completed within a single grid cell and time step.

3.2 Structure of water allocation and management module

The components included in the water allocation and management module of DWCM-AgWU are schematically illustrated in **Fig. 3.** The water allocation and management module has two major schemes, namely, a reservoir operation scheme and a water allocation scheme.
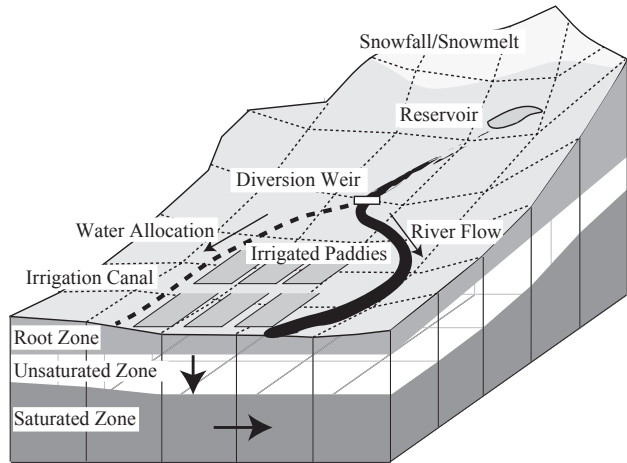

Fig. 3 Schematic representation of components of the water allocation and management module in irrigated paddy areas.

3.2.1 Reservoir operation scheme

The reservoir operation scheme is used to estimate releases from the reservoir to diversion weirs for irrigation (Horikawa et al., 2011). Typical water releases from a reservoir, such as releases for hydropower generation or releases of excess water via a spillway, are simply calculated from the inflow into the reservoir and its storage capacity. In contrast, for calculation of irrigation releases, flow rates at the diversion weirs must be taken into account, because the amount of water released must be enough to meet the water demand at the downstream diversion weirs when the flow rates at those weirs are less than the water demand.

The scheme is based on the water balance in the reservoir:

$$V_r(t) = V_r(t - 1) + Q_{rin}(t) - Q_{rout}(t), \tag{37}$$

where $Q_{rin}(t)$ and $Q_{rout}(t)$ are the inflow and release of water (m^3/dt), and $V_r(t)$ (m^3) is the storage in the reservoir at time t (day). The total amount of water released

from the reservoir is estimated by summing the amounts released for different reasons:

$$Q_{\text{rout}}(t) = Q_{\text{ru}}(t) + Q_{\text{spill}}(t) + Q_{\text{rf}}(t), \tag{38}$$

where $Q_{\text{ru}}(t)$, $Q_{\text{spill}}(t)$, and $Q_{\text{rf}}(t)$ (all m^3/dt) are the amounts released for water use, as spillway flow, and to maintain the minimum required environmental flow, respectively.

(1) Release for water use

Release for water use from reservoirs $Q_{\text{ru}}(t)$ are the sum of amounts released for irrigation $Q_{\text{ri}}(t)$, domestic use $Q_{\text{rd}}(t)$, and hydropower generation $Q_{\text{rp}}(t)$ (all m^3/dt).

$$Q_{\text{ru}}(t) = Q_{\text{ri}}(t) + Q_{\text{rd}}(t) + Q_{\text{rp}}(t) \tag{39}$$

a) Release for irrigation

 Water required for irrigation $Q_{\text{ri}}(t)$ (m^3/dt) is released to fulfill the water deficit at diversion weirs, when the water demand at the diversion weir Q_{wr} (m^3/dt) exceeds the available river flow at the weir Q_{rsf} $(t - 1)$ (m^3/dt). Thus, $Q_{\text{ri}}(t)$ is their difference:

$$Q_{\text{ri}}(t) = Q_{\text{wr}} - Q_{\text{rsf}}(t - 1) \tag{40}$$

Although the water demand at the diversion weir varies temporally, Q_{wr} is assumed by the model to be equal to the maximum diversion capacity of the weir.

 Typically, the ratio of river flow to total water diversion in irrigation areas in Japan is relatively large, compared with the ratio in other countries, both because the distance from reservoir to diversion weir is generally relatively long, and because the base flow from the part of the watershed below the reservoir is stable. The amount released for irrigation is thus just the amount of supplemental water needed to meet the difference between the water demand and river flow at the diversion weir.

b) Release for domestic water use

Release for domestic water use is set to a constant as the planned value.

c) Release for hydropower generation

The amount of water released for power generation is calculated as the product of the maximum that can be released for hydropower generation Q_{rpmax} (m^3/dt) and the ratio of storage in the reservoir V_{r} $(t - 1)$ (m^3) on the previous day to the effective storage of the reservoir V_{rmax} (m^3), which is the difference between the maximum and minimum storage volumes.

$$Q_{\text{rp}}(t) = Q_{\text{rpmax}} \frac{V_{\text{r}}(t - 1)}{V_{\text{rmax}}(t)} \tag{41}$$

(2) Release from spillways

Water is released via spillways when the storage in the reservoir exceeds its maximum capacity V_{rmax}. Thus,

when the sum of the storage on the previous day V_{r} $(t- 1)$ and the reservoir inflow $Q_{\text{rin}}(t)$(m^3/dt) exceeds V_{rmax}, $Q_{\text{spill}}(t)$(m^3/dt) is calculated as follows:

$$Q_{\text{spill}}(t) = Q_{\text{rin}}(t) + \frac{V_{\text{r}}(t - 1) - V_{\text{rmax}}}{dt} \tag{42}$$

3.2.2 Water allocation scheme

The water allocation scheme simulates water diversion at the weirs, followed by its allocation to the associated irrigated areas. The estimated amount of diverted water Q_{i} (m^3/dt) is allocated among the modeled irrigation systems along the flow pathways of the irrigation channel networks as described below. Thus, the amount of diverted water is calculated independently of the surface water flows in the runoff module. In the base model, the diverted water is supplied to paddies within the same grid cell, but the new model can simulate water allocation across multiple grid cells.

(1) Extraction of irrigation networks using GIS database

To model water fluxes across large irrigated areas, precise data describing water use facilities and channel networks are needed. These data were obtained from a recently configured GIS database of water use facilities throughout Japan (Japan Institute for Irrigation and Drainage, 2010; data acquired on 2014.5.12). This database includes specifications for irrigation facilities, irrigation channel networks, and irrigation block polygons; the latter two have rarely been incorporated into hydrological models.

The database includes water use facilities (diversion weirs, drainage pumps, and reservoirs) and irrigation and drainage channels that serve an area exceeding 100 ha; the former are represented by point data and the latter by line data. These data have attributes of function and name, and they can be separated or grouped according to their connectivity. However, the database lacks information necessary to link the vector (i.e., point and line) data to the polygon (areal) data of the irrigation blocks. Therefore, an algorithm was developed to link the vector and polygon data for simulation of water allocation to irrigated areas. The algorithm is implemented in two steps. First, an irrigation network is created by linking water diversion facilities (point data) to irrigation channels (line data). Second, the irrigation network is overlaid on the irrigated blocks (polygon data) to link the diversion facilities with their associated irrigated areas. In this way, the spatial extent of each irrigation system is determined, and water allocation to each irrigation area can be simulated.

(2) Water diversion and allocation schemes

First, the amount diverted daily at each diversion weir Q_{i} is determined as the minimum value among the fol-

lowing: daily river discharge $Q_{ch}(m^3/dt)$, designed maximum intake capacity $Q_{if}(m^3/dt)$, and the water requirement of the associated irrigation area $Q_{gw}(m^3/dt)$.

$$Q_i = \min\left(Q_{gw}, Q_{ch}, Q_{if}\right) \qquad (43)$$

Then, Q_i is allocated by dividing it into irrigation water supplied to paddies and management water loss (i.e., the management water requirement). The management water loss, which consists of water that does not reach the irrigated area (paddy fields), gradually returns to streams. In the paddy fields, the irrigation supply is divided into percolation, runoff from fields, and ET. The management water requirement and runoff from paddy fields are passed to the surface runoff module.

The water allocation calculation is independent of the surface runoff calculation. In the runoff module, the flow direction in each grid cell depends on the local topography and the stream flow direction, but in the water allocation scheme, water flow to irrigated areas follows the irrigation channel network. Therefore, the model simulates water allocation to the irrigation areas according to the priority order of the grid cells composing each irrigated block of paddies (here, an irrigated block can be represented by multiple grid cells or by a single grid cell). Paddies in a grid cell in the upper part of an irrigation block that is directly connected to an irrigation channel have a higher priority than those in a grid cell in the lower part of a block that is not directly connected to a channel. Thus, the priority order of each grid cell is determined by 1) its distance from the diversion weir, 2) its distance from an irrigation channel, and 3) its elevation. Water is then allocated to each grid cell following its priority order in the irrigation block according to the water demand in that grid cell Q_{gw}.

The gross irrigation water requirement (mm/d) (i.e., the amount of water that must actually be extracted from the diverted water) is computed by dividing the net irrigation requirement by the irrigation efficiency I_e, which represents the water loss during the distribution and application of the water to the paddies.

$$Q_{gw} = \frac{Q_{rq}A_{ir}}{1,000 \times I_e} \qquad (44)$$

Repetitive use of water within irrigated blocks is not accounted for in this model, and irrigation and drainage channels are assumed to be separate. Hence, the total Q_{gw} in an irrigated area may exceed the diverted amount Q_i, depending on the available river flow. In this case, water is not allocated to grid cells with a low priority order.

Q_{gw} consists of allocated water $Q_a(m^3/dt)(= Q_{rq}A_{ir}/1,000)$ and water loss during allocation $Q_{dr}(m^3/dt)$ (**Fig. 4**). Water lost during allocation returns to the drainage channels within a day (Sato et al., 1998); thus, Q_{dr} is added to the lateral inflow into drainage channels on the day following the allocation. If the sum of water
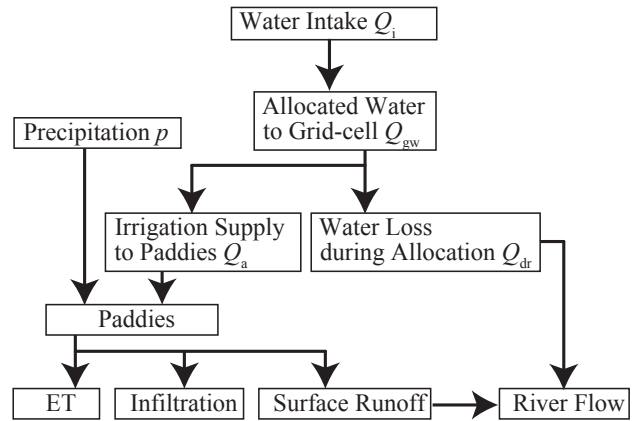

Fig. 4 Schematic diagram of water flows in the water allocation scheme.

allocated to all irrigated grid cells in the irrigated block is less than the total amount of diverted water Q_i, the remainder of the water is distributed equally to all grid cells in the irrigated block or added to the drainage channels via lateral inflow.

For irrigated blocks that consist of a single grid cell, the water diversion and allocation scheme is the same as that of the base model: that is, allocated water Q_a is determined as follows:

$$Q_a = \min\left(Q_{gw}, Q_{ch}, Q_{if}\right) \qquad (45)$$

3.3 Study watershed
3.3.1 Topography, geology and climate of the study watershed

The Seki River basin in central Japan was selected for a case study. The Seki River is 64 km long, and its catchment area is 1140 km². The land cover is dominantly forest (79%), but 17% of the land area of the catchment is agricultural land, mainly rice paddies. The Seki River flows from the Myoko Mountains (highest peak, Myoko Mountain, 2425 m a.s.l.) to the Japan Sea (**Figs.5, 6**). Hillslopes are steep, and the bedrock is a mixture of various Tertiary sedimentary rocks, which are mantled by alluvium. The climate of the basin is humid, typical of the Japan Sea area, and snowfall is heavy in winter. Average annual precipitation is more than 3000 mm, over half of which falls as snow in winter.

3.3.2 Agricultural water use in the basin

The total irrigated area of the basin is approximately 9000 ha, and it is mostly used for rice paddies. There are two major irrigation systems on the eastern side of the Seki River (**Fig. 6**); the Uwae (approximately 2000 ha) and the Nakae (approximately 3000 ha) systems. The Nakae diversion weir was originally located 3 km downstream from the Uwae diversion weir, which led to complex conflicts between the two systems when the conventional water use rule was applied, because Nojiri
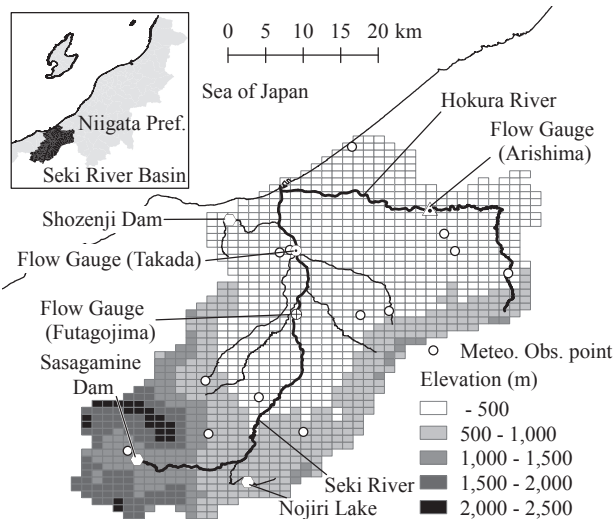
Fig. 5 Location of the Seki River basin (inset), and locations of hydrometeorological observation points in the basin. The grid applied to the study area and its topography are also shown.
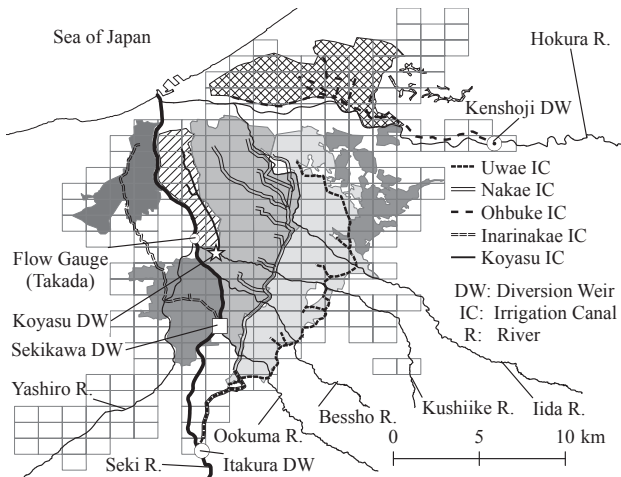

Fig. 6 The major irrigation facilities in the areas served by the Land Improvement Districts of the lower Seki River basin. Different irrigation areas are shown by different hatching patterns and gray shading.

Fig. 7 Photograph of Sasagamine dam looking west. See Fig. 5 for its location.

Fig. 8 Photograph of the Itakura diversion weir looking upstream (north). See Fig. 6 for its location.

Lake (effective storage for irrigation: $9.8 \times 10^6 \mathrm{m}^3$), one of the major irrigation reservoirs, is controlled by the Nakae system. However, the construction of Sasagamine dam $9.2 \times 10^6 \mathrm{m}^3$, **Fig. 7**) and the Itakura diversion weir (**Fig. 8**), which now serves both systems, resolved these conflicts (Shinzawa, 1962). Currently, the Itakura diversion weir not only diverts and allocates water to both the Uwae and Nakae irrigation systems, it also diverts water for hydropower generation. Other irrigation systems shown in (**Fig. 6**) include the Inari-Nakae system on the western side of the Seki River (approximately 600 ha) and the Ohbuke irrigation system along the Hokura River (approximately 1600 ha). Shozenji dam (effective storage $4 \times 10^6 \mathrm{m}^3$, **Fig. 5**) stores water for domestic use.

3.3.3 Collected data and data input procedures

For the model application, the Basic Grid Square (Third Area Partition) of the Standard Regional Mesh Code was used for the grid. In this system, each grid cell covers 45 seconds of arc in the longitudinal direction and 30 seconds of arc in the latitudinal direction, and in central Japan its area corresponds to approximately 1 km². Elevation and land use/cover data for each grid cell were obtained from the National Land Numerical Information website of the Ministry of Land, Infrastructure and Transportation (data acquired on 2014/09/20) and the GIS database of water use facilities in Japan (Japan Institute for Irrigation and Drainage, data acquired on 2014/05/12). The steepest descent method was used to determine the water flow direction in each grid cell, and the direction of river flow in a grid cell was toward the lowest grid cell among the eight neighboring grid cells.

Required meteorological data (precipitation, temperature, humidity, and wind speed) were collected from

1976 through 2008 at existing observation stations (**Fig. 5**). The meteorological data were obtained from the database of the Automated Meteorological Data Acquisition System (Japan Meteorological Agency), the River Bureau of Ministry of Land, Infrastructure and Transport, and the Myoko-Sasagamine Station of the National Institute for Earth Science and Disaster Prevention. To estimate the spatial variation in the observed meteorological variables, the inverse distance weighting method was employed. In this method, the grid cell values are determined by calculating the weighted average of values observed at observation stations in the neighborhood of each grid cell. The closer a station is to the center of the cell being estimated, the greater its weight in the averaging.

Precipitation $p(x)$ (mm/d) in grid cell x was estimated by calculating the average of data from three observation stations, weighted according to the distance from x to the observation station. Then, the ratio of the observed precipitation to the estimated climatic value $r(i)$ (where i = 1, 2, 3) in the grid cell of station i was calculated as follows:

$$r(i) = p_o(i)/p_m(i), \tag{46}$$

where $p_o(i)$ (mm/d) is the observed precipitation at station i and $p_m(i)$ (mm/d) is the climatic value derived from Mesh Climatic Data 2000, which is the monthly climatic precipitation for the corresponding Basic Grid Square (Third Area Partition) estimated from the observed spatial distribution of rainfall from 1971 through 2000 (Japan Meteorological Agency, 2003).

Then, ratio $r(i)$ is interpolated to each grid square of the model by using the inverse distance weighting method as follows:

$$r(x) = \sum_{i=1}^{3} \frac{w(i)r(i)}{\sum_{j=1}^{3} w(j)} \tag{47}$$

$$w(i) = \frac{1}{d(x,i)^2}, \tag{48}$$

where $d(i)$ is the distance from grid cell x to observation station i.

Finally, $p(x)$ is estimated by multiplying $r(i)$ by $p_m(i)$. Ideally, the estimated grid cell x should be located within a triangle formed by the three observation points; however, the same procedure was applied for grid cells outside of such a triangle. Snowfall and snowmelt processes, which were also incorporated in the precipitation estimation, are described in Section 4.. The values of other meteorological variables used for ET estimation were similarly interpolated by using the inverse distance method.

River discharge, which was observed at Takada and Futagojima flow gauge stations (**Fig. 5**) from 2003 through 2008, was used to validate the model. The upstream station (Futagojima) is located immediately

downstream of the largest diversion weir, and the downstream station (Takada) is located near the basin outlet. The recorded data at both stations were affected by both water diversion and return flow.

Actual ET, calculated by the method proposed by Ohtsuki (1984), was used for the adjustment of the root zone storage S_{rmax} so that the actual ET calculated with equation (17) (see Section 2) would equal the Actual ET value. Then, the annual water balance at Takada station was calculated, and areal precipitation was corrected to satisfy the water balance of the watershed.
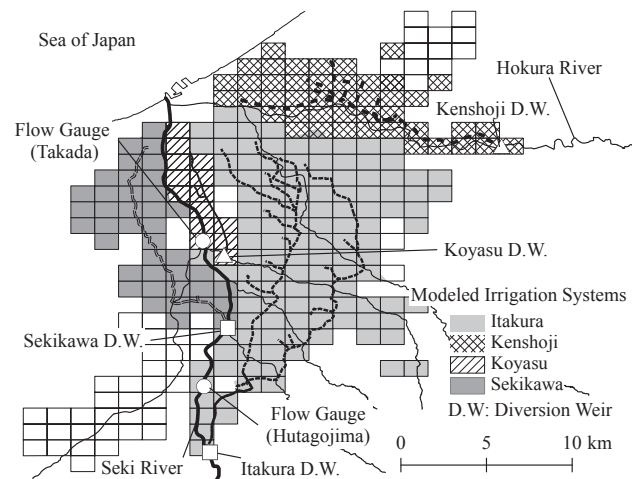

Fig. 9 The modeled irrigated areas and their associated irrigation facilities in the lower Seki River basin.

3.3.4 Settings for the water allocation and management module

To apply the water allocation and management module, 16 irrigated blocks were delineated in the watershed by the method described in Section 2. Three major irrigation blocks, for which water is diverted at the Itakura, Sekikawa, and Kenshoji diversion weirs, respectively, are shown in **Fig. 9**.

In the reservoir operation scheme, each reservoir needs to be linked to a diversion weir, so that the water released for irrigation can be estimated. Here, the Sasagamine dam reservoir is linked to the Itakura diversion weir, and Nojiri Lake is linked to the Sekikawa diversion weir. The maximum release from each reservoir for hydropower generation was set to 3.28m³/s based on the published operation rule (Niigata Prefecture, 1985).

The paddy outlet height was set to 30 mm, and the maximum infiltration rate at the paddy surface was set to 5 mm/d, based on survey data obtained by the Hokuriku Regional Agricultural Administration (1984). Planting starts when the allocated water is greater than 120 mm, which is the water requirement for irrigation planning in this region, and the cropping period was set to 100 days.

3.4 Results and discussion

3.4.1 Validation of model with rivere discharges

Model performance was first evaluated by comparing the calculated river discharges with the actual discharges observed at the two flow gauge stations along the Seki River (**Fig. 5**) during the period from 1976 to 2008. The hydrograph for 2006 is shown in **Fig. 10** and **Fig. 11**. The relative error between the calculated and the observed discharges was 27.0%, and the chi-square error was 7.2 m^3/s. Hydrographs for the years 2003-2007 are shown in the appendix to this section (**Fig. 18**-**Fig. 22**).

Next, the impact of agricultural water use on the flow regimes at the two flow gauges was evaluated. Calculated discharges for the irrigation period (May through September) were compared with observed discharges at Futagojima station (immediately below the diversion weir) (hydrographs for 2006 are shown in **Fig. 11**). The hydrograph calculated with diversion (solid line) corresponds well to the observed discharges (open circles), but the hydrograph calculated without diversion (dotted line), which represents the natural flow condition, does not. Thus, the difference between the discharges calculated with and without diversion represents the effect of water diversion on the river flow. Hydrographs for the years 2002 to 2007 are presented in the appendix of this section (**Fig. 23**-**Fig. 28**).

Finally, discharges at Takada station (near the basin outlet) during the irrigation period in 2006 were calculated with both diversion and return flow (**Fig. 12**, solid
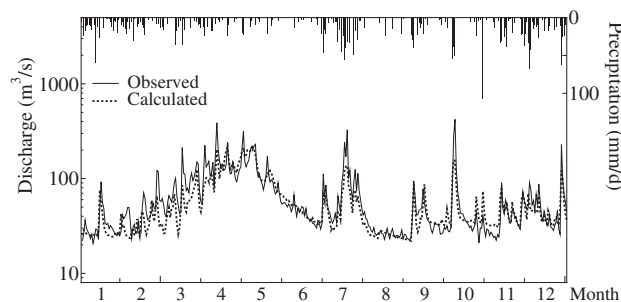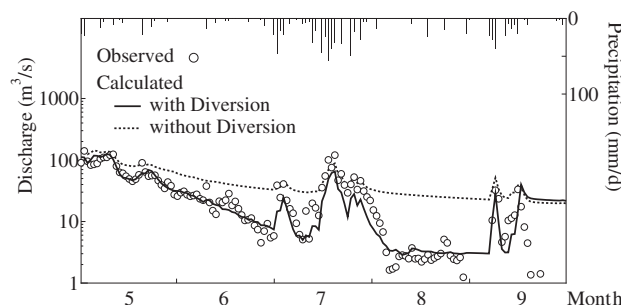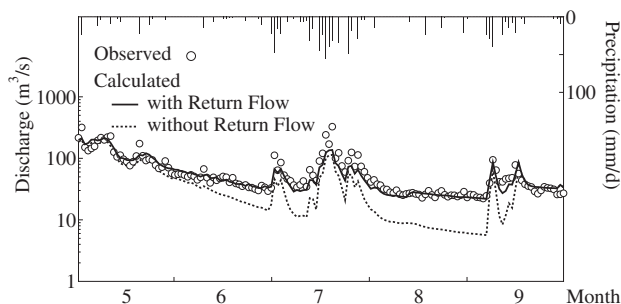
Fig. 12 Changes in calculated discharges at Takada from May through September 2006 due to the incorporation of return flow processes into the model.

line) and with diversion but without return flow (i.e., water is diverted at the weirs but does not drain from the paddy fields) (dotted line) and compared with the observed values (open circles). Here, the difference between the calculated value with return flow and that calculated without return flow reflects the drainage from the irrigated paddy areas. However, the drainage water from irrigated areas consists of both rainwater and diverted water, and their contributions to total drainage are difficult to separate. Thus, this model experiment does not by itself reveal the amount of diverted water in the return flow. All results for 2002 to 2007 are presented in the appendix to this section (**Fig. 29**-**Fig. 34**).

When water allocation was incorporated into the model, the calculated discharges during irrigation periods agreed closely with the observed data at both Futagojima and Takada flow gauge stations. These results show that river discharge at both observation points is strongly influenced by diversion and return flow processes, and that the developed water allocation and management module well represents the interaction between water circulation in irrigated paddy areas and the stream flow system.

3.4.2 Changes to the flow regime simulated by the reservoir operation scheme

The reservoir operation scheme was validated by using the time series of storage data for Sasagamine dam for 2002 and 2003 (**Fig. 13**). Although the time series data for reservoir inflows and effluxes are published, the data do not satisfy the reservoir water balance; thus, these data were not used to evaluate the reservoir operation scheme. Instead, the calculated storage volume was compared with the observed storage volume of the dam. The general pattern of annual changes in the calculated storage agreed with the pattern of annual changes in the observed storage: (1) storage increased sharply at the end of March; (2) plateaued until 1 June, the starting date of irrigation releases (predetermined by the operation rule); (3) decreased as the volume released for irrigation increased; and (4) gradually recovered during fall and winter. However, the absolute values of the ob-
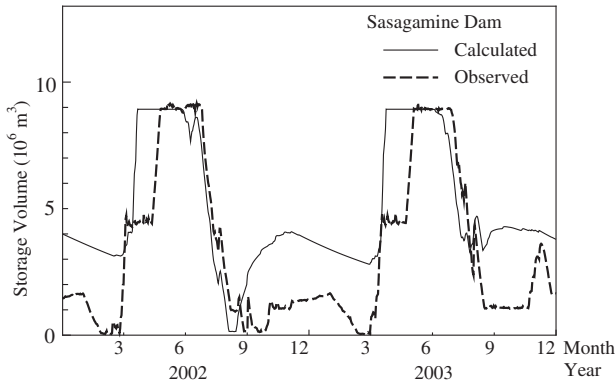

Fig. 10 Comparison between the calculated discharges and the observed discharges at Takada flow gauge station in 2006.

Fig. 11 Changes in calculated discharges at Futagojima from May through September 2006 due to incorporation of water allocation processes into the model.

Fig. 13 Comparison between the calculated and observed storage volumes in Sasagamine dam reservoir in 2002 and 2003.
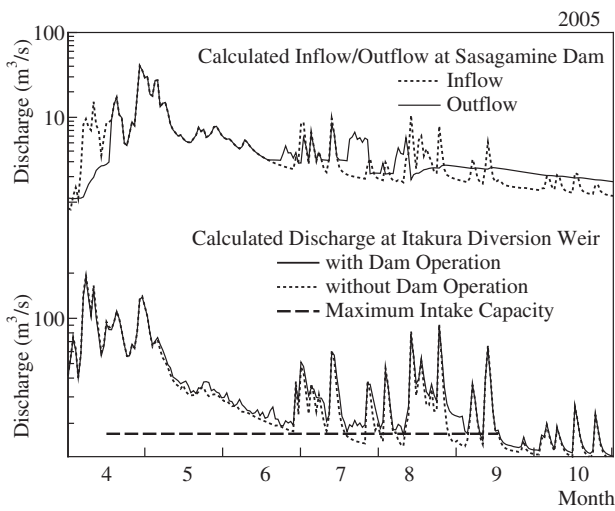

Fig. 14 Comparison of the calculated inflows and outflows at Sasagamine dam (top) and changes in the discharges at the Itakura diversion weir calculated with and without dam operation(bottom).

served and calculated storage values differed. These discrepancies are attributable to two assumptions of the module. First, as described in section 3.2.1, the release for hydropower generation was set to a constant. Second, the release for water use Q_{ru} was estimated simply by summing the releases for different uses, including irrigation Q_{ri} and hydropower generation Q_{rp} (see equation (39)). The discrepancies can be reduced by incorporating data specific to Sasagamine dam. For instance, Horikawa et al. (2012), who performed a detailed evaluation of the impact of climate change on reservoir operation, was able to improve the calculated storage by using a specific model for Sasagamine dam.

Although the reservoir operation scheme proposed here employed simple assumptions, water releases during the irrigation period were appropriately simulated. Comparison of the calculated inflows and outflows at Sasagamine dam (**Fig. 14**, top) with changes in the calculated discharge at the Itakura diversion weir with and without dam operation (bottom) showed that the calcu-

lated discharge without reservoir operation was less than the maximum intake capacity of the Itakura diversion weir in the middle of July and at the end of August, whereas the calculated discharge with reservoir operation remained higher than the maximum intake capacity. These results confirm that the reservoir operation scheme properly represents the supplementary release of water for irrigation.

3.4.3 Estimated water circulation within an irrigated areas

Fig. 15 shows the estimated water circulation within the Itakura Irrigation Area, which is the largest irrigation block in the watershed, from April through September, including the time series of precipitation and water diversion at the weir (top), the ponding depth in the paddies (middle), and the amount of water supplied to paddies and the water loss during allocation (bottom). Each value in **Fig. 15** is averaged over the entire irrigated block. Water diversion at the Itakura diversion weir was stable at a rate of approximately 22 mm/d (top), and the ponding depth in the paddies was maintained at the target water depth of 20 mm (middle), indicating that the irrigation supply to paddies was sufficient. The maximum rate of water allocation (bottom) of approximately 12 mm/d, reflecting the irrigation efficiency I_e (set to 0.6), illustrates the trade-off between water allocation and water loss during allocation. During rainfalls (e.g., at the end of June and the beginning of July), much of the allocated water drained from the irrigated area (increasing the water loss), but the water loss decreased during low-precipitation periods (e.g., in the middle of July).
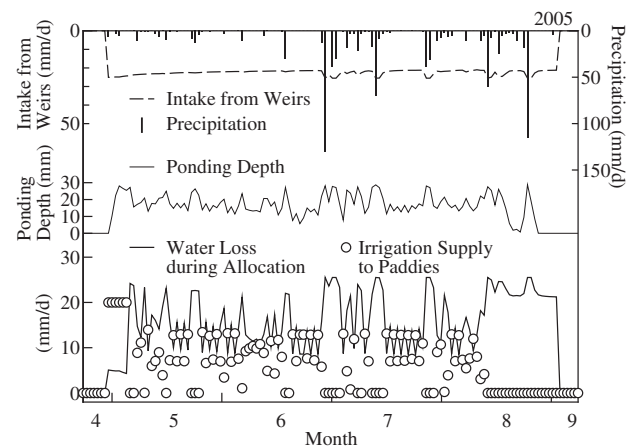
Fig. 15 Estimated water circulation in the Itakura Irrigation Area, which receives water diverted at the Itakura diversion weir.

3.4.4 Return ratio of diverted water from irrigated areas

Water movement within the irrigated areas is complicated not only by the substantial Volumes involved but

also by repeated cycles of diversion and return flow. Understanding the dynamics of return flow is crucial for characterizing flow regimes in watersheds where irrigated paddies predominate. However, direct measurement data are rarely available and measurement alone cannot capture the entire return flow from irrigated areas for the following reasons. First, drainage from irrigated areas is composed of both rainwater and water diverted for irrigation. Second, these two components are difficult to separate because the mixing processes vary temporally and the residence times in each flow pathway are not known. Therefore, instead of an observationbased approach, DWCM-AgWU was used to estimate the return ratio of diverted water at the catchment scale.

To calculate the return flow from irrigated areas, the inflow and return flow (drainage) points were first identified for each irrigated area as the points where the modeled streams cross the borders of the irrigated areas. Then, total inflow $Q_{inf}(t)$ and drainage $Q_{dng}(t)$ of the irrigated area at time t were calculated as follows;

$$Q_{dng}(t) = \sum_{i=1}^{N_d} Q_{ch}(i,t) \tag{49}$$

$$Q_{inf}(t) = \sum_{i=1}^{N_i} Q_{ch}(i,t), \tag{50}$$

where $Q_{ch}(i, t)$ is the calculated stream inflow at time t (m³/dt), and N_i and N_d are the numbers of inflow and drainage points, respectively.

For the largest irrigated area in the watershed, the Itakura Irrigation Area, 33 inflow and 21 drainage points were identified **Fig. 16**. This large number of points means that it is difficult to conduct the necessary observations to evaluate return flow at the catchment scale.

To eliminate the effect of influx from adjacent upstream areas, net drainage from irrigated areas $Q_{net}(t)$ (m³/dt) was calculated by subtracting total inflow $Q_{inf}(t)$ from total drainage $Q_{dng}(t)$.

$$Q_{net}(t) = Q_{dng}(t) - Q_{inf}(t) \tag{51}$$

Because Q_{net} can be composed of both rainwater and diverted water for irrigation, and these two components are difficult to separate, to evaluate the contribution to Q_{net} of water diverted for irrigation, the averaging time period for the calculation was set to a period during which Q_{net} consisted of both rainwater and diverted water. Then, the return flow of diverted water was evaluated over this averaging period. Here, the proportion of diverted water in Q_{net} was assumed to reflect the ratio of diverted water to the total water input during the averaging period, which is called the rainfall-irrigation ratio R_{ri}.

$$H_i(t) = Q_i(t)/A_{irg} \times 1000 \tag{52}$$
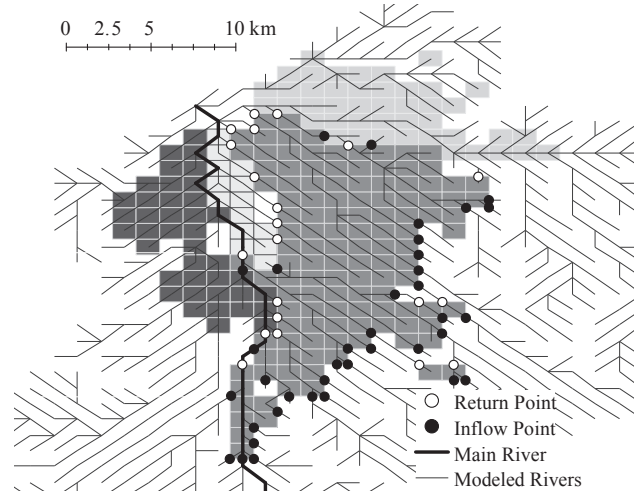
Fig. 16 Locations of inflow and return flow points in the Itakura Irrigation area.

$$R_{RI} = \sum_{t_i}^{t_e} \left(\frac{H_i(t)}{H_i(t) + P_{area}(t)} \right) \tag{53}$$

Equation (52) converts $Q_i(t)$, the volume of water diverted for irrigation at time t (m³/dt)), to water depth $H_i(t)$ (mm/dt), where A_{irg} is irrigated area (m²). Then, R_{RI} is calculated with equation (53), where $P_{area}(t)$ is precipitation over the irrigated area (mm/dt), and ti and te are the initial and terminal times of the averaging period, respectively. In this study, the entire irrigation period (25 April to 10 September) was used as the averaging period.

Finally, the return ratio F_r is calculated as the product of the rainfall-irrigation ratio and the ratio of net drainage to total diverted water, summed over the averaging period:

$$F_r = \sum_{t_i}^{t_e} \left(\frac{Q_{net}(t)}{Q_i(t)} \right) R_{RI} \tag{54}$$

The return ratio during the irrigation period was calculated for each irrigated area over a 33-year period (1976-2008). In the Itakura Irrigation Area, the average return ratio was 69.6%, and the ratio varied annually from 63.2% to 76.9% (**Fig. 17**, **Table 1**). Thus, a large proportion of the diverted water was returned to the river, where it presumably contributed to the stability of the downstream water supply.

The largest return ratio (76.9%) was obtained for the wettest year (1985) among the 33 years, and the smallest value (63.2%) was obtained for the driest year (1994). In 1994, 246 mm of rain fell during the irrigation period. Under such dry conditions, farmers try to retain water in the paddies, which decreases the management water loss. A large portion of the retained water, however, is lost through ET because of the dry conditions. Thus, the calculated decrease in the return ratio under extremely dry conditions is reasonable.
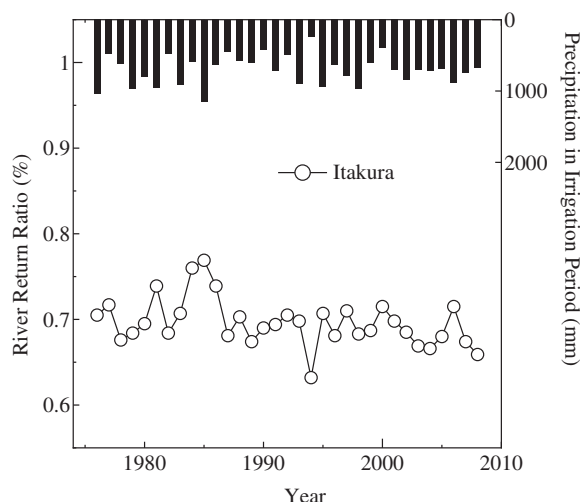
Fig. 17 Annual variation in the return ratio in the Itakura Irrigation Area from 1975 to 2009 compared with precipitation during the irrigation period of each year.

Table 1 Estimated precipitation (mm), actual ET (mm), and river return ratios in the Itakura Irrigation Area (1976-2008).

Year	Precipitation	Actual ET	River Return Ratio
1976	1038	511	0.705
1977	484	495	0.717
1978	618	533	0.676
1979	964	522	0.684
1980	796	517	0.695
1981	956	503	0.739
1982	483	503	0.684
1983	913	498	0.707
1984	586	484	0.760
1985	1148	467	0.769
1986	638	475	0.739
1987	446	498	0.681
1988	583	485	0.703
1989	608	524	0.674
1990	424	505	0.690
1991	719	500	0.694
1992	497	488	0.705
1993	899	484	0.698
1994	246	534	0.632
1995	937	509	0.707
1996	634	525	0.681
1997	785	505	0.710
1998	966	515	0.683
1999	598	514	0.687
2000	394	482	0.715
2001	704	506	0.698
2002	839	519	0.685
2003	698	525	0.669
2004	716	555	0.666
2005	691	540	0.680
2006	890	508	0.715
2007	744	529	0.674
2008	673	563	0.659
Average	706	510	0.696

Although the largest return ratio was obtained for the wettest year, a correlation between rainfall amount and the return ratio is less evident in wet years. For example, in 1998, the return ratio was relatively low (68.3%) (below the average) despite the higher than average

rainfall (966 mm). This result may be attributable to the duration of the averaging period (i.e., the entire irrigation period from 25 April to 10 September). During this rather long averaging period, a single intensive rainfall (e.g., 200 mm or more) could decrease the rainfall irrigation ratio RRI for the entire period, and consequently reduce the calculated return ratio. Further research is required to determine an appropriate duration for the averaging period.

3.5 Summary

In this section, a novel approach to simulating the interaction between natural and anthropogenic water cycles in watersheds dominated by irrigated paddies was presented. The novel concepts used should contribute to ongoing discussions about how to incorporate anthropogenic impacts into distributed hydrological models. The approach and the results obtained by its application are summarized as follows:

1) A recently configured GIS database of water use facilities throughout Japan was used to extract specifications for each facility, as well as for irrigation channel networks and irrigation block polygons. In addition, an algorithm was developed to connect vector and polygon data so that water allocation to irrigated areas could be simulated.

2) A water allocation and management module, which is independent of the surface runoff calculation, was incorporated into the base model so that the supplementary release of water for irrigation, water diversion at weirs, and water allocation and return flow within irrigated areas could be simulated.

3) When water allocation was incorporated into the model and applied to the Seki River basin as a case study, the calculated discharges during the irrigation period agreed closely with the observed data at two flow gauge stations, showing that stream flow was strongly influenced by both diversion and return flow processes. The water allocation and management module was thus shown to be highly capable of representing the interaction between water circulation in irrigated paddy areas and stream flow systems.

4) The largest and smallest return ratios were obtained for the driest and wettest years, respectively. These results are reasonable from the viewpoint of the water balance in the irrigated areas, though the correlation between rainfall amount and return flow was not as clear in wet years as it was in dry years. The lack of correlation in wet years may mean that the duration of the averaging period used was too long. Further research is required to determine the appropriate averaging period duration.

Appendix 3
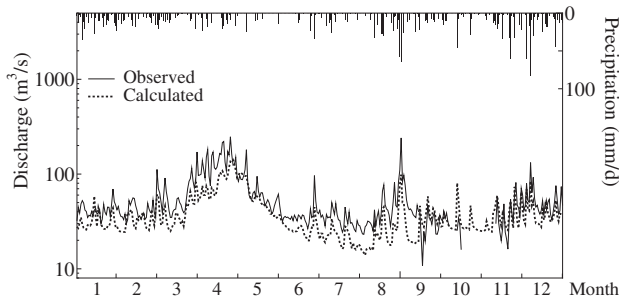Appendix 3A: Hydrographs at Takada

Fig. 18 Comparison between the calculated discharges and observed discharges at Takada flow gauge station in 2003.
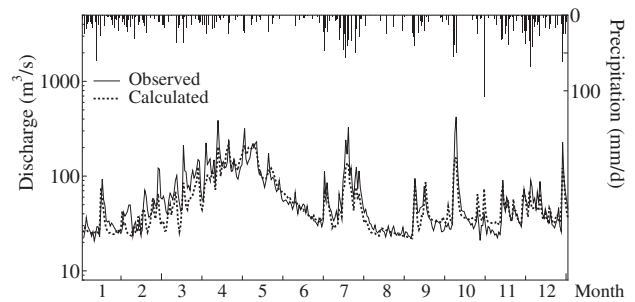

Fig. 21 Comparison between the calculated discharges and observed discharges at Takada flow gauge station in 2006.
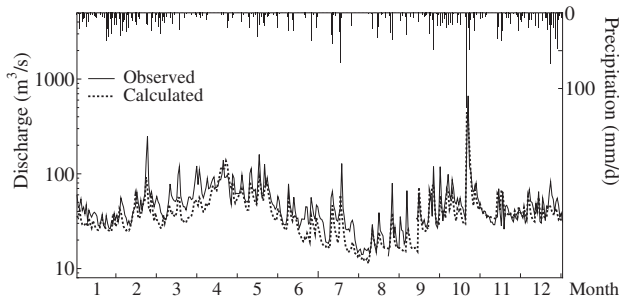

Fig. 19 Comparison between the calculated discharges and observed discharges at Takada flow gauge station in 2004.
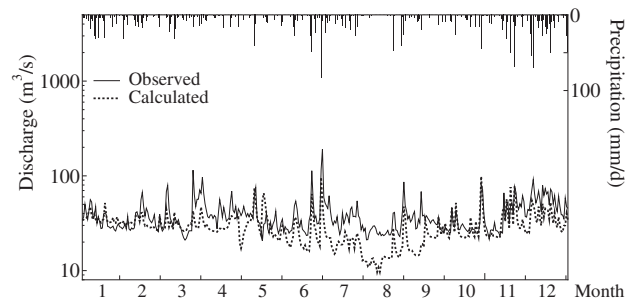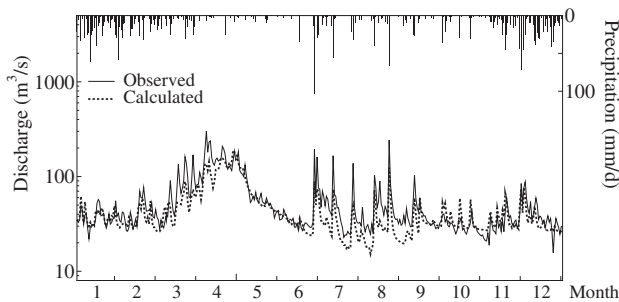

Fig. 22 Comparison between the calculated discharges and observed discharges at Takada flow gauge station in 2007.

Fig. 20 Comparison between the calculated discharges and observed discharges at Takada flow gauge station in 2005.

Appendix 3B: Changes in calculated discharges at Futagojima due to incorporation of water allocation and management module
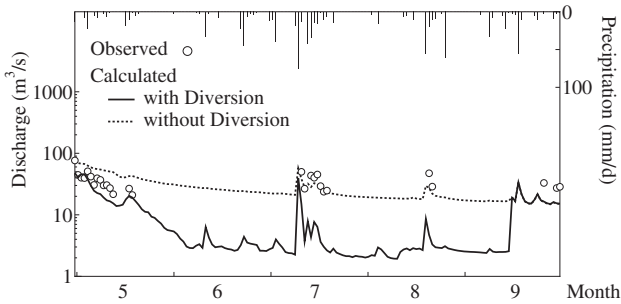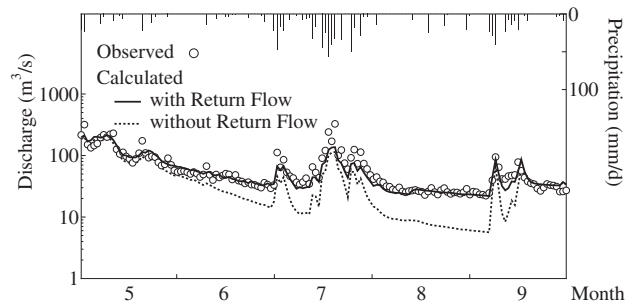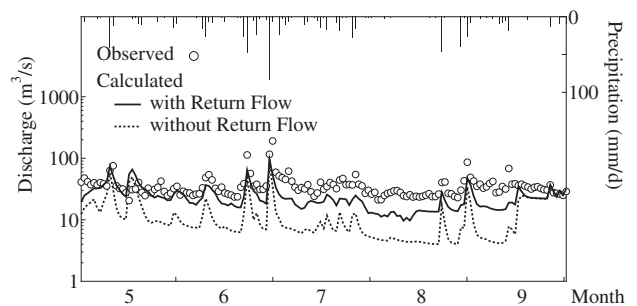

Fig. 23 Changes in calculated discharges at Futagojima from May through September, 2002 due to incorporation of water allocation processes into the model.
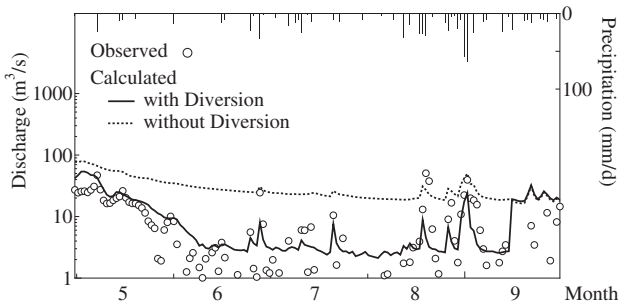
Fig. 24 Changes in calculated discharges at Futagojima from May through September, 2003 due to incorporation of water allocation processes into the model.
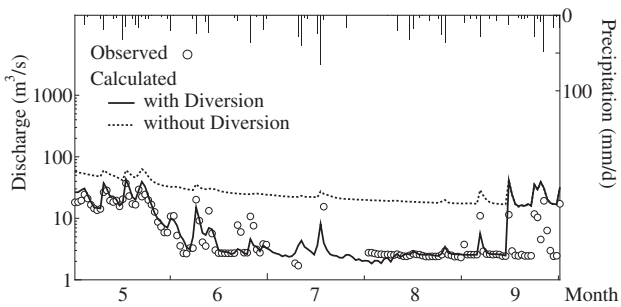
Fig. 25 Changes in calculated discharges at Futagojima from May through September, 2004 due to incorporation of water allocation processes into the model.
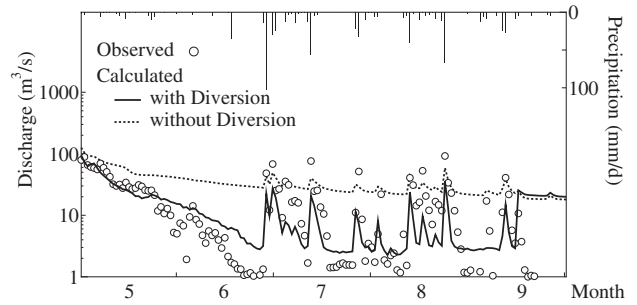
Fig. 26 Changes in calculated discharges at Futagojima from May through September, 2005 due to incorporation of water allocation processes into the model.
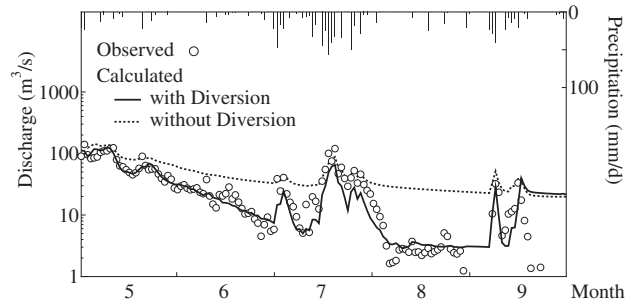
Fig. 27 Changes in calculated discharges at Futagojima from May through September, 2006 due to incorporation of water allocation processes into the model.
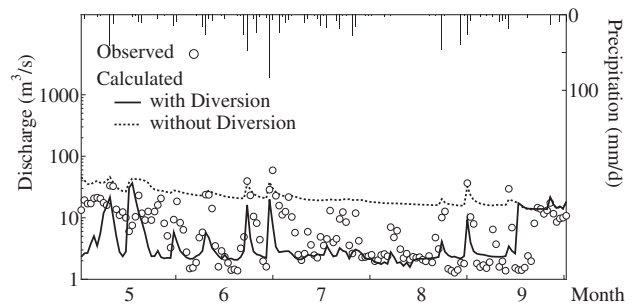
Fig. 28 Changes in calculated discharges at Futagojima from May through September, 2007 due to incorporation of water allocation processes into the model.

Appendix 3C: Changes in calculated discharges at Takada due to incorporation of return flow processes into the model
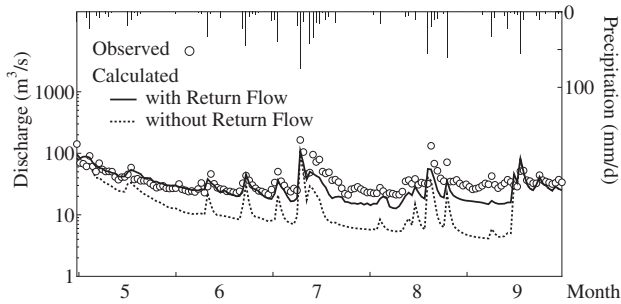
Fig. 29 Changes in calculated discharges at Takada from May through September, 2002 due to incorporation of return flow processes into the model.
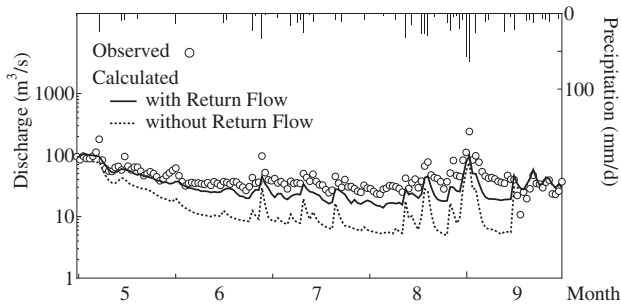
Fig. 30 Changes in calculated discharges at Takada from May through September, 2003 due to incorporation of return flow processes into the model.
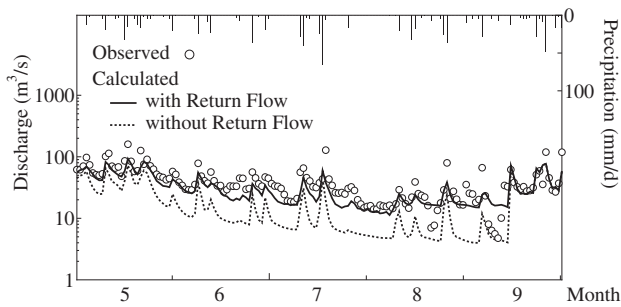
Fig. 31 Changes in calculated discharges at Takada from May through September, 2004 due to incorporation of return flow processes into the model.
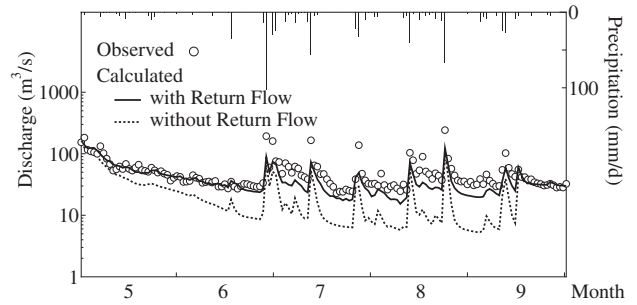
Fig. 32 Changes in calculated discharges at Takada from May through September, 2005 due to incorporation of return flow processes into the model.

Fig. 33 Changes in calculated discharges at Takada from May through September, 2006 due to incorporation of return flow processes into the model

Fig. 34 Changes in calculated discharges at Takada from May through September, 2007 due to incorporation of return flow processes into the model.

4. A snowfall and snowmelt module for warm climate watersheds and its integration into DWCM-AgWU

4.1 Introduction

The timing and pattern of snowmelt play a critical role in runoff generation in Japanese watersheds. Section 4 presents a grid-based snowfall and snowmelt module in which daily snow accumulation and snowmelt are calculated based on a simplified energy balance. Remotely sensed snow-covered areas are used to estimate the spatial distribution of a model parameter in regions where observed meteorological data are sparse.

4.2 Development of the snowfall and snowmelt module

4.2.1 Estimation of snowmelt based on the energy balance

The amount of energy used for snowmelt Q_m (W/m^2) is estimated by using the energy balance of snow surface as follows

$$Q_m = R_n + H + \iota E + Q_g + Q_r \tag{55}$$

$$R_n = (1 - \alpha)S^{\downarrow} + L^{\downarrow} - \epsilon\sigma(T_s + 273.15)^4, \tag{56}$$

where R_n is net radiation, H and ιE are the sensible and latent heat fluxes (positive for influxes into the snow layer, W/m^2), $S^{\downarrow}$ is the downward short wave radiation (W/m^2), $L^{\downarrow}$ is the downward long wave radiation (W/m^2), α is albedo of snow surface, ε is emmision rate of snow surface (=0.97), σ is the Stephan-Boltzman constant (= 5.67×10^{-8}(W/(m^2 K^4))), T_s is the temperature of snow surface (℃), Q_g is the heat flux from ground (W/m^2), and Q_r is the heat flux from rain (W/m^2).

The developed module is intended to represent snowfall and snowmelt in areas where precipitation in winter falls mainly as snow in a relatively warm climate. So that equation (55) could be applied to such an area, the energy balance employed for the calculation was simplified by adopting the following two assumptions (Suizu, 2001). First, the outgoing sensible H and latent heat ιE fluxes emitted from the snow surface were neglected (e. g., the sensible heat flux associated with extremely low temperatures or sublimation from the snow surface). Second, the freezing of meltwater in the snow layer was not simulated in the module. In other words, H is calculated by the module whenever the daily average air temperature T_a is more than 0℃, and the only latent heat flux considered is the influx into the snow layer that occurs with condensation at $T_a > 7$℃ and precipitation $p > 0$.

However, these assumptions cause snowmelt to be simulated whenever the calculated energy balance is positive (i.e. $R_n + Q_r > 0$) even if the actual energy balance Q is negative ($Q = R_n + H + \iota E + Q_r$). To avoid the simulation of snowmelt when Q is actually negative, the module calculates daily snowmelt M (mm/d) only when

$Q > 0$ and the daily average temperature is greater than -3℃ (Suizu, 2001).

$$M = \begin{cases} \dfrac{Q}{\iota_f \rho_w} \times 86400 & (T_a \geq 0) \\ \dfrac{Q}{\iota_f \rho_w} \dfrac{T_a + 3}{3} \times 86400 & (0 > T_a > -3), \end{cases} \tag{57}$$

where ι_f is the specific heat of ice melt (= 0.33×10^6 (J/kg)), ρ_w is the density of water (1.0×10^3(kg/m^3)), and T_a is the daily averaged temperature (℃).

Besides the snowmelt M calculated with equation (57), the constant rate of snowmelt due to the ground heat flux M_g (mm/d) is also calculated. The value of M_g was set to 1.0 mm/d because observed values of M_g in Japan range from 0.6 to 1.2 mm/d (Ono et al., 1986).

(1) Estimation of shortwave radiation incorporating solar illumination geometry

Downward shortwave radiation $S^{\downarrow}$ was estimated from the daily average global radiation S_d. The shortwave radiation received by a grid cell varies according to the angle and direction of its slope, especially during winter. Thus, solar illumination geometry was incorporated into the estimation of the actual shortwave radiation for each grid cell.

The daily average global radiation S_d (W/m^2) was estimated from the sunshine ratio (=sunshine duration/potential sunshine duration) and extraterrestrial radiation S_{0d} (W/m^2) (Kondo et al., 1991).

$$S_d = \begin{cases} \left(a\dfrac{N}{N_0} + b\right) S_{0d} & (N > 0) \\ c\, S_{0d} & (N = 0), \end{cases} \tag{58}$$

where N is the sunshine duration (h), N_0 is the possible sunshine duration (h), a, b, c is pyranometer coefficients; the typical values of the coefficients used for AMeDAS observations are a=0.244, b=0.511, and c=0.118 (Kondo et al., 1991) The extraterrestrial radiation S_{0d} is calculated with equation (59), and potential sunshine duration N_0 is calculated with equation (61).

$$S_{0d} = \frac{I_{00}}{\pi}\left(\frac{d_0}{d}\right)^2 (H \sin\phi\sin\delta + \cos\phi\cos\delta\sin H) \tag{59}$$

$$H = \cos^{-1}(-\tan\phi\tan\delta), \tag{60}$$

where I_{00} is the solar constant (=1365 (W/m^2)), H is the solar time angle from sunrise to its culmination (rad), ϕ is latitude (rad), δ is solar declination (rad), and d and d_0 are the distance between the sun and earth and the average distance between them, respectively.

$$N_0 = \frac{2H_0}{0.2618}, \tag{61}$$

where H_0 is solar time angle from sunrise to its culmination.

Next, the downward short wave radiation of each grid cell $S^{\downarrow}$ is estimated from S_d and a reception index f, which accounts for solar illumination geometry of grid
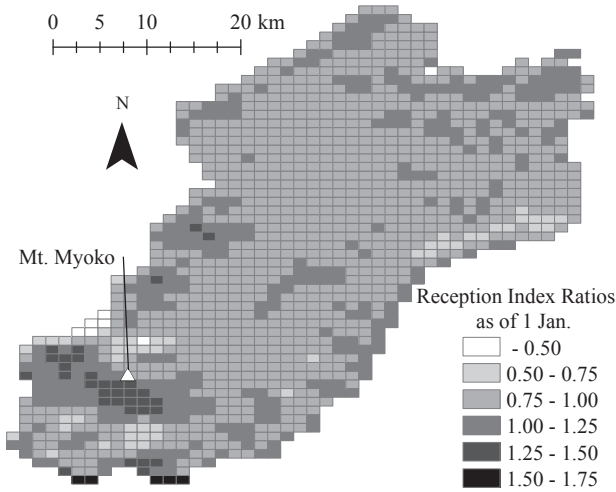
Fig. 35 Spatial distribution of reception index ratios on 1 January.

cells. The reception index f is given by equation (62) as the inner product of the vector normal to the grid cell and the direction of the sun at its culmination (Lu et al., 1998).

$$f = \cos \delta \cos \phi + \sin \phi \sin \delta + \tag{62}$$
$$\tan \theta (\cos \delta \cos \beta \sin \phi - \cos \delta \cos \beta \cos \phi),$$

where θ is slope angle ($0 < \theta < \pi/2$), β is slope direction ($-\pi < \beta < \pi$, 0 for south facing slope, and positive in the counterclockwise direction). The reception index for horizontal surface f_0 is given by $\theta = 0$ as follows:

$$f_0 = \cos \delta \cos \phi + \sin \phi \sin \delta \tag{63}$$

Finally, the shortwave radiation received by a grid cell, $S^{\downarrow}$, is estimated with equation (64).

$$S^{\downarrow} = \frac{f}{f_0} S_d \tag{64}$$

The spatial distribution of the reception index ratios (f / f_0) as of 1st of January of any given year is depicted in **Fig. 35**. Values of f / f_0 are close to 1 over flat plains; they increase to more than 1.25 on south-facing slopes, and decreased to less than 0.75 on north-facing slopes around the Mt. Myoko,

The snow surface albedo was parameterized on the basis of snow age and temperature (Yamazaki et al., 1994).

$$\alpha_n = \alpha_{min} + (\alpha_{n-1} - \alpha_{min}) \exp(-1/k) \tag{65}$$

$$\alpha_0 = \begin{cases} -0.12 T_a + 0.76 & (T_a \geq -1.0) \\ 0.88 & (T_a \leq -1.0) \end{cases} \tag{66}$$

$$k = \begin{cases} -4.9 T_a + 4.5 & (T_a \leq 0.1) \\ 4.0 & (T_a \geq 0.1), \end{cases} \tag{67}$$

where α_0 is an albedo of new snow surface, and α_{min} is the minimum of snow surface albedo ($=0.4$).

(2) Estimation of net long wave radaiation from sunshine duration

Net longwave radaiation, $L^{\downarrow} - \varepsilon \sigma (T_s + 273.15)^4$ (W/m²), is estimated by using the empirical relationship between the net longwave radiation and daily sunshine duration (Suizu, 2001). The long term observed data used for this study included the meteorological characteristics for different snowy areas of Japan, including Moshiri, eastern Hokkaido (cold and dry weather), Sapporo, western Hokkaido (cold and wet weather), and Nagaoka, Niigata (warm and wet weather).

$$L^{\downarrow} - \epsilon\sigma(T_s + 273.15)^4 = -53.01 \frac{N}{N_0} - 11.08 \tag{68}$$

(3) Estimation of sensible and latent heat flux

The sensible and latent heat flux H and ιE are estimated by the bulk equations (69) and (70).

$$H = c_p \rho C_h U (T_a - T_s) \tag{69}$$

$$\iota E = \iota \rho C_e U (q - q_s), \tag{70}$$

where $c_p \rho$ is the specific heat at constant pressure for air ($= 1.21 \times 10^3 \text{J/(Km}^3))$, C_h and C_e are the bulk coefficient for sensible and latent heat flux, respectively, q and q_s are the specific humidity of air and snow surface, respectively, and U is the daily averaged wind speed (m /s). Here, E (mm) denotes the amount of condensed water onto the snow surface.

To calculate H and ιE, spatial distribution of the wind speed U and diurnal variation must be properly accounted for. However, detailed wind speed data are not available, especially in remote mountainous areas. Therefore, the parameter k_{sl} (mm/(K d)) proposed by Suizu (2001), is employed, in which the spatial and diurnal variation of U are implicitly accounted for (equation (71)).

$$k_{sl} = \frac{c_p \rho C_h U}{\iota_f \rho_w} \times 86400 \tag{71}$$

For the calculation of k_{sl}, the following assumptions were made. First, the bulk transfer coefficients for sensible and latent heat on snow surface were set equal each other ($C_h = C_e$), because their estimated valuses are approximately 1.5-3.0 $\times 10^{-3}$ (Kondo, 1994). Second, the specific humidity q was converted to $q \doteqdot 0.622e/p_{atm}$, where e is vapor pressure at the snow surface (hPa) and p_{atm} is the standard atmospheric pressure. Third, because the presumed latent heat flux occured under very humid conditions (i.e. $T_a > 7$ ℃ and precipitation $p > 0$), the vapor pressure e was equated to the saturated vapor pressure at T_a, and vapor pressure at snow surface e_0 is equaled to the vapor pressure at $T_a = 0$ (i.e. $e_0 = 6.11$ (hPa)).

4.2.2 Estimation of the spatial extent of parameter k_{sl}

Because of the absence of detailed time series data

for wind speed U and the bulk coefficients C_h and C_e, k_{sl} was originally estimated by assuming that the calculated snow melting date was the same as the observed snow melting date (Suizu, 2001). For larger scale application of the model (e.g. watershed scale), the k_{sl} values at ungauged points can be estimated by a regression analysis in which the distance from the coast line, altitude and direction of slope are used as predictors (Suizu, 2002). However, clear relationship between the predictors and k_{sl} values are not always found, especially in the case of watersheds where snow observations are sparse.

Therefore, in this study, to allow more general application of the snowfall and snowmelt module, remotely sensed snow cover data are used to estimate the spatial distribution of k_{sl}. First, snow cover areas are extracted from remotely sensed images and overlaid on the model grid to estimate the snow melting date for each grid cell. The snow melting date (hereafter, the observed melting date) was assumed to be the same date that the images were taken. Next, the k_{sl} value of the grid cell was estimated such that the difference between the calculated and observed melting dates was minimized by using a global parameter search algorithm, called the SCE-UA method (Duan et al., 1992). The definition of the calculated melting date is that of the Japanese Society of Snow and Ice (1990), namely, the date after which no snow cover is observed at least for 30 days. To estimate k_{sl}, 10 repetitions of the search algorithm were carried out for each grid cell by changing the random seeds of the search algorithm for each repetition; then the average of the results was adopted as the estimated k_{sl} value of that grid cell. Finally, k_{sl} values of the grid cells for which no melting date could be estimated were determined by the inverse distance weighting method using the estimated k_{sl} values of the three neighbouring grid cells.

4.3 Study watershed
4.3.1 Winter precipitation in the study watershed
In the Seki River Basin in central Japan was selected for a case study (see section 3.3), over half of the average annual precipitation of more than 3000 mm falls as snow in winter. Among 339 stations in Japan where snow depth is continuously observed, record snowfalls were observed in winter 2005-2006 at 23 (Takahashi, 2007), whereas in winter 2006-2007, snowfall was remarkably lower than average at many of the stations. In the Seki River Basin, the snow depth in winter 2005-2006 was about three times that recorded in 2006-2007 (Yokoyama et al., 2007). By comparison, in the Tohoku Region, snow depth in 2005-2006 was about twice that in 2006-2007 (Motoya, 2008).

4.3.2 Collected winter precipitation data
(1) Estimation of the spatial distribution of snowfall
The grid system used for the snowfall and snowmelt module is the same as that described in section 3.3.3. Required meteorological data (precipitation, temperature, humidity, and wind speed) were collected from 1976 through 2008 at existing observation stations (**Fig. 36**). The details of the collected data and their processing for the model application are also described in section 3.3.3.

The estimated precipitation was classified into snowfall or rainfall depending on the daily average temperature T_a. The threshold value of T_a was determined based on 10 years of precipitation observations recorded at the Takada Weather Station (Sugaya, 1990). In these observations, the ratio of snowfall to total precipitation was 50% when T_a = 2.2 ℃, and it increased linearly from 0% to 100% as T_a increased from 0.5 to 4.0 ℃ The underestimation of snowfall caused by wind was corrected for by calculating the catch ratio C_r:

$$C_r = \frac{1}{1 + mU}, \tag{72}$$

where m is a specific parameter that depends on the type of raingauge (Yokoyama et al., 2003). The value of m was set to 0.346 for for the typical AMeDAS raingauge (RT-3).

(2) Observed snow water equivalent data
For model validation, snow water equivalent (SWE) data were collected at 31 points in the study watershed (**Fig. 36**), where continuous monthly observations have been carried out for almost 20 years by researchers at the NARO Hokuriku Agricultural Research Center. The snow surveys are conducted monthly, in January, February, and March of each year. Each survey point is located in an open, flat to gently sloping area to minimize the effect of wind on the measurement. At each sampling time, three samples are collected at each point and the average is used as the observed SWE (**Fig. 37**). Among the 20 years of observed data, data from three years were selected for the model validation: namely, a heavy snow year (2005-2006), a light snow year (2006-2007), and an average snow year (2002-2003).

The snow surveys are carried out in four areas of the study watershed (**Fig. 36**). The distribution of SWE in relation to elevation in each of these areas in February 2006 is shown in **Fig. 38**. In February 2006, snowmelt was relatively small compared to the total snowfall, so the SWE distribution mainly reflects the original spatial distribution of the snowfall. The increase rate of SWE with elevation varied among the four areas: it was 0.159 in the Ikenodaira Area, 0.527 in the Iiyama Area, 1.585 in the Myoko Area, and 2.265 in the Kubiki Area. The increase rates in the four areas averaged over the nine observations were 0.326, 0.635, 0.902, and 1.618 mm/
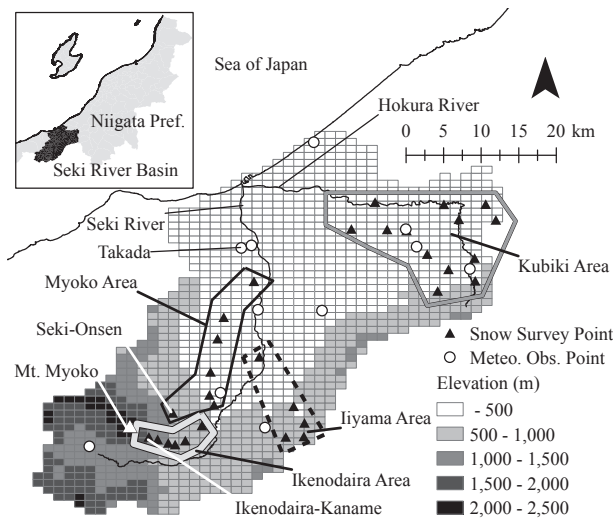
Fig. 36 Map of the Seki River Basin showing the snow survey observation points and areas.

Fig. 37 A snow sampler being used during the snow survey.

m, respectively.

(3) Remotely sensed snow-covered areas

Remotely sensed imagery from the MODIS (MODerate resolution Imaging Spectroradiometer) satellite was used to detect snow-covered areas. The spatial resolution was 500 m for the wavelength ranges used in the analysis (1.230 - 1.250μm and 1.628 - 1.652μm, Japanese Agricultural System Society, 2007). Thirteen images were selected from the MODIS data archive. The selected images were acquired on 7 March, 24 March, 7 April, 28 April, 4May, and 21 May in 2006; and on 21 March, 23 March, 12 April, 29 April, 14 May, 21 May, and 29 May in 2007. The snow-covered areas of the study watershed were detected by supervised classification using the spectral signatures for snow cover (e.g., at the top of high mountains) as the supervisor.
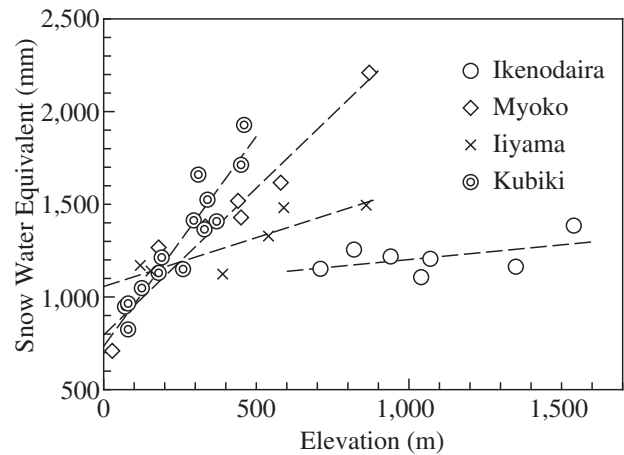
Fig. 38 Relationship between SWE and elevation in the four areas of the study watershed (February 2006).

4.4 Results and discussion
4.4.1 Estimated spatial disribution parameter k_{sl}

The average values of k_{sl} obtained by the 10 repetitions of the parameter search are shown in **Fig. 39**. For most grid cells, the difference between the maximum and minimum estimate was 0.1-0.2, but for some it was as large as 5. Among the variables used to estimate k_{sl} (sensible and latent heat fluxes, net radiation, and the ground heat flux; see equation (71)), net radiation and ground heat flux were determined from the observed meteorological data. As a result, k_{sl} is the only parameter that determines the snow melting date. If the estimated value of k_{sl} is larger than the best (optimized) value, the difference between the observed snow melting date and the date calculated with an objective function will increase, and vice versa. Therefore, the shape of the objective function is theoretically similar to that of a quadratic function with one depression, at which the optimal k_{sl} can be obtained.

However, the actual shape of the function is composed of discrete values because the objective function is calculated as a difference betweent the obesrved and calculated melting dates. Thus, if the depression of the function is flat, the range of the estimated k_{sl} will be wider. A wide range of the estimated k_{sl} implies a low contribution of the sensitive and latent heat fluxes to the total energy used to melt the snow. Possible causes are overestimation of the net radiation and ground heat flux, underestimation of snowfall, and heat sources neglected by the model (e.g., heat emitted from urban areas).

Grid cells in which the estimation range of k_{sl} exceeded 1 (open circles in **Fig. 39**) were excluded from the analysis. As a result, 42 of the 313 grid cells (13.4%) were excluded. The values of the non-excluded grid cells (black circles in **Fig. 39**) were then used to estimate k_{sl} by the inverse distance weighting method. **Fig. 40** shows the spatial distribution of the estimated k_{sl} values. In the low-lying area near the coast, k_{sl} values
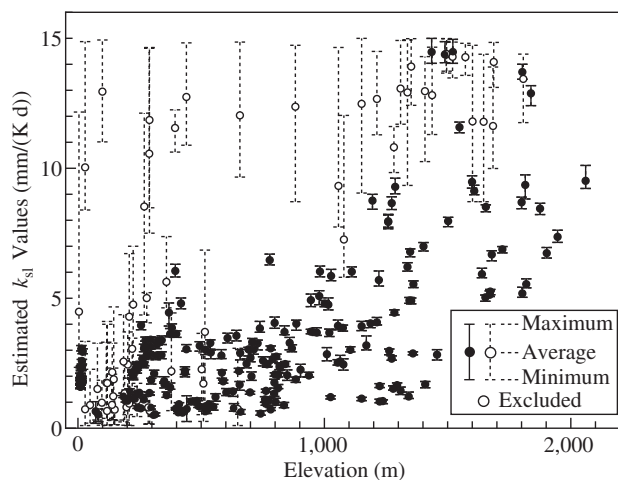
Fig. 39 R elationship between estimated k_{sl} values and elevation. Bars indicate maxima and minima estimated from satellite images of snow-covered areas. Data shown with white circles were excluded from further analysis.
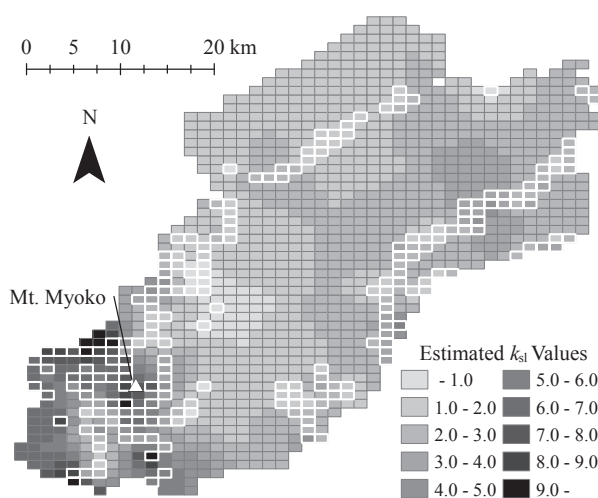

Fig. 40 Spatial distribution of ksl as estimated from satellite images of snow-covered areas. Snowmelt dates were obtained from satellite images for the grid cells outlined in white.

were approximately 1.5, similar to the value estimated at Takada (k_{sl} = 1.7; Suizu, 2001). Then k_{sl} values gradually increased with elevation, and they exceeded 10 on the south-facing slope of Mount Myoko, where sensible heat transfer contributed greatly to snowmelt because of strong winds and high daytime temperatures.

4.4.2 Comparison of observed and calculated SWE

Calculated SWE values in each of four areas were plotted against observed values **Fig. 36**. In each graph (**Figs.41**, **42**, **44**, and **46**), dashed lines are plotted ±200 mm away from the line of one-to-one correspondence between calculated and observed SWE. An SWE difference of 200 mm is equivalent to a difference of 5-7 days in the snow melting date if the maximum snowmelting rate is assumed to be 30-50 mm/d. This discrepancy in melting date is considered acceptable because of the heterogeneity of snow accumulation and snowmelt processes in the grid cells, and given the spatial resolution of the MODIS data (500 m). In the description below, the dashed lines are referred to as 200 mm lines.

(1) **Kubiki Area**

Among the four areas, SWE estimates were most accurate in the Kubiki area, where all but two data points plotted within the 200 mm lines (**Fig. 41**). This result is attributed to the relatively gentle slopes and high density of rain gauges within this area. Time series of SWE at all observed points in the Kubiki area are shown in the Appendix 4A of this section (**Figs.50-62**).

(2) **Ikenodaira Area**

Calculated and observed SWEs in the Ikenodaira area, the highest area in the study watershed, are compared in **Fig. 42**. The data points are more scattered compared with those in the Kubiki area, but 76% of all points

plotted within the 200 mm lines. The time series of observed and calculated SWE and cumulative snowmelt at the Ikenodaira-Kaname point (1540 m.a.s.l) (**Fig. 43**) shows that the cumulative snowmelt was only about 100 mm in the middle of March, which is quite small compared with the SWE (between 1000 and 2000 mm at maximum). Hence, the discrepancy between calculated and observed SWE can be attributed mainly to errors in snowfall estimation due to the few rain gauge observations and strong winds in high-altitude areas. Time series of SWE at all observed points in this area are shown in the Appendix 4B (**Figs.63-67**).

(3) **Myoko Area**

In a similar way in the Ikenodaira Area, all the observed and calculated SWE were presented (**Figs. 44** and **45**). In the Myoko area, the calculated SWE values were underestimated compared with the observed values; only 64% of the total points plotted within the 200 mm lines (**Figs. 44**). In this area, the increase rate with elevation of winter precipitation given by Mesh Climatic Data 2000 is 0.310 (mm/m), which is less than the observed increase rate of 0.902 mm/m (see section 4.3.2). Thus, the underestimation of SWE in this area is partly attributable to the underestimated winter precipitation.

Another possible cause of the discrepancy is locally heavy snowfall. The time series of observed and calculated SWE and cumulative snowmelt at the Seki-Onsen point (870 m.a.s.l) (**Fig. 45**) shows that the calculated SWE corresponds well to the observed SWE in 2003 and 2007 but not in 2006, when it was underestimated. Moreover, the discrepancy was large even in January and February, when the cumulative snowmelt was very small. Hence, the underestimation of the snowfall may account at least in part for the underestimation of SWE.
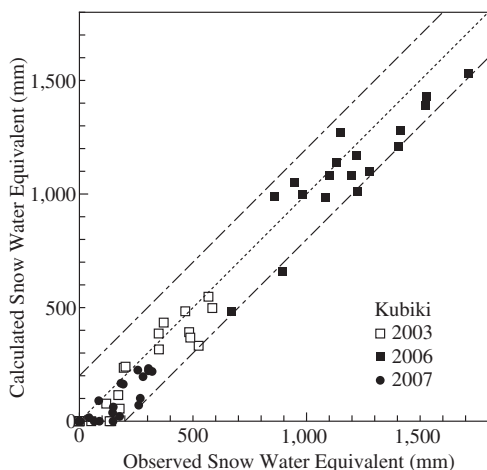
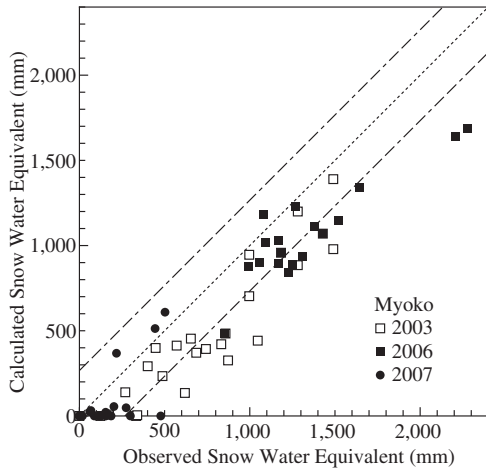Fig. 41 Comparison of observed and calculated SWE in the Kubiki Area.
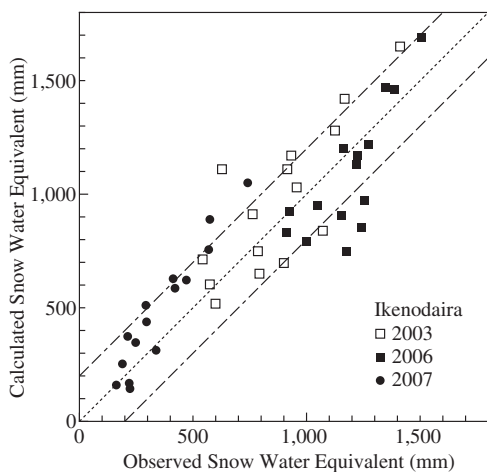
Fig. 42 Comparison of observed and calculated SWE in Ikenodaira Area.

Local snowfall anomalies have also been reported in this area by intensive snow surveys carried out during winter 2005-2006 to evaluate the damage caused by that winter's abnormally heavy snowfall (Yokoyama, 2006). The survey revealed that snow depth on the southeastern slope of Mount Myoko, where the Seki-Onsen point is located, was 20% larger than the average. Time series of SWE at all the observed points included in this area are shown in the Appendix 4C (**Figs.68-73**).

(4) Iiyama Area
In the Iiyama area, comparison of calculated and observed SWE showed that more than 80% of the data plotted within the 200 mm lines (**Fig. 46**). The discrepancies are likely due to the effects of local snowfall and strong winds. Time series of SWE at all observed points in this area are shown in the Appendix 4D (**Figs.74-78**).
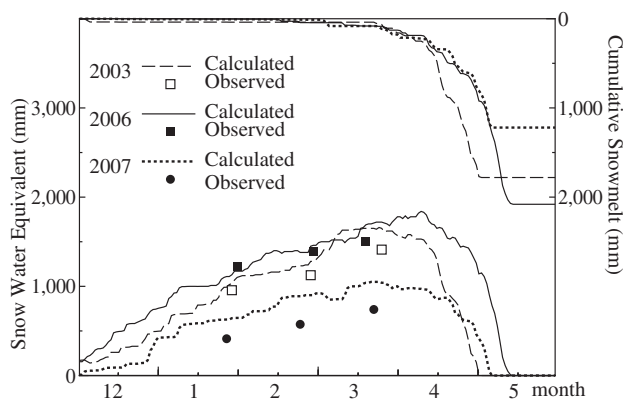
Fig. 43 Time series of observed and calculated SWE (bottom) and cumulative snowmelt (top) at Ikenodaira-Kaname (Stn. 2410; see **Fig. 49**).

4.4.3 Calculated river discharges after incorporation of the developed snowfall and snowmelt module

Simulations were performed with DWCM-AgWU after incorporation of the snowfall and snowmelt module, and then the calculated discharges during the winters (December through May) of 2004-2005 (**Fig. 47**) and 2005-2006 (**Fig. 48**) were compared with discharges observed at the Takada flow gauge (**Fig. 36**). The relative error (RE) and chi square error (CSE) for the entire calculation period (2003-2007) were 27% and 7.2 m^3/s, respectively; in winter 2004-2005, they were 19.4% and 4.5 m^3/s, respectively, and in winter 2005-2006, they were 24.6% and 9.2 m^3/s, respectively. Thus, as a result of incorporation of the module, DWCM-AgWU was able to represent well watershed-scale snowfall and snowmelt processes as a part of the natural hydrological cycle. In particular, the calculated maximum discharges, observed during periods of little or no precipitation, showed clearly that the skill level of the snowfall and snowmelt module is high.

4.5 Summary

In this section, the development of a snowfall and snowmelt module for calculation of daily snow accumulation and snowmelt from the simplified energy balance was presented. The module was then tested against observed SWE and river discharges in the study watershed. The results obtained are summarized as follows:

1) A simplified form of the energy balance was employed for application in an area with a relatively warm climate and abundant winter snow. So that the model could be applied at watershed scale, a novel approach was used to estimate the spatial distribution of the model parameters. Namely, remote sensing data were used to determine the snow-covered areas in regions where observed meteoro-

Fig. 44　Comparison of observed and calculated SWE in the Myoko Area.
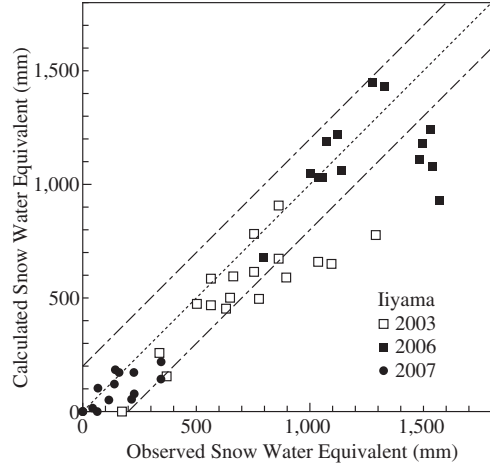
Fig. 46　Comparison of observed and calculated SWE in Iiyama Area.
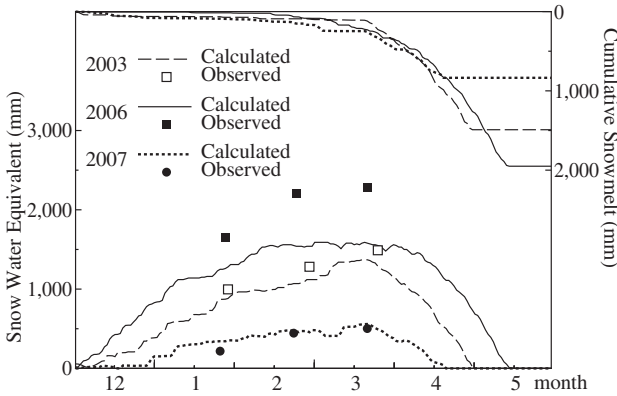
Fig. 45　Time series of observed and calculated SWE (bottom) and cumulative snowmelt (top) at Seki-Onsen (Stn. 2813; see Fig.49).

Fig. 47　Comparison of the calculated and observed discharge in winter 2004-2005.

Fig. 48　Comparison of the calculated and observed discharge in winter 2004-2005.

logical data were sparse.

2) The model was applied to the Seki River Basin, a representative snowy basin in an area of Japan with a relatively warm winter climate. Comparison of calculated and observed snow water equivalent (SWE) revealed that the model successfully represented the spatial distributions of SWE within ±200 mm, except in areas where locally intensive snowfall occurred.

3) In addition, river discharges calculated during snow-melt periods with DWCM-AgWU represented observed variations in flow with high accuracy.
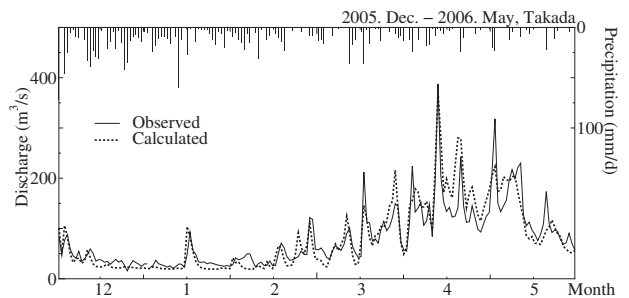
Appendix of Section 4

Fig. 49 Map of the Seki River Basin showing the snow survey points and their associated station numbers in the four areas.

Appendix 4A: Time series of SWE at all the observed points included in the Kubiki Area
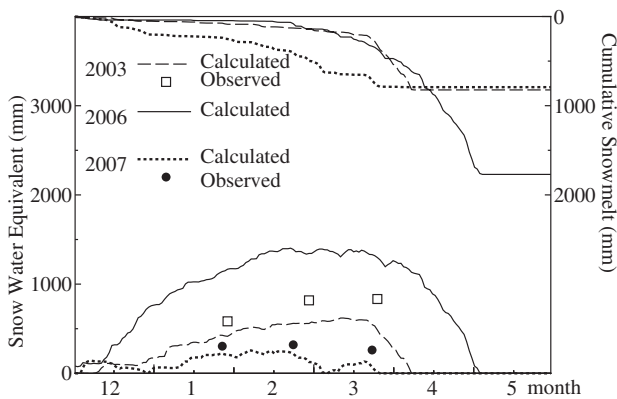
Fig. 50 Time series of observed and calculated SWE (bottom) and cumulative snowmelt (top) at Stn. 4742.
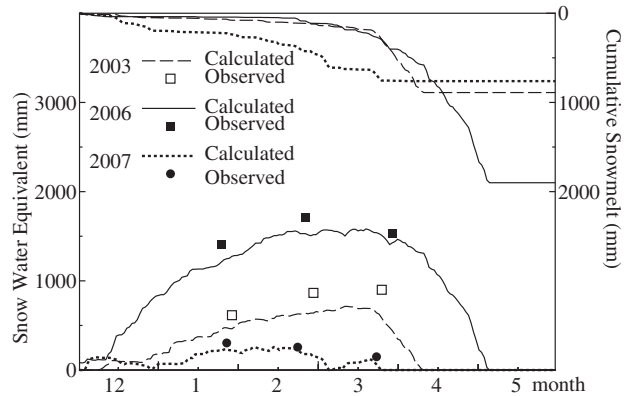
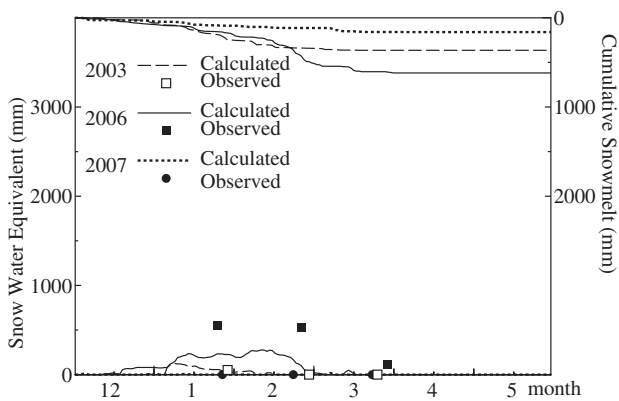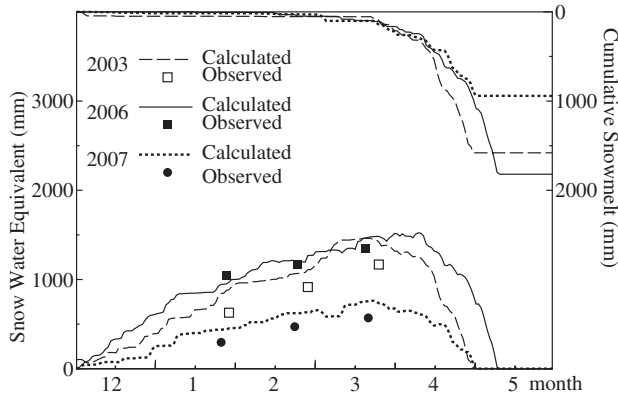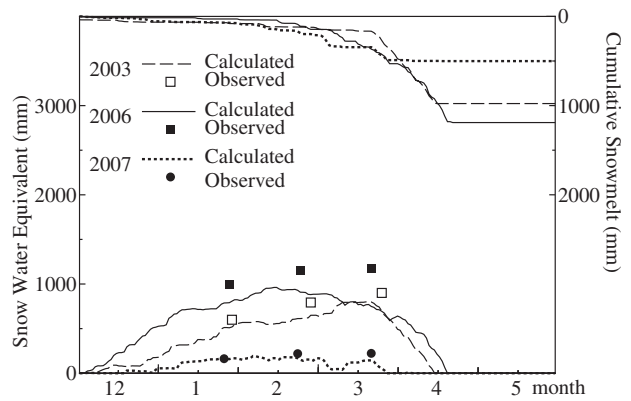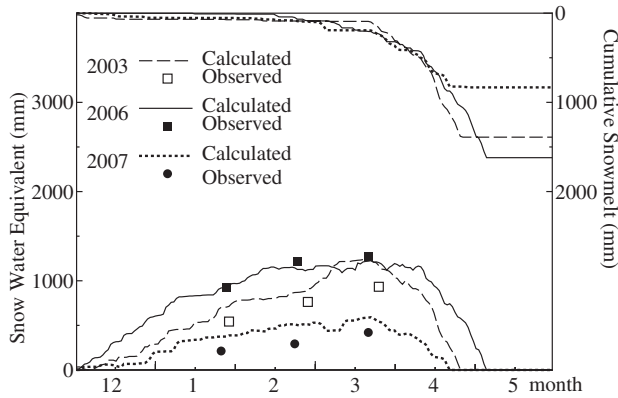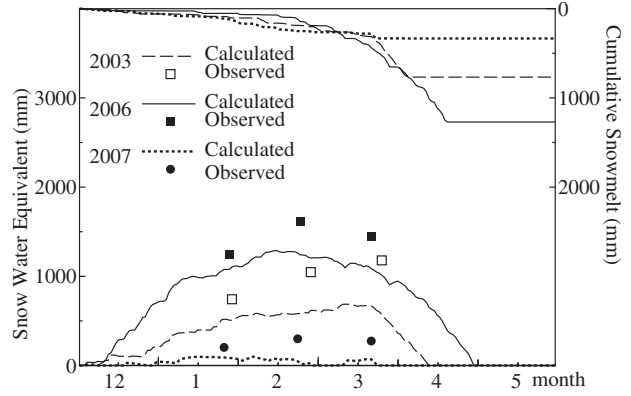**Fig. 51** Time series of observed and calculated SWE (bottom) and cumulative snowmelt (top) at Stn. 4638.
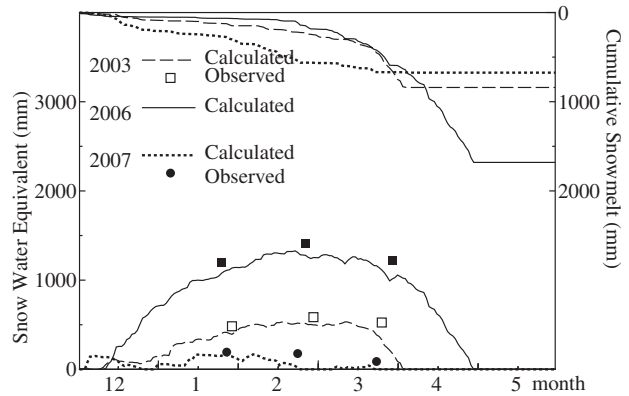
Fig. 52 Time series of observed and calculated SWE (bottom) and cumulative snowmelt (top) at Stn. 4939.
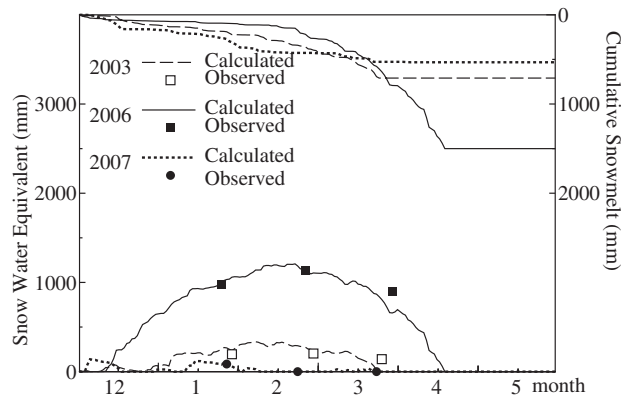
Fig. 53 Time series of observed and calculated SWE (bottom) and cumulative snowmelt (top) at Stn. 5137.
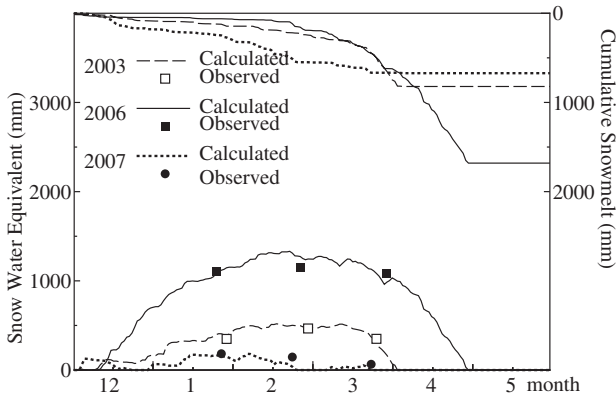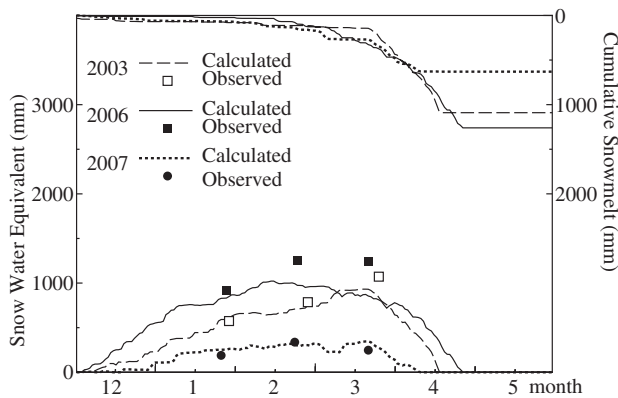
Fig. 54 Time series of observed and calculated SWE (bottom) and
cumulative snowmelt (top) at Stn. 5042.
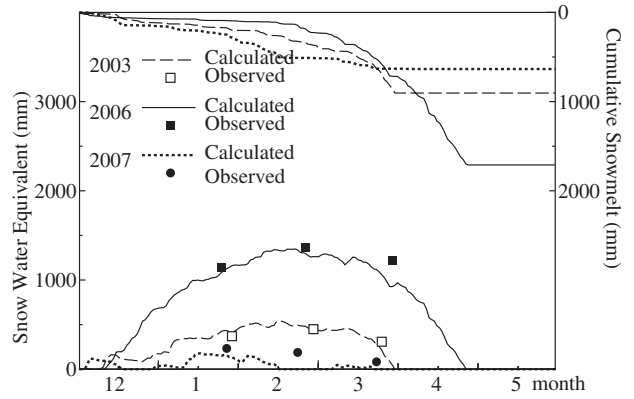
Fig. 57 Time series of observed and calculated SWE (bottom) and
cumulative snowmelt (top) at Stn. 5843.
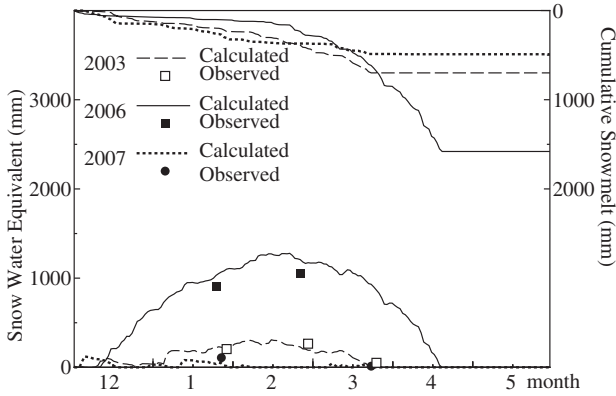
Fig. 55 Time series of observed and calculated SWE (bottom) and
cumulative snowmelt (top) at Stn. 5640.
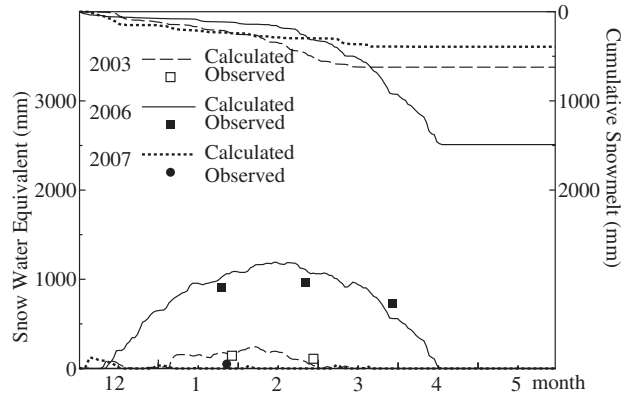
Fig. 58 Time series of observed and calculated SWE (bottom) and
cumulative snowmelt (top) at Stn. 5839.
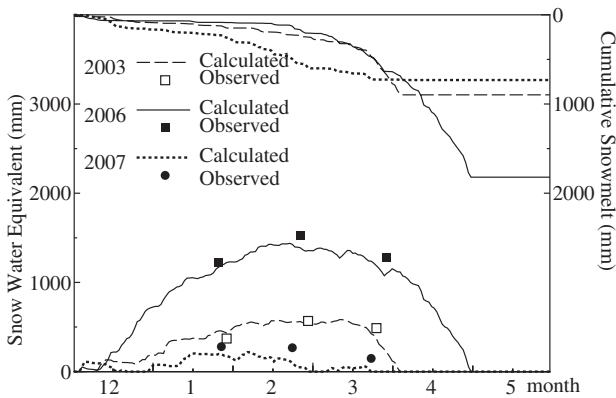
Fig. 56 Time series of observed and calculated SWE (bottom) and
cumulative snowmelt (top) at Stn. 5644.
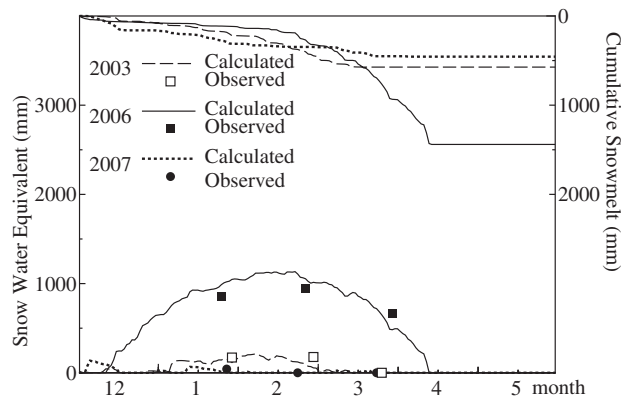
Fig. 59 Time series of observed and calculated SWE (bottom) and
cumulative snowmelt (top) at Stn. 5435.
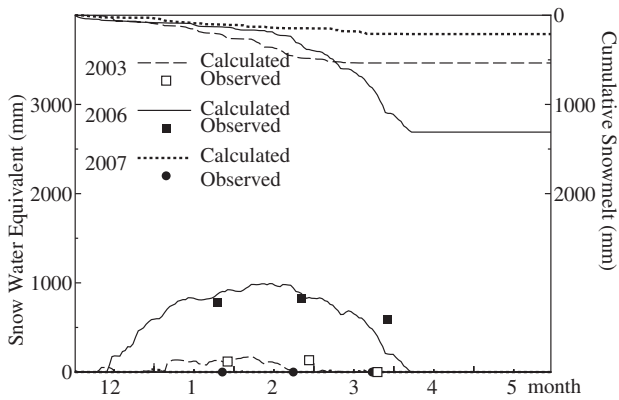
Fig. 60　Time series of observed and calculated SWE (bottom) and
　　　　　cumulative snowmelt (top) at Stn. 5433.
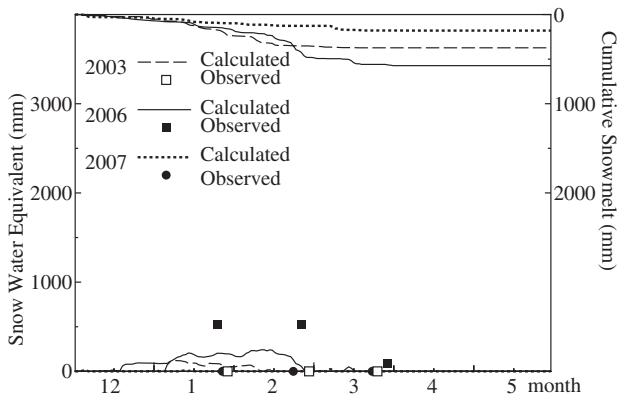
Fig. 61　Time series of observed and calculated SWE (bottom) and
　　　　　cumulative snowmelt (top) at Stn. 5832.

Fig. 62　Time series of observed and calculated SWE (bottom) and
　　　　　cumulative snowmelt (top) at Stn. 5530.

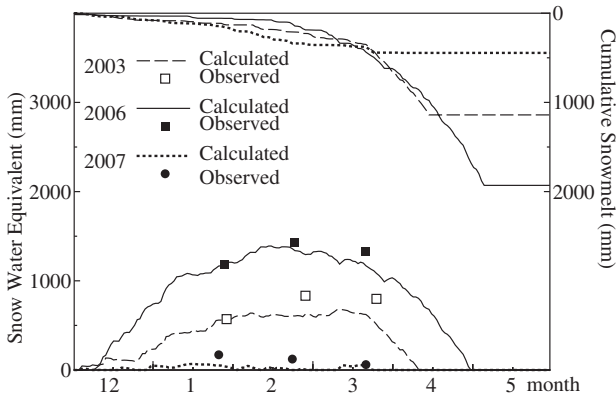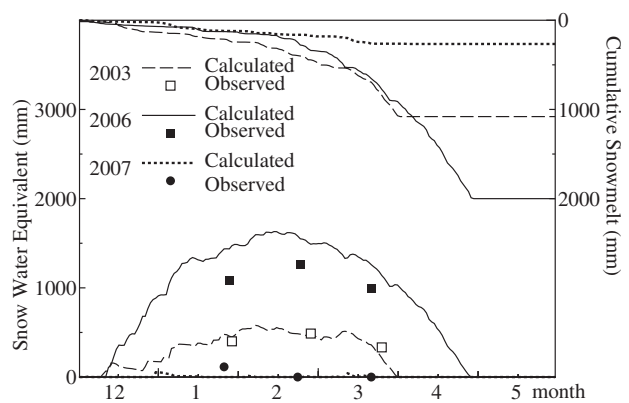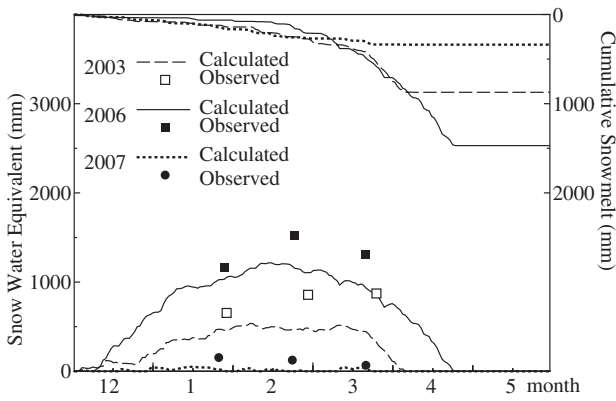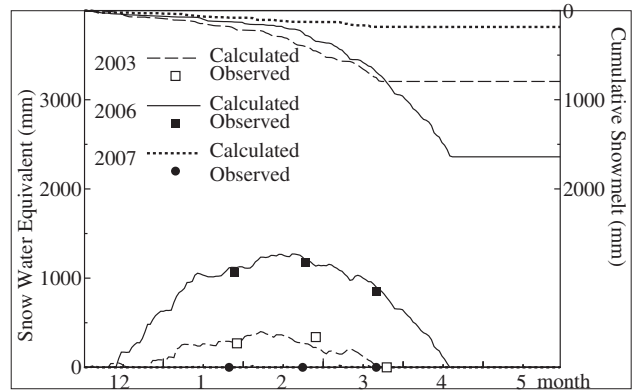## Appendix 4B: Time series of SWE at all the observed points included in the Ikenodaira Area

Fig. 63 Time series of observed and calculated SWE (bottom) and cumulative snowmelt (top) at Stn. 2411.

Fig. 66 Time series of observed and calculated SWE (bottom) and cumulative snowmelt (top) at Stn. 2314.
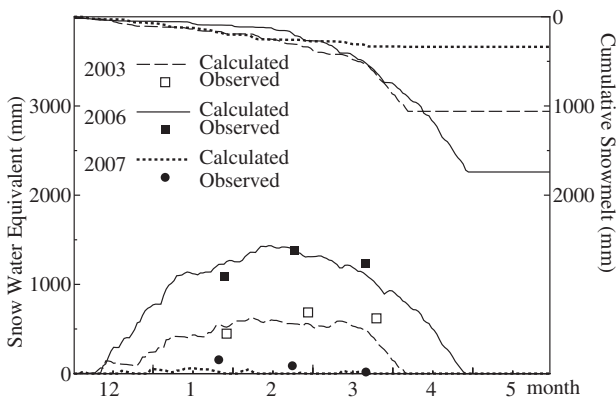

Fig. 64 Time series of observed and calculated SWE (bottom) and cumulative snowmelt (top) at Stn. 2412.

Fig. 67 Time series of observed and calculated SWE (bottom) and cumulative snowmelt (top) at Stn. 2616.
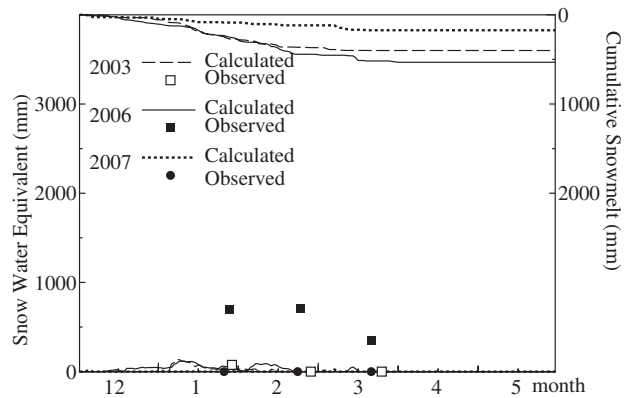

Fig. 65 Time series of observed and calculated SWE (bottom) and cumulative snowmelt (top) at Stn. 2313.

Appendix 4C: Time series of SWE at all the observed points included in the Myoko Area
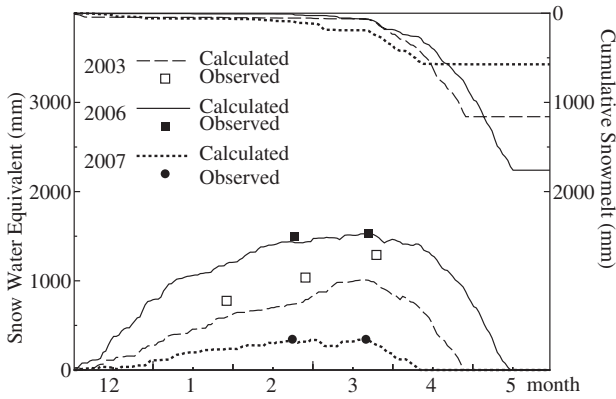

Fig. 68 Time series of observed and calculated SWE (bottom) and cumulative snowmelt (top) at Stn. 2917.

Fig. 71 Time series of observed and calculated SWE (bottom) and cumulative snowmelt (top) at Stn. 3917.

Fig. 69 Time series of observed and calculated SWE (bottom) and cumulative snowmelt (top) at Stn. 3116.

Fig. 72 Time series of observed and calculated SWE (bottom) and cumulative snowmelt (top) at Stn. 4218.

Fig. 70 Time series of observed and calculated SWE (bottom) and cumulative snowmelt (top) at Stn. 3417.

Fig. 73 Time series of observed and calculated SWE (bottom) and cumulative snowmelt (top) at Stn. 4721.

Appendix 4D: Time series of SWE at all the observed points included in the Iiyama Area

Fig. 74 Time series of observed and calculated SWE (bottom) and cumulative snowmelt (top) at Stn. 2524.
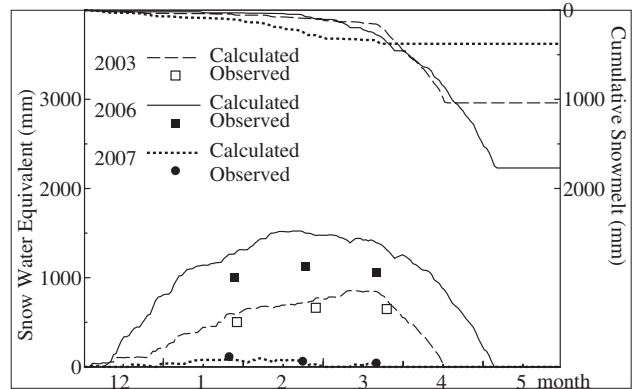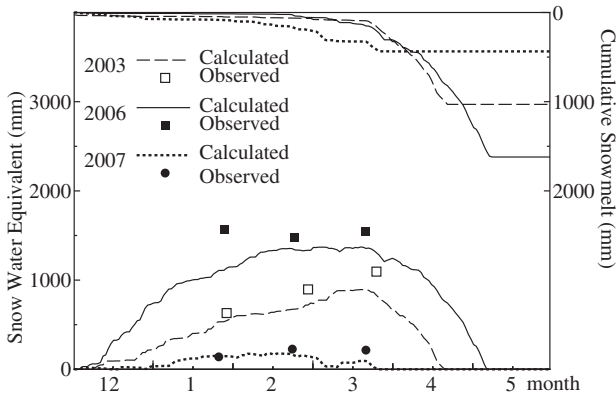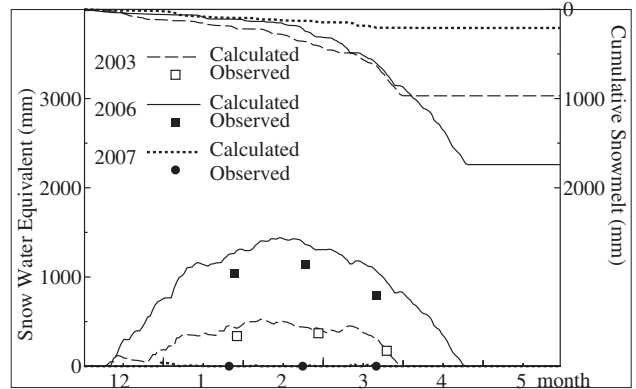

Fig. 77 Time series of observed and calculated SWE (bottom) and cumulative snowmelt (top) at Stn. 2924.

Fig. 75 Time series of observed and calculated SWE (bottom) and cumulative snowmelt (top) at Stn. 2525.

Fig. 78 Time series of observed and calculated SWE (bottom) and cumulative snowmelt (top) at Stn. 3621.
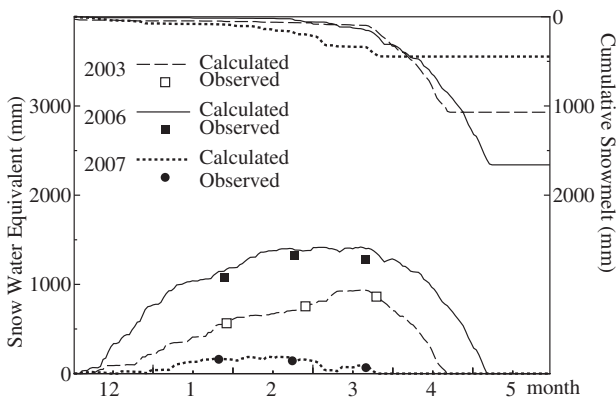

Fig. 76 Time series of observed and calculated SWE (bottom) and cumulative snowmelt (top) at Stn. 2726.

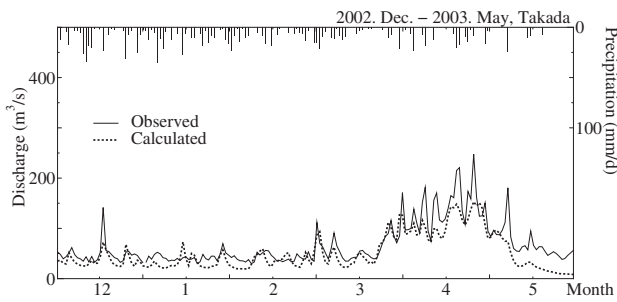## Appendix 4E: Hydrographs in winter (from December through May)

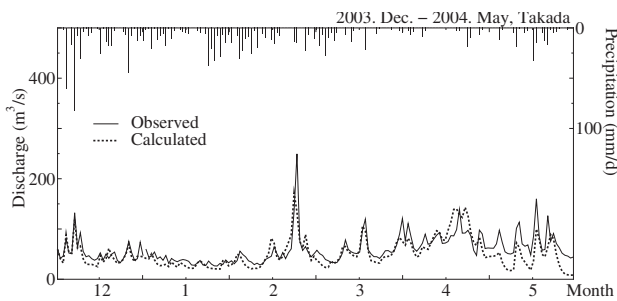**Fig. 79** Comparison of the calculated and observed discharges in winter 2002-2003.

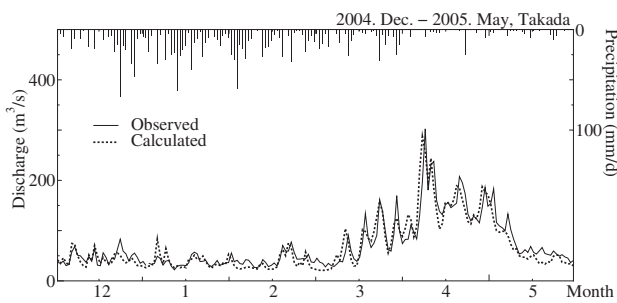**Fig. 80** Comparison of the calculated and observed discharges in winter 2003-2004.

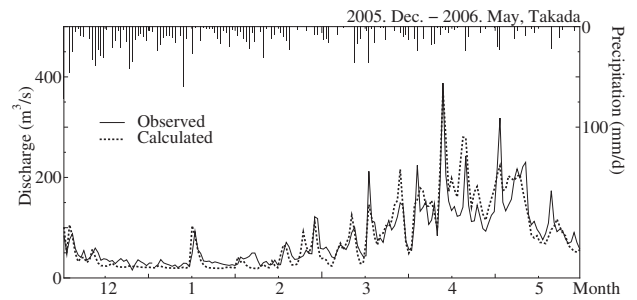**Fig. 81** Comparison of the calculated and observed discharges in winter 2004-2005.

Fig. 82 Comparison of the calculated and observed discharges in winter 2005-2006.
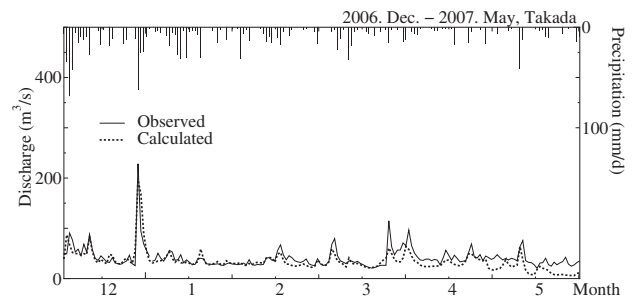

Fig. 83 Comparison of the calculated and observed discharges in winter 2006-2007.

5. Integration of an inundation module for low-gradient rivers into DWCM-AgWU

5.1 Introduction

An inundation process module was developed and integrated into DWCM-AgWU to help assess flood hazard. The module is based on a simple model that assumes that an inundated area is a reservoir, and that water levels in the reservoir and the surrounding area are equivalent. To apply the model, high-resolution digital elevation models, which are becoming available on a global scale, were used to extract detailed topographical features within the grid cells of DWCM-AgWU.

Floods are categorized as flash floods due to intense rainfall in mountainous areas and large-scale inundation of long duration in the lower part of a catchemnt. The inundation module represents the latter type of inundation, which can be triggered by long-lasting rainfall in the upper catchment and high water levels in connecting river to which water is drained.

5.2 Representation of inundation processes and its integration into DWCM-AgWU

5.2.1 Development of inundation module for low-gradient rivers

Kinematic wave models, in which wave speed is determined by the channel-bed slope and channel friction, can efficiently simulate wave propagation and water levels from topographic gradients. However, kinematic models do not account for inundation effects and may be difficult to use in areas with low relief, where flow regimes are strongly diffusive.

The simple model driving the inundation module assumes that there is no active water movement in the inundated area (Hayase and Kadoya, 1977; Masumoto and Kadoya, 1995). The inundation volume is calculated by using the relationship between the maximum conveyance capacity of rivers and detailed topographic data in the surrounding areas. Inundation level and volume are calculated using an equation of motion (described later) and the following continuity equation:

$$Q_{\text{out}}^{n+1} = \frac{W^{n+1} + W^n}{\Delta t}(H_{\text{in}}^n - H_{\text{in}}^{n+1}) + Q_{\text{in}}^{n+1} + Q_{\text{in}}^n - Q_{\text{out}}^n, \quad (73)$$

where Q_{in}^n and Q_{out}^n are the influx and efflux of the inundation area (m³/s), W^n is the inundation area (m²), H_{in}^n is the inundation depth (m), Δt is calculation time interval (3600 sec). Here, the suffix n and $n + 1$ denotes the number of calculation steps. To calculate the inundation depth H_{in}^n, the relation between H_{in}^n and the inundation volume, referred to as H-V curve, is derived from topographic data for the surrounding area.

The eflux from the inundation area Q_{out} (influx from connected rivers to inundation area if efflux is negative) is calculated for uniform ($\sqrt{F} > \sqrt{s}$) or non-uniform ($\sqrt{F} < \sqrt{s}$) flows with the following equation (Kadoya and Hayase, 1981).

$$Q_{\text{out}} = \begin{cases} G\sqrt{F} & (\sqrt{F} < \sqrt{s}) \\ G\sqrt{s} & (\sqrt{F} > \sqrt{s}), \end{cases} \quad (74)$$

where $G = \dfrac{A_{\text{in}}R_{\text{in}}^{2/3}}{N}$ and $\sqrt{F} = \dfrac{H_{\text{in}} - H_{\text{out}}}{\sqrt{X}\sqrt{|H_{\text{in}} - H_{\text{out}}|}}$; H_{out} is the water level of a channel to which water drained from an inundation area, X and s are respectively the length and slope of the connecting channel, A_{in} and R_{in} are respectively the cross sectional area and hydraulic radius of the channel, and N is a friction coefficient.

For nonuniform flow ($\sqrt{F} < \sqrt{s}$), the inundation depth at time $n + 1$, H_{in}^{n+1} is calculated from the inundation depth H_{in}^n at time n, the efflux from the inundation area Q_{out}^n, and the influx to the inundation area, Q_{in}^n and Q_{in}^{n+1} at times n and $n+1$. The runoff module in DWCM-AgWU provides the value of Q_{in}^{n+1}. The Newton-Raphson method is used to estimate H_{in}^{n+1} by the following procedures.

1) With Q_{out}^m denoting the m th iteration, Q_{out}^{m+1} is calculated with the following equation:

$$Q_{\text{out}}^{m+1} = Q_{\text{out}}^m + \left(\frac{\partial Q}{\partial G}\frac{dG}{dH_{\text{in}}}\right)^m dH_{\text{in}} + \left(\frac{\partial Q}{\partial F}\frac{dF}{dH_{\text{in}}}\right)^m dH_{\text{in}} \quad (75)$$

2) H_{in}^{m+1} is estimated by the following equation by assuming $W^{m+1} = W^m$, in which the continuity equation (73) and equation (75) are solved simultaneously

$$\left(\frac{W^m + W^n}{\Delta t} + D_G^m + D_F^m\right)H_{\text{in}}^{m+1} = \frac{W^m + W^n}{\Delta t}H_{\text{in}}^n +$$
$$(D_G^m + D_F^m)H_{\text{in}}^n - Q_{\text{out}}^m - Q_{\text{out}}^n + Q_{\text{in}}^{n+1} + Q_{\text{in}}^n, \quad (76)$$

where $D_G^m = \left(\frac{\partial Q}{\partial G}\frac{dG}{dh}\right)^m$ and $D_F^m = \left(\frac{\partial Q}{\partial F}\frac{dF}{dH_{\text{in}}}\right)^m$.

3) If $|H_{\text{in}}^{m+1} - H_{\text{in}}^m| > \varepsilon$, H_{in}^m is replaceed with H_{in}^{m+1} and process 1) is repeated until an acceptable solution is obtained ($|H_{\text{in}}^{m+1} - H_{\text{in}}^m| < \varepsilon$). Here, threshold for contraints was set at $\varepsilon = 0.001$ (m).

For uniform flow, the calculation proceeds by assuming $\sqrt{F} = \sqrt{s}$), and thus $D_F^m = 0$ in equation (76). In the same way as with nonuniform flow, H_{in}^{n+1} is approximated by repeated iteration of the following equation:

$$\left(\frac{W^m + W^n}{\Delta t} + D_G^m\right)H_{\text{in}}^{m+1} = \frac{W^m + W^n}{\Delta t}H_{\text{in}}^n + D_G^m H_{\text{in}}$$
$$-Q_{\text{out}}^m - Q_{\text{out}}^n + Q_{\text{in}}^{n+1} + Q_{\text{in}}^n \quad (77)$$

5.2.2 Integration of the inundation module into DWCM-AgWU

The runoff and inundation modules were integrated with the following assumptions to ensure seamless calculation of both runoff and inundation within the DWCM-AgWU framework.

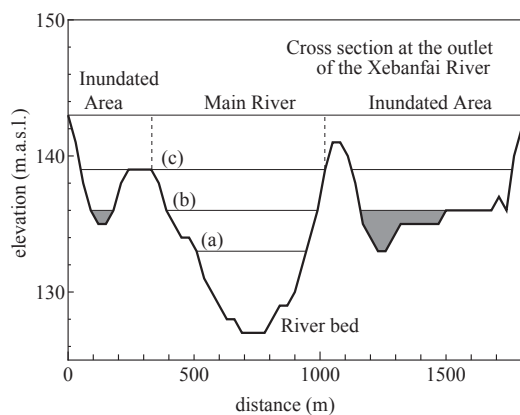First, to apply the inundation module, inundation

Fig. 84 Cross section of the outlet of the Xebanfai River showing schematics of the inundation calculation.

Fig. 85 Location map showing the Xebanfai River in the lower Mekong region.

points were selected from the grid cells of the DWCM-AgWU. Points should be selected for which detailed cross section and slope data are available. Next, the H-V curve for each point was created using topographic data. Even if the potential inundation area covered multiple grid cells, the inundation area was represented as a single reservoir and inundation water levels in all of its grid cells were treated as equivalent.

The inundation module was activated or deactivated by using the conveyance capacity at the inundation point, the calculated discharge at the inundation point, and the water level in the inundation area. The conveyance capacity was set as equivalent to the flow rate when the water level was at the level of the lowest bank (line (c) in **Fig. 84**), and was calculated by assuming uniform flow.

The inundation module was governed by the following three criteria.

1) The module is not activated when the discharge at the inundation point is less than the conveyance capacity (e.g., lines (a) and (b) in **Fig. 84**). Thus, this module permits only largescale inundation caused by water spilling over the banks of major rivers.

2) The module is activated when the discharge at the inundation point exceeds the conveyance capacity (line (c) in **Fig. 84**). The excess of surface flow above the conveyance capacity is allowed to expand the inundation area.

   The drainage from the inundation area is calculated by the method described in section 5.2.1, and the main river flow at the inundation point is replaced by the drainage from the inundation area. The cross section for drainage calculation is taken as the area between the dashed lines in **Fig. 84**, even if the inundation level is above line (c).

3) The module is active until the inundation level falls below the minimum elevation in the inundation areas (line (a) in **Fig. 84**). Even if the inundation level is below the lowest river bank (below line (c) in **Fig. 84**), the inundation level is assumed

to be equal to the water level in the main river.

5.3 Study watershed
5.3.1 Inundation in the study watershed

The inundation module was applied to daily data from the Xebanfai River, in the Lao PDR, from 2004 through 2008. The Xe- banfai River, a tributary of the Mekong River, drains an area of 10,330 km^2, and its elevation ranges from 130 to 1657 m.a.s.l. (**Figs.85** and **86**). The gradient in the upper reach, above Mahaxay, ranges from 1/2000 to 1/4000 (mean 1/3400), and in the reach below Mahaxay, the gradient is quite small (mean 1/7000). The gradient downstream from the Xebanfai Bridge is approximately 1/15,000. Paddy fields, which account for 23% of the total catchment area, are found predominantly in the lower catchment. Thus, prolonged flooding causes damage mainly to paddy areas and rural communities.

The average annual precipitation at Mahaxay is 2700 mm, most of which falls during the rainy season from May through October. Floods in this watershed are categorized as flash floods in the upper reach and large-scale inundation of long duration in the lower reach (Mekong River Commission, 2009). The inundation module represents the latter type of inundation, which can be caused by intense rainfall and high water levels in the Mekong River.

5.3.2 Data collection in the study watershed

Meteorological data were obtained from the Department of Meteorology and Hydrology, Water Resource$_s$ and Environmental Administration, Lao PDR. The data
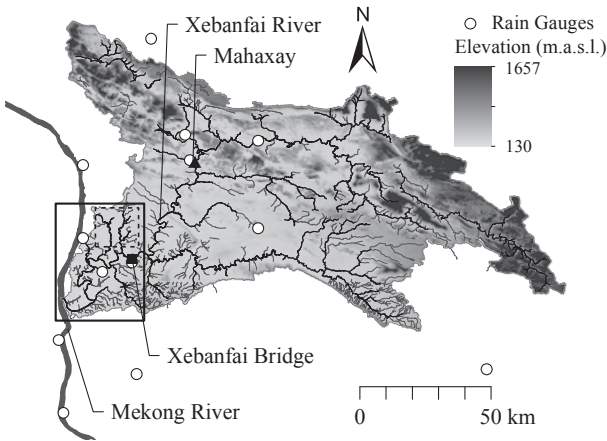
Fig. 86 Topography of the Xebanfai River basin showing locations of observation stations (open circles); dashed and solid lines denote the areas shown in Fig.89 and Fig.96, respectively.
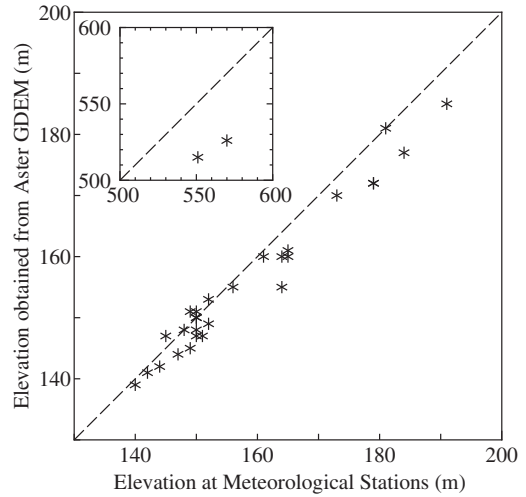

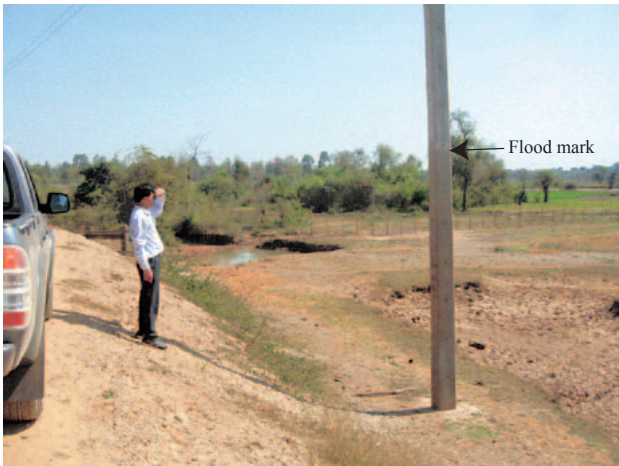**Fig. 88** Comparison of elevation data for meteorological stations from Aster GDEM and NGD DEM.

Fig. 87 Photograph of an inundation field survey locality.

Fig. 89 Representation of areas lower than 141 m.a.s.l. (gray) in (a) the NGD DEM and (b) the Aster GDEM in tributaries of the lower reach of the Xebanfai River (location shown in Fig.86).

included daily water levels and discharges at Mahaxay (catchment area 4520 km^2) and the Xebanfai Bridge (8539 km^2) and meteorological data from 13 observation stations (**Fig. 86**). These data were processed for model application by the method described in section 3.3.3.

Two types of topographic data were used: a digital elevation model (DEM) dataset provided by the National Geographic Department of Lao PDR (NGD DEM) and a global DEM (GDEM) of high-resolution topographic data based on observations from the Advanced Space-borne Thermal Emission and Reflection Radiometer (ASTER) instrument on the Terra satellite (Aster GDEM; Earth Remote Sensing Data Analysis Center, 2008). The NGD DEM uses elevation data obtained from field surveys, and it was interpolated into grid cells of 30 m spatial resolution. The Aster GDEM was generated from stereopairs of images acquired with nadir and backward angles over the same area.

Although high-resolution DEMs are becoming available at the global scale, the data are susceptible to speckle, or random noise. To investigate the validity of
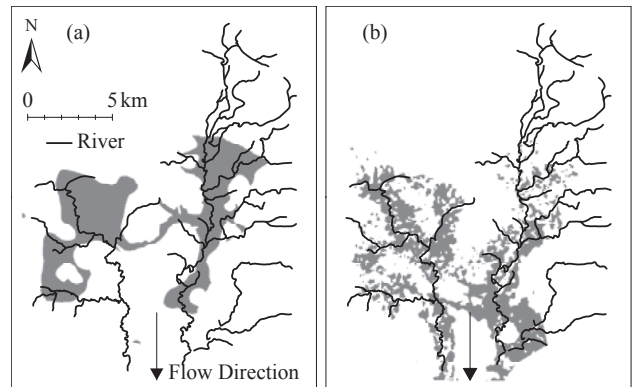
the Aster GDEM, it was compared to the NGD DEM with respect to specific landmarks and topography.

First, the elevations of the meteorological stations in **Fig. 86** were compared (**Fig. 88**). The root mean square error between the two DEMs was 11.5 m, and the discrepancy were relatively small in lower areas (140-160 m in elevation) and larger in higher areas (160-180 m). The elevations of the highest meteorological stations in the NGD DEM (551.2 m and 570.8 m) were 30 m higher than those in the Aster GDEM (515 m and 526 m).

Next, the topography represented by both datasets along a tributary to the lower Xebanfai River was compared. The shaded areas in **Fig. 89** represent the areas lower than 141 m.a.s.l. The shaded areas of the NGD DEM (**Fig. 89** (a)) did not cover the flow direction (downward in the figure), while those of the Aster GDEM corresponded to the flow direction (**Fig. 89** (b)).

The topography in the Aster GDEM was used for creating HV curves in the floodplains, and the NGD DEM was used for elevation data of each grid cell in the en-

tire watershed because of the low accuracy of Aster GDEM data in mountainous areas.

To validate the developed module, imagery from the Phased Array L-Band Synthetic Aperture Radar (PAL-SAR) sensor on the Advanced Land Observing Satellite (ALOS) was used. PALSAR instruments have the advantages of day-night operability (as active sensors), cloud penetration, and the ability to calibrate without performing atmospheric corrections. Where water is present, enhanced returns caused by specular scattering make it possible to distinguish between flooded and non-flooded areas (Kato and Yamazaki, 2010; Lowry et al., 2009). The spatial resolution of the imagery is 12.5 m. The imagery was acquired on 12 August 2008. Typhoon Kammuri crossed the region on 9 August and produced daily rainfall exceeding 200 mm.

5.4 Results and discussion
5.4.1 Application to the case study watershed

The inundation module was applied to daily data for the Xebanfai River from 2004 through 2008. Inundation points were introduced at Mahaxay, the Xebanfai Bridge, and at the confluence of the Xebanfai River with the Mekong River. The conveyance capacity at Mahaxay and the Xebanfai Bridge, calculated using the bank height at each point was $1822 m^3/s$ and $2649 m^3/s$, respectively.

The drainage rates from the two higher inundation areas were calculated by assuming uniform flow. However, the drainage rate at the outlet of the Xebanfai River was calculated using the water levels between the higher inundation areas and the Mekong River, as described in section 5.2.1. The Mekong River water level at its confluence with the Xebanfai River was estimated by interpolation between water levels at Thakek and Savannakhet, located 40 km upstream and 50 km downstream from the confluence, respectively (**Fig. 85**).

The highest water level during the analysis period was observed in 2005. The maximum level recorded at Mahaxay was 156.18 m, the second-highest level since 1991, which coincided with severe flooding damage in the Mahaxay District (Mekong River Commission, 2006).

5.4.2 River flows without the inundation module

The calculated discharge without the inundation module was compared with the observations at Mahaxay (**Fig. 90**) and the Xebanfai Bridge (**Fig. 91**) for a five-month period in 2005. The calculated peak discharge agreed with the observations in June and early July. However, the higher peak discharges in late July and August were overestimated, and the calculated timing of the peak and its recession were earlier than the observed dates.

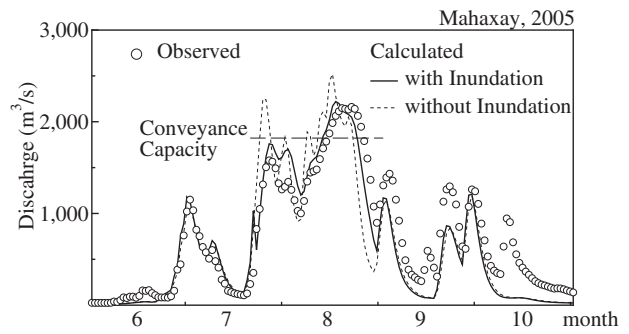In general, the calculated peaks matched the observed

Fig. 90 Observed discharges and calculated discharges with and without inundation processes atMahaxay from June through October 2005.
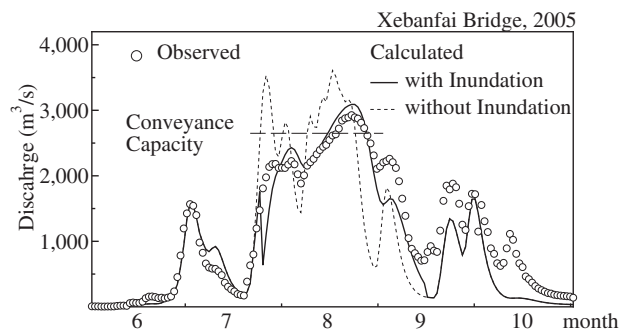

Fig. 91 Observed discharges and calculated discharges with and without inundation processes at Xebanfai Bridge from June through October 2005.
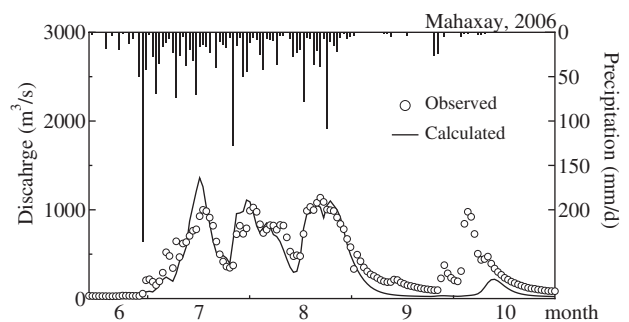

Fig. 92 Observed discharges and calculated discharges atMahaxay from June through October 2006.

ones well when the peaks were relatively small (e.g. in 2006, **Fig. 92**), although the calculated discharges did not always agree with the observations (e.g., in October in **Fig. 92**). It may be that the network of rain gauges was not sufficiently dense to capture all of the precipitation events in the watershed.

5.4.3 River flows with the inundation module

The observed discharges were also compared to discharges calculated using the inundation module. The calculated discharge decreased when the inundation module was activated because the water level in the river was forced to match the water levels in inundation areas. However, the module reproduced the observed discharges well, especially the peaks and timing of dis-
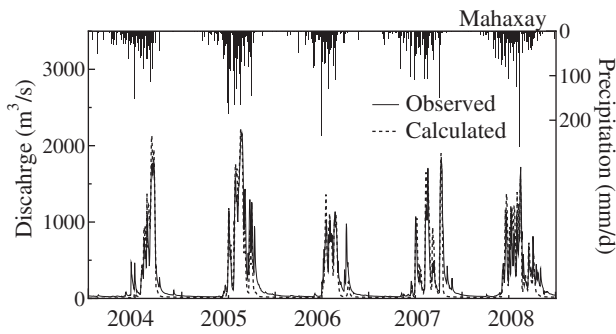
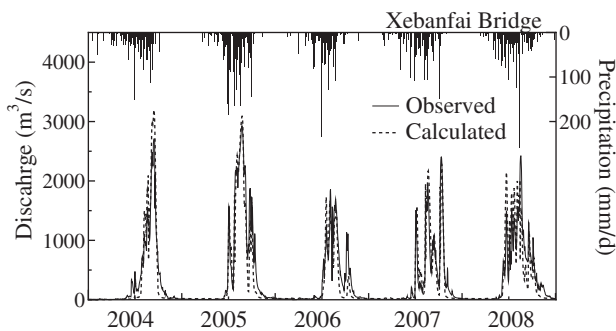**Fig. 93** Observed discharges and calculated discharges at Mahaxay from 2004 through 2008.

Fig. 94 Observed discharges and calculated discharges at Xebanfai Bridge from 2004 through 2008.
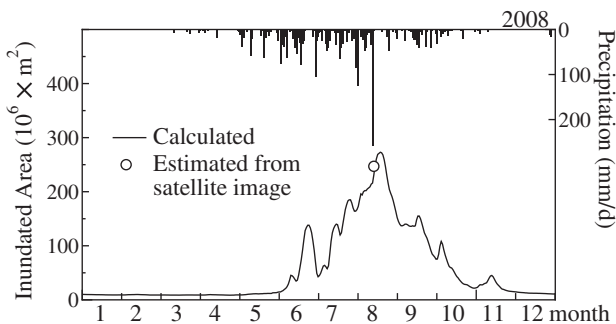

Fig. 95 Time series of inundated areas estimated at the outlet of the Xebanfai River in 2008.

charge. In 2005, the observed discharge at Mahaxay exceeded the conveyance capacity from 16 to 25 August and its peak was 2148 m³/s, whereas the calculated discharge exceeded the conveyance capacity from 13 to 23 August and its peak was 2220 m³/s (**Fig. 90**). Similarly, the observed discharge at the Xebanfai Bridge exceeded the conveyance capacity from 16 to 27 August and its peak was 2926 m³/s, whereas the calculated discharge exceeded the conveyance capacity from 15 to 26 August and the peak was 3090 m³/s (**Fig. 91**).

Next, the discharges calculated with the inundation module were compared with the observed discharges for the entire analysis period. The results were a close match at Mahaxay (**Fig. 93**) and the Xebanfai Bridge (**Fig. 94**). It should be noted that the calculated discharges exceeded the conveyance capacity only in 2004 and 2005. The relative errors were 48% and 47%, and
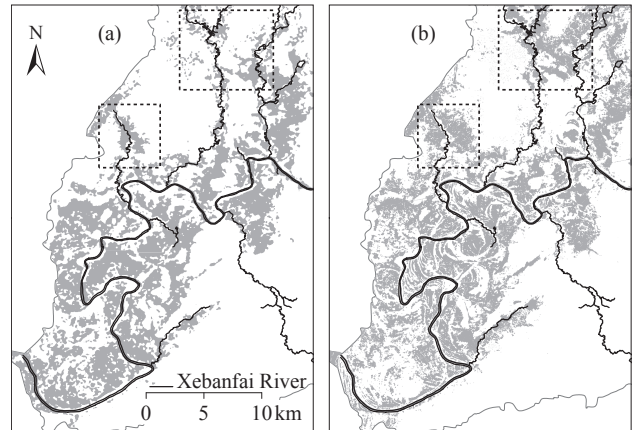

Fig. 96 (a) Calculated and (b) satellite-based inundation areas on 12 August 2008 of the lower reach of the Xebanfai River (location shown in Fig.86).

the chi square errors were 154 m³/s and 226 m³/s at Mahaxay and the Xebanfai Bridge, respectively.

Next, the spatial extent of inundation simulated by the model was compared with the satellite imagery. Good agreement was observed between the total area of inundation from calculations and the satellite imagery (**Fig. 95**). The simulated extent of inundation (**Fig. 96 (a)**) also showed good agreement with the remotely observed inundation areas (**Fig. 96 (a)**). However, the calculated area of inundation (265 km²) underestimated the observed area (250 km²). The source of the underestimation may be discrepancies in inundation of the watersheds of tributaries to the Xebanfai River, as outlined by the dashed lines in **Fig. 95**. The outlets of these subwatersheds were topographically constrained and acted as local inundation points that were not incorporated in the inundation module. Despite these discrepancies, the module succeeded in capturing the large-scale inundation by introducing simple assumptions into DWCM-AgWU, and hence the model enables better evaluations of the agricultural damage caused by flooding.

5.5 Summary

An inundation process module was developed and integrated into DWCM-AgWU. The integrated model was then tested by using data for the Xebanfai River basin in the Lao PDR. The results are summarized as follows:

1) The inundation process module markedly improved the performance of DWCM-AgWU in terms of calculated discharges, especially the timing and duration of peak flooding.

2) The module was validated against the 2008 episode of maximum inundation, as determined from ALOS/PALSAR images. The comparison confirmed that the module accurately reproduced large-scale inundation processes in the lower reaches of the watershed. Thus, the module is useful for evaluating agricultural damage caused by flooding.

Appendix of Section 5

Appendix 5A: Observed discharges and calculated discharges with/without inundation processes at the Mahaxay flow gauge
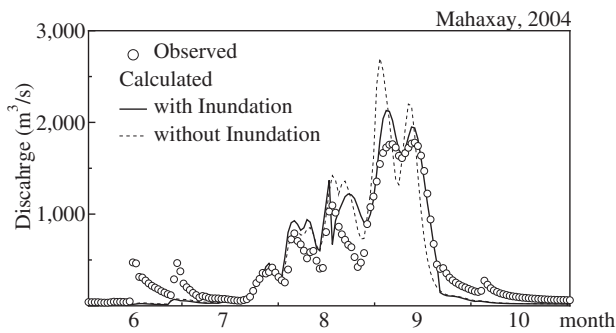

Fig. 97 Observed discharges and calculated discharges with and without inundation processes atMahaxay from June through October 2004.
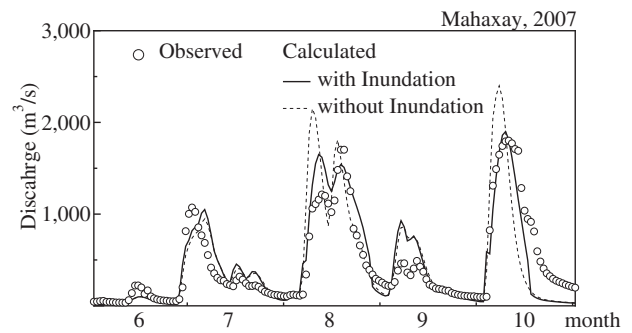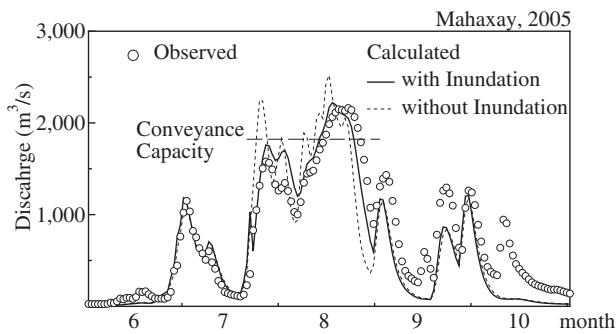

Fig. 98 Comparison of the observed and calculated discharges with/without inundation processes at the Mahaxay flow gauge from June through October, 2005.
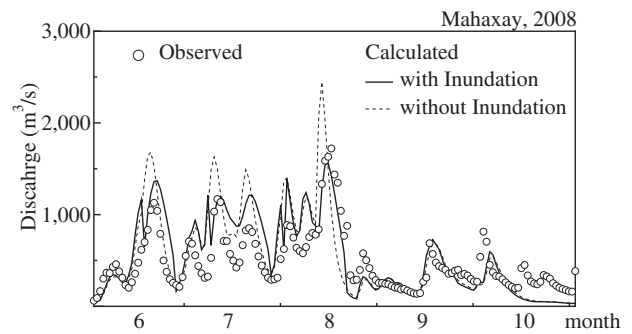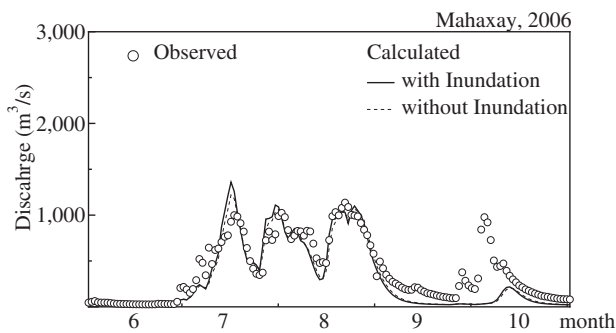

Fig. 99 Comparison of the observed and calculated discharges with/without inundation processes at the Mahaxay flow gauge from June through October, 2006.

Fig. 100 Comparison of the observed and calculated discharges with/without inundation processes at the Mahaxay flow gauge from June through October, 2007.

Fig. 101 Comparison of the observed and calculated discharges with/without inundation processes at the Mahaxay flow gauge from June through October, 2008.

Appendix 5B: Observed and calculated discharges with/without inundation processes at the Xebanfai Bridge flow gauge
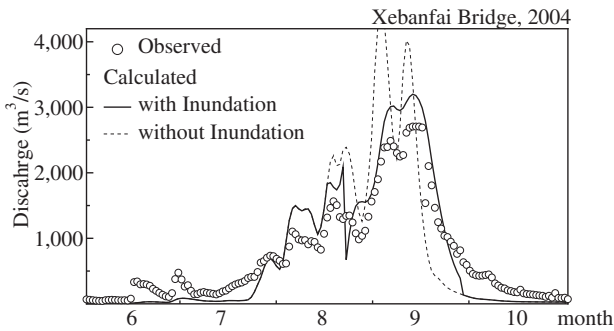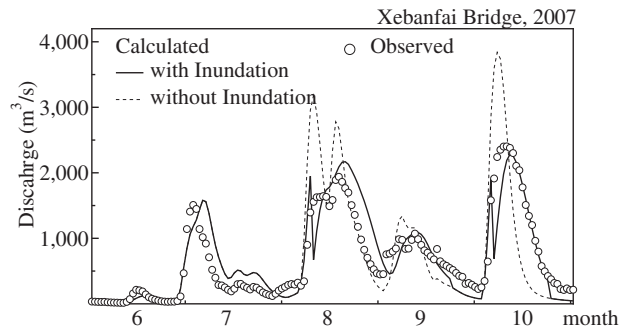

Fig. 102 Comparison of the observed and calculated discharges with/without inundation processes at the Mahaxay flow gauge from June through October, 2004.
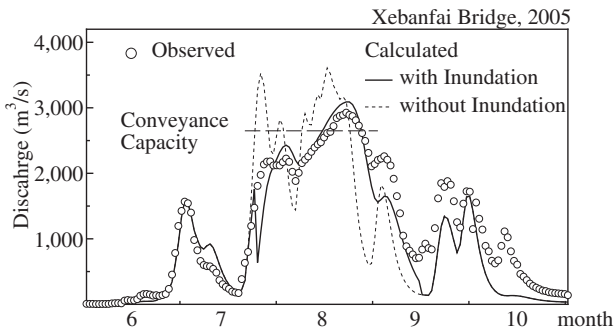

Fig. 103 Comparison of the observed and calculated discharges with/without inundation processes at the Mahaxay flow gauge from June through October, 2005.
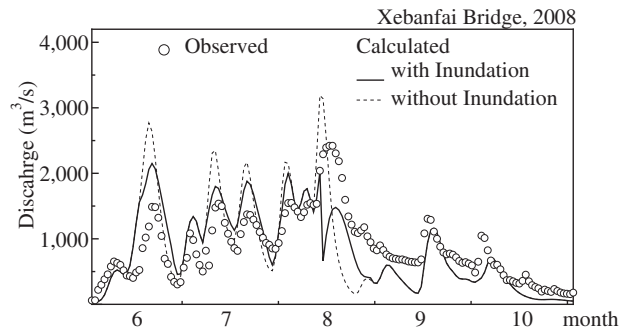

Fig. 104 Comparison of the observed and calculated discharges with/without inundation processes at the Mahaxay flow gauge from June through October, 2006.

Fig. 105 Comparison of the observed and calculated discharges with/without inundation processes at the Mahaxay flow gauge from June through October, 2007.

Fig. 106 Comparison of the observed and calculated discharges with/without inundation processes at the Mahaxay flow gauge from June through October, 2008
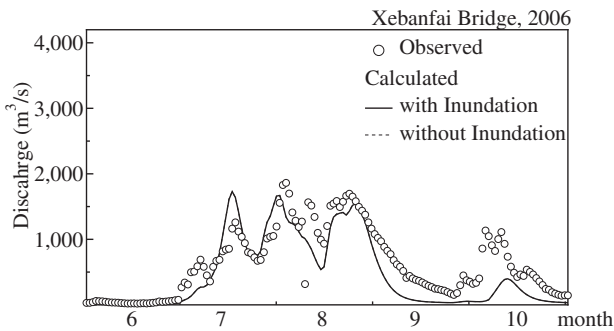
6. Short-term runoff modelling in hilly watersheds where paddy fields are prevalent

6.1 Introduction

In section 6, the ability of DWCM-AgWU was investigated to reproduce differences in runoff characteristics among watersheds. To assess the interaction between hydrological characteristics and paddy conditions, three experimental watersheds in Niigata Prefecture that were characterized by cultivated paddies, abandoned paddies, or forest were examined (**Fig. 107**).

6.2 Experimental watersheds and hydrological observation

6.2.1 Study area

The study area is in the Higashi-Kubiki region, which is a typical and active area for Tertiary strata landslides (Koide, 1973; Niigata University, 1987). The topography of the region is relatively gentle slopes ranging from 200 to 600 m in elevation. We examined three watersheds in the region that differ both in terms of land uses and land management of paddy fields.

The cropping season in the region starts in late May and ends in late September (**Fig. 108**). Irrigation systems in the area are mostly small-scale structures with direct intake from ephemeral streams or wells. Because the water for planting is mostly supplied by retaining snowmelt in paddies and small ponds, farmers prepare paddy fields by flooding them and tilling the soil to reduce the seepage from paddies (**Figs.109-112**).

In addition, the levees of rice paddies in this region are unique in height and thickness . The levees are approximately 40-50 cm tall, which allows rice to withstand dry spells of up to 1 month (Takeuchi, 1974). The farmers in the region retain as much water as possible to maintain a sufficient ponding level in the fields. Thus, they do not construct the levees lower to let water flow out in early summer, which is the typical management practice for irrigated paddies in Japan.

6.2.2 Selection of experimental watersheds

Fourteen watersheds were surveyed in Higashi Kubiki region (Hokuriku Regional Agricultural Administration Office, 2006). The land uses were delineated by using aerial photographs taken in 1989 and 2002 and through field surveys. The land uses in the watersheds were categorized as forest, cultivated paddies, or abandoned paddies. From these, three experimental watersheds were selected, each of which is characterized by cultivated paddies (cultivated-paddy watershed, CPW; no. 1 in **Fig. 113**), abandoned paddies (abandoned-paddy watershed, APW; no. 6 in **Fig. 113**), or forest (forested watershed, FW; no. 14 in **Fig. 113**). The specifications of each watershed are presented in **Table 2**.

CPW is 1.02 km^2 in area and ranges from 1/5 to 1/10
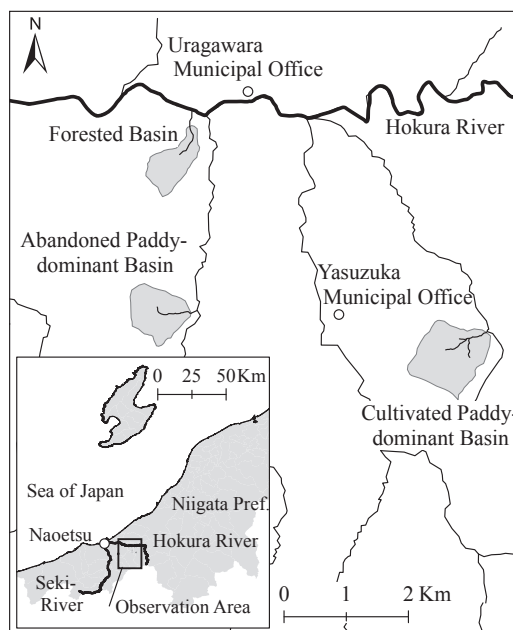

Fig. 107 Map of the Higashi-Kubiki region and experimental watersheds.

Fig. 108 View of the cultivated-paddy watershed during the cropping season.

in slope (**Fig. 114**). The areal ratio of cultivated paddies is about 29.4%, most of which are located in the upstream region of the watershed.

APW is 0.61 km^2 in area, and its slope is 1/7 and slightly steeper than that of CPW (**Fig. 115**). The watershed was covered by cultivated paddies 20 years ago, when the areal ratio of paddy fields exceeded 40%. However, most of the paddies are currently abandoned. The cultivated paddy are located only in the upstream of the watershed, where farmers can easily access them from the roads.

FW is 0.47 km^2 in area, the smallest watershed in the experimental watersheds (**Fig. 116**). The watershed is mostly covered by a Japanese cedar (*Cryptomeria japonica*) plantation of 30 years in age. Such plantations are typical in the study area, and the difference in forest conditions among the experimental watersheds are negligible.

Fig. 109 View of the cultivated-paddy watershed after puddling in autumn.

Fig. 111 Degraded levees and consequent steep slopes in the abandonedpaddy watershed.

Fig. 110 Water intake system from streams to cultivated paddies.

Fig. 112 View of the abandoned-paddy watershed immediately after snowmelt.

Table 2 Area of each land use (km2) and its ratio to the total area.

	Cultivated	Abandoned	Forest
Catchment Area	1.02	0.61	0.47
Paddy Field	0.37 (36.3)	0.24 (39.3)	0.02 (4.2)
Cultivated	0.30 (29.4)	0.05 (8.2)	0.02 (4.2)
Abandoned	0.07 (6.9)	0.19 (31.1)	0.00 (0.0)
Forest	0.65 (63.7)	0.37 (60.6)	0.45 (95.7)

Abbreviations:
Cultivated: Cultivated Paddy-dominant Watershed,
Abandoned: Abandoned Paddy-dominant Watershed,
Forest: Forest Watershed

The average slope in the experimental watersheds is approximately 1/7, and surface runoff velocities appear to be similar. The observed flood concentration times, which will be described later, also showed no significant differences among the watersheds. In this section, sub-surface storage capacity affects rainfallrunoff characteristics will be discussed later; therefore, the topographic features of each watershed were compared by using a topographic index computed in TOPMODEL (Beven and Kirkby, 1979). TOPMODEL calculates the topo-graphic index of hydrological similarity based on an analysis of the topographic data, which can be described as $\ln(a/\tan \beta)$, where a is the area draining through a point from upslope and $\tan \beta$ is the local slope angle. The index identifies areas with greater upslope contrib-uting area and lower gradient as being more likely to be saturated. The topographic index was evaluated with an algorithm proposed by Quinn et al. (1991). The evalu-ated topographic indexes in CPW and APW are illus-trated in **Fig. 117**, which shows similar frequency distri-butions, indicating that spatial differences in storage ca-pacity are small.

6.2.3 Hydrological observations and data analysis
(1) Hydrological observation in experimental water-sheds

Rainfall and discharge were observed at 10-min inter-vals in each watershed. The observations were con-ducted from June 2007 through November 2011 in APW and FW and from August 2007 through Novem-ber 2011 in CPW. Due to the heavy snowfall in this re-
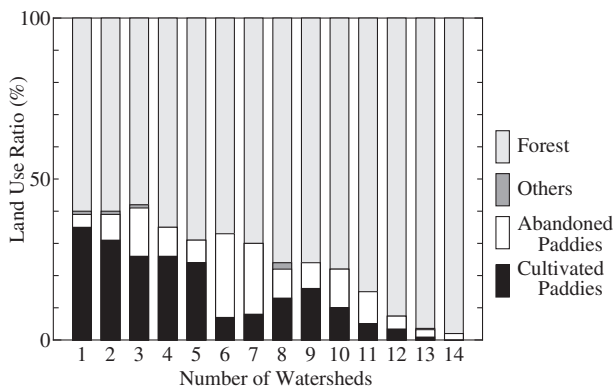
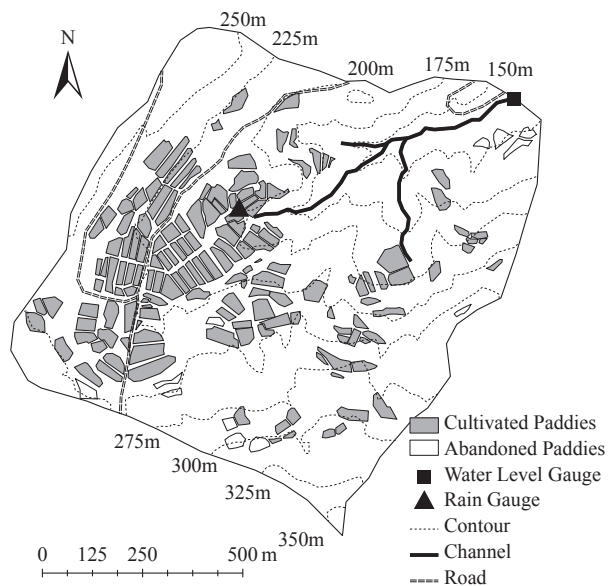Fig.113 Areal ratio of land uses in each watershed assessed for the selection of experimental watersheds.
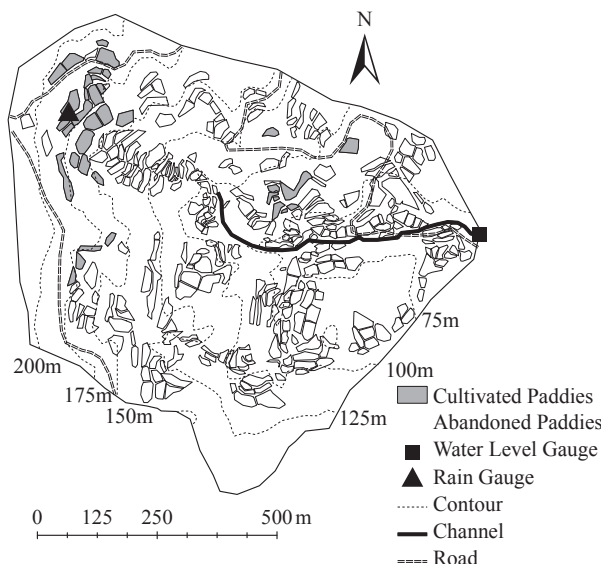

Fig. 115 Map of the abandoned-paddy watershed.

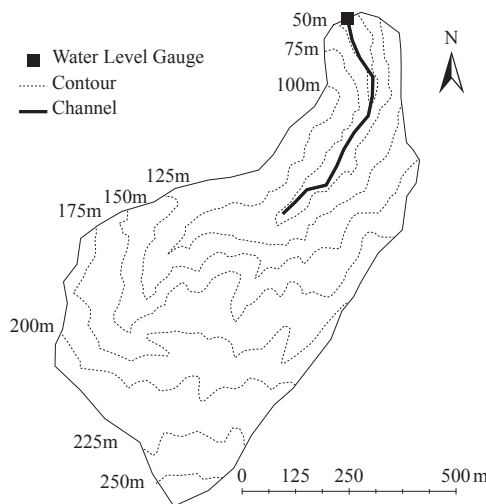Fig.114 Map of the cultivated-paddy watershed.

Fig. 116 Map of the forested watershed.

gion, we removed the rain gauges in winter, and replaced the missing data with the meteorological data gathered by the Automated Meteorological Data Acquisition System in Yasuzuka (see **Fig. 107**).

(2) Flood concentration times and peak runoff ratio

Flood concentration time (T_p) and peak runoff ratio (f_p) were analysed for the observed rainfall runoff events following the procedures presented by Kadoya and Fukushima (1976). Peak runoff ratio was defined as the ratio of the amount of discharge to precipitation during the flood concentration time.

The flood concentration time was visually determined from a hydrograph as follows. First, the point when peak discharge was observed was identified; and the rainfall intensity at that point was noted. We then looked backwards in time on the flood hydrograph to find a point when the same rainfall intensity was observed.

The flood concentration time is the period between the two identified points.

Next, the total precipitation (R) was obtained by summing the observed precipitation data during T_p; and converted peak discharge during T_p to effective rainfall (R_e, mm/h) by using equation (78).

$$R_e = \frac{3.6 \times Q_p}{A}, \tag{78}$$

where Q_p is peak discharge (m³/s), A is catchment area (km²).

Finally, the peak runoff ratio f_p was evaluated equation 79.

$$f_p = R_e / R \tag{79}$$

(3) Separation of direct runoff

The direct runoff from total runoff was visually separated as the quick runoff component, and compared it with total precipitation of each rainfall event. Here the runoff ratio is defined as the ratio of direct runoff to the total precipitation, and watershed retention as the
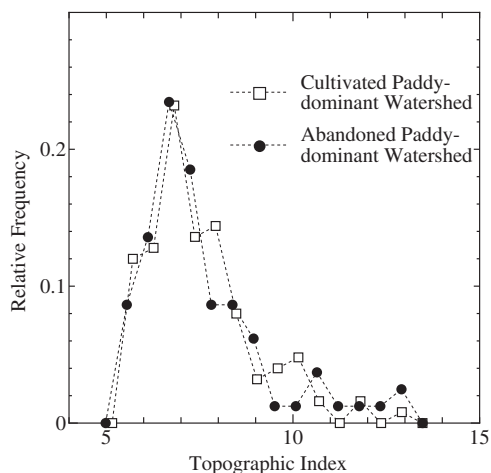
Fig. 117 Relative frequency distributions of topographic index in the cultivated- and abandoned-paddy watersheds
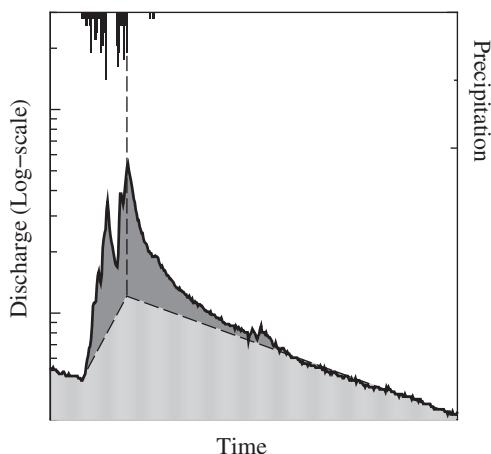

Fig. 118 Process for separating direct runoff using a storm hydrograph. Dark-shaded area represents the direct runoff as the amount of water.

amount of water that did not flow out as the direct runoff.

A storm hydrograph with a log-axis was used to separate the direct runoff. First, the recession line was extrapolated to the point when the peak discharge was observed. Next, it was connected to the point of initial discharge breakthrough in the storm hydrograph (**Fig. 118**). Then, the direct runoff was calculated as the amount of water above the line drawn by the previous procedures (dark-shaded area in **Fig. 118**). However, for the events without clear peaks and recession lines, the hydrograph was separated by using the horizontal line at the point of breakthrough of discharge to calculate the direct runoff.

6.3 Comparison of runoff characteristics based on paddy cultivation conditions
6.3.1 Comparison of runoff ratios

The short-term rainfall-runoff characteristics were analysed in the case of rainfall events that exceeded a
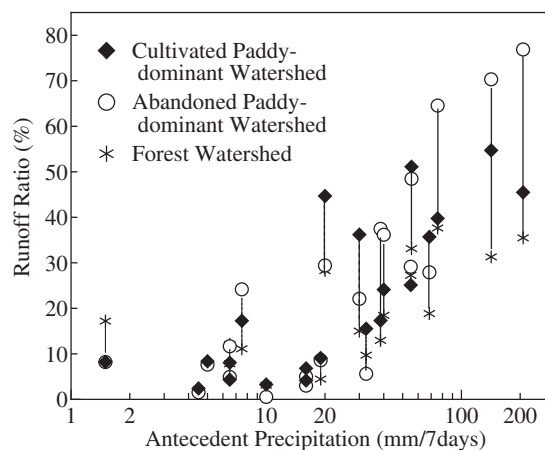

Fig. 119 Relationship between direct runoff ratios and antecedent precipitation for 7 days. Representative data were encircled with dashed line and corresponding rainfall numbers. The runoff ratios of each watershed in the same event are connected with lines.

daily precipitation of 20 mm and rainfall intensity of 5 mm/h. The observed rainfall-runoff events, including date, total precipitation (mm), runoff ratio (%), maximum rainfall intensity (mm/h), and peak discharge (mm/10 min), are summarized in **Table 3**. (Hereafter, we refer to a rainfall event that corresponds to the number x in **Table 3** as rainfall no.x.)

In **Fig. 119**, the runoff ratios are compared with the antecedent precipitation in the 7 days prior to each rainfall event. The difference in observed runoff ratios among watersheds was significant in wetter antecedent conditions (i.e., when precipitation exceeded 70 mm), whereas no significant difference was observed in drier antecedent conditions. In those wet events, the runoff ratios of APW were significantly higher than those of CPW, with a maximum difference of 31.4%.

6.3.2 Comparison of peak runoff coefficients

Table 4 summarizes flood concentration times (T_p, min), average rainfall intensity during flood concentration time (R, mm/h), effective rainfall intensity (R_e, mm/h), peak specific discharge (Q_p, m³/s/km²), and peak runoff coefficient (f_p). Although we should use data whose peak specific discharge exceeds 1 m³/s/km² for the evaluation of flood concentration time (Kadoya, 1980), due to data limitation we included smaller events as well. The peak specific discharge ranged from 0.34 to 1.82 m³/s/km² in CPW and from 0.60 to 1.91 m³/s/km² in APW; only two events (rainfall no. 13 and no. 14) in CPW and three events (rainfall no. 4, no. 13, and no. 14) in APW were valid in terms of the criterion.

Peak runoff coefficients differed according to antecedent moisture conditions and land use in the watersheds. The maximum peak runoff coefficient was observed during rainfall no. 14 in both CPW and APW, and the

Table 3 Observed short-term rainfall-runoff characteristics in the experimental watersheds

No.	date	Cultivated Paddy-dominant					Abandoned Paddy-dominant				Forest			
		Ant.	Prc.	Rat.	Int.	Peak	Prc.	Rat.	Int.	Peak	Prc.	Rat.	Int.	Peak
	2007													
1	22 Aug.	6.5	37.0	4.3	21.5	0.213	32.5	4.9	18.0	0.206	23.0	7.8	12.0	0.171
2	28 Aug.	32.5	42.5	15.5	8.5	0.142	48.0	5.6	9.5	0.078	51.5	9.7	13.5	0.125
3	30 Aug.	30.0	50.0	36.2	11.5	0.145	48.0	22.1	12.0	0.149	46.0	15.0	9.0	0.171
4	5 Sep.	60.0	-	-	-	-	48.0	24.8	31.0	0.721	46.0	14.9	21.0	0.563
5	8 Oct.	19.0	44.0	9.1	6.0	0.043	50.0	8.6	6.5	0.056	56.0	4.5	4.0	0.042
6	26 Oct.	20.0	84.5	30.2	6.0	0.133	-	-	-	-	73.5	16.7	9.0	0.142
	2008													
7	20 May	4.5	22.5	2.4	6.0	0.008	22.5	1.6	6.5	0.014	-	-	-	-
8	23 Jun.	16.0	27.5	4.1	5.0	0.010	40.5	3.0	19.5	0.145	-	-	-	-
9	29 Jun.	40.0	82.5	24.1	9.5	0.239	82.5	36.2	9.5	0.267	78.0	18.5	6.5	0.204
10	8 Jul.	10.0	45.0	29.8	25.5	0.286	-	-	-	-	-	-	-	-
11	4 Aug.	5.0	27.5	1.4	20.0	0.055	27.5	7.6	20.0	0.406	-	-	-	-
12	15 Aug.	1.5	62.0	8.2	33.5	0.540	53.5	8.2	38.0	0.419	-	-	-	-
13	16 Aug.	55.0	64.5	25.1	34.0	0.967	70.0	29.1	38.0	1.017	94.5	27.2	35.5	1.895
14	19 Aug.	142.0	79.5	54.7	34.5	1.127	65.5	70.3	27.5	1.147	65.5	31.3	12.5	0.786
15	21 Aug.	223.5	51.0	45.5	13.5	0.540	54.5	76.9	16.0	0.780	51.0	35.5	9.5	0.622
16	25 Sep.	70.0	122.0	39.8	13.5	0.286	127.5	64.5	12.5	0.386	102.5	37.7	7.5	0.240
	2009													
17	17 May	16.0	24.5	6.8	7.0	0.040	24.0	5.0	7.5	0.053	23.5	5.1	5.5	0.047
18	31 May	10.0	20.5	3.3	4.0	0.007	20.5	0.5	4.5	0.008	22.5	3.1	3.5	0.021
19	22 Jun.	0.5	42.0	17.0	24.5	0.431	43.0	20.8	27.0	0.461	40.0	19.0	22.5	0.764
20	1 Jul.	7.5	46.0	17.3	7.0	0.139	57.5	24.2	11.0	0.209	45.0	11.1	8.0	0.204
21	9 Jul.	55.5	90.0	51.7	12.0	0.427	88.5	48.5	11.0	0.465	81.5	33.1	9.0	0.448
22	18 Jul.	23.0	47.0	36.6	17.5	0.497	44.5	29.4	16.0	0.423	47.0	28.3	8.5	0.398
23	8 Aug.	38.5	22.0	17.3	11.5	0.272	31.5	23.2	11.0	0.262	35.5	13.0	10.0	0.403
24	29 Aug.	6.5	22.5	8.0	6.5	0.077	26.5	11.7	8.5	0.096	26.5	12.1	9.5	0.161
25	3 Nov.	68.5	42.0	35.7	6.0	0.218	46.5	27.9	5.5	0.172	44.0	18.9	6.0	0.164
26	11 Nov.	0.0	58.0	26.4	3.5	0.275	52.5	24.0	6.5	0.145	50.0	14.6	5.5	0.178

Abbreviations and units:

Ant.: Antecedent Precipitation for 7 days (mm/7d), Prc.: Total Precipitation (mm), Rat.: Direct Runoff Ratio (%),
Int.: Maximum Rainfall Intensity (mm/h), Peak: Peak Discharge (mm/10min)

Table 4 Flood concentration times and peak runoff coefficients of cultivated- and abandoned-paddy watersheds.

No.	Cultivated Paddy-dominant					Abandoned Paddy-dominant				
	T_p	R	Q_p	R_e	f_p	T_p	R	Q_p	R_e	f_p
4	-	-	-	-	-	40	46.50	1.19	4.32	0.09
10	40	36.75	0.48	1.72	0.05	-	-	-	-	-
12	40	42.75	0.34	1.25	0.03	30	47.00	0.70	2.51	0.05
13	50	39.60	1.61	5.82	0.15	60	37.50	1.68	6.10	0.16
14	90	27.66	1.82	6.56	0.24	90	22.90	1.91	6.88	0.30
19	50	28.20	0.71	2.59	0.09	30	28.00	0.77	2.77	0.10
22	80	15.37	0.78	2.82	0.18	50	16.20	0.60	2.20	0.14

Abbreviations and units:

T_p: Flood Concentration Time (min), Q_p: Peak Discharge (m³/s/km²), f_p: Peak Runoff Coefficient
R, R_e: Average and Effective Rainfall Intensity within Flood Concentration Time (mm/h)

value in APW(0.30) was 1.25 times that in CPW (0.24). The total precipitation observed during rainfall no. 14 was 79.5 mm in CPW and 65.5 mm in APW, which implies that the difference would be larger if the total precipitation had been identical.

However, any significant difference could not be found between the observed peak runoff coefficients in other rainfall events, except for rainfall no. 22, which showed a larger peak runoff coefficient in CPW than in APW, which is the reverse of other events. Flood concentration time also did not show a clear difference between the watersheds, ranging from 40 to 90 min in CPW and 30 to 90 min in APW.

6.3.3 Comparison of retention characteristics

Fig. 120 illustrates the retention capacities of CPW and APW. In rainfall events up to 40 mm, most of the rainfall was stored; however, there were discrepancies in retention capacities as rainfall increased beyond that value. The maximum retention capacities estimated using the envelope curve were 52 mm for CPW, 61 mm for APW, and 64 mm for FW.

6.3.4 Changes in peak runoff coefficients and runoff with more abandoned paddies

As noted, observed peak runoff coefficients in APW exceeded those observed in CPW, except for rainfall no.
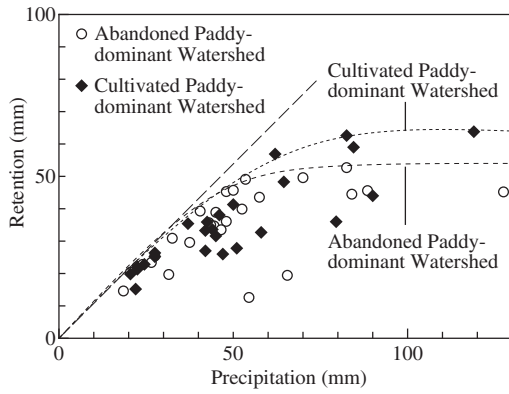
Fig. 120 Retention capacities of the cultivated- and abandoned-paddy watersheds.
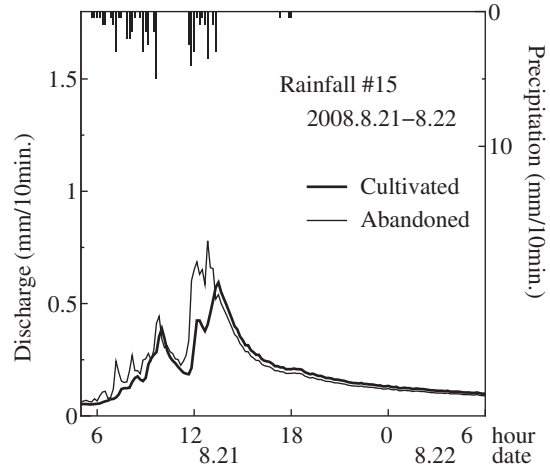

Fig. 121 Observed hydrograph for cultivated- and abandoned-paddy watersheds in rainfall no. 15.

Fig. 122 Observed hydrograph for cultivated- and abandoned-paddy watersheds in rainfall no. 16.

22, and the maximum value in APW was 1.25 times that in CPW (no. 14). The runoff ratio also showed higher values in APW as compared with CPW, especially for events with wet antecedent moisture conditions, and the maximum difference between CPW and APW was 31.4% (no. 15).

Here, the runoff characteristics of both watersheds were compared using the data observed in rainfall no. 15 and no. 16, which were typical events that showed clear differences in the runoff ratios.

Rainfall no. 15 occurred on 21 August 2008 (**Fig. 121**). The 7-day antecedent precipitation exceeded 200 mm (223.5 mm for CPW and 207.5 mm for APW), most of which was attributable to the intense rainfall no. 12 and no. 13. The peak discharge for rainfall no. 16, on 26 September 2008, also occurred in wet watershed conditions. The total precipitation in rainfall no. 16 can be divided into that in the first half (up to 12:00 on 25 September) and the latter half. The 7-day antecedent precipitation (approximately 70 mm) and the precipitation in the first half of the event (70 mm for both watersheds) resulted in the total precipitation exceeding 140 mm before the peak flow was observed.

The precipitation that fell directly on the wet surface of abandoned paddies became surface runoff and flowed out through the pathways of degraded paddy levees. In CPW, however, part of the generated surface runoff was temporarily stored in paddy levees, resulting in differences in the peak runoff coefficients.

The rainfall intensity differed between rainfall no. 15 and no. 16, with relatively intense rainfall of 15 mm/h in no. 15 and only mm/h in no. 16 (**Fig. 122**). In other words, the increasing trend of runoff ratio under wet conditions did not depend on the rainfall intensity. However, the maximum rainfall intensity (38.0 mm/h) observed during our experimental period was equivalent to a return period of 5 years; thus, this conclusion may be limited to the range of our observations.
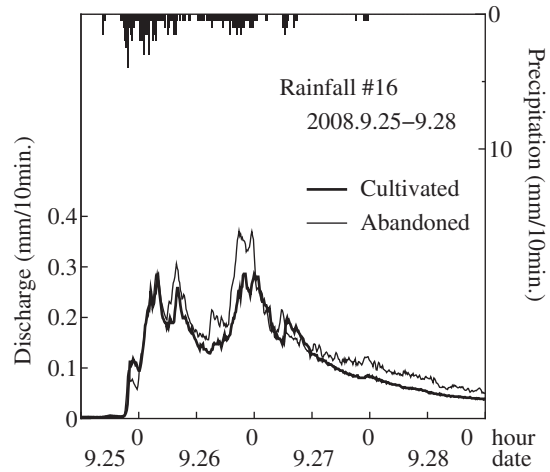
6.4 Rainfall-runoff modelling of watersheds characterized by terraced paddy

6.4.1 Modelling runoff processes in cultivated and abandoned paddies

(1) Runoff processes from cultivated paddies

The ponding depth governs the runoff process from cultivated paddies. Thus, the ponding depth of paddies were calculated in every grid cell, using simple water balance equations of precipitation, irrigation supply, evapotranspiration, infiltration, and runoff from the outlet. Runoff from the outlet was estimated by using the formula to calculate water flow over weirs.

Interviews with farmers revealed that the ponding depth was kept at the target level by an irrigation supply from ephemeral streams. Here, the irrigation supply (Q_a, m³/dt) was estimated; that is, in case the calculated ponding depth is below the target water level, farmers supply as much water as they need from streams. The model compares stream flow in a grid cell (Q_{cin}, m³/dt) and water requirement for paddies, which is the product of unit water requirement (Q_{rq}, m/dt) and paddy area

(A_{ir}, m^2), and determines Q_a as the smaller value of the two. In extremely severe drought conditions, the farmers pump up water from downstream paddies; however, such water management were not incorporated in this calculation.

(2) Runoff processes from abandoned paddies

Changes in the hydrological environment with the abandonment of paddy fields include not only levee degradation but also changes in soil properties, which are maintained through agricultural activities as mentioned above. Many studies have revealed the relationships between the surface hydrological environment and soil moisture conditions in abandoned paddies (Yoshida et al., 1997; Chiba et al., 1997). The soil properties in the Higashi-Kubiki region vary greatly following the repetition of drying and wetting. The observed changes include an increase in pore space during drying periods and a decrease during wetting periods. The effects of drying and wetting reach the soil base layer of paddies, which lies 25-30 cm below the surface, and during a severe dry spell permeability of the base layer had increased to approximately 10^{-4} cm/s from 10^{-7} cm/s (Yoshida et al., 1997). The changes in infiltration rate in an abandoned paddy plot were observed, and the rate decreased from 19 to 1 mm after a storm of 40 mm rainfall (Chiba et al., 1997).

However, upscaling these point- or plot-scale observations to the catchment scale is difficult due to the catchment's spatial heterogeneity. In equation (80), the maximum and minimum values of infiltration at the abandoned paddy surface were set; and a linear relationship between percolation from paddy surface and root zone storage were assumed:

$$I_{abn} = I_{min} + (I_{max} - I_{min})\left(1 - \frac{S_r}{S_{rmax}}\right), \qquad (80)$$

where I_{min} and I_{max} are minimum and maximum value of percolation rate at paddy surface, respectively. If data were available regarding the structure of the pore space, then other distributions or multimodal expressions could be applied, at the expense of introducing further parameters.

(3) Parameters for cultivated and abandoned paddy modules

The levee and outlet height of the cultivated and abandoned paddies were set based on field observations. The modelled levee and outlet height of the cultivated paddies are 400 and 300 mm, respectively, and those of the abandoned paddies are 100 and 30 mm. The water level of cultivated paddies is maintained such that it exceeds the target ponding depth of 50 mm. Maximum daily water intake for the cultivated paddies (Q_{rq}) is set to 10 mm/d for the period from 1 May through 15 Au-

gust.

The infiltration rate at the paddy surface in this region is relatively small due to the hydraulic conductivity below the paddies, which is on the order of 10^{-7} 10^{-6} cm/s. Therefore, we set the infiltration rate in cultivated paddies to 5 mm/d. Infiltration rate in the abandoned paddies, however, changes according to the development of large cracks during the drying periods and is modelled by using equation (80). The minimum and maximum values (I_{min} and I_{max}) were set at 5 and 25 mm/d, respectively. These values follow the referenced values in our study area, which were observed in an abandoned paddy field using a long-term record of water balance studies during a period that included extreme drought (Yoshida et al., 1997).

6.4.2 Initial conditions for short-term calculations

Our observations showed that initial moisture conditions affected the short-term rainfall-runoff characteristics. Although the initial conditions can be generated and optimized in lumped hydrological models, this is not be possible in distributed hydrological models because they require spatial representation of state variables based on physical processes. Therefore, the initial conditions for each rainfall event were determined by using the results of long-term calculation of the model:

1) The model parameters were calibrated for hydrogeological properties using the long-term rainfall and runoff data observed in FW. The parameters Q_{b0}, f_b, R_{c0}, f_r, and T_d can be determined by recession properties and base flow, whereas K_{sat} and ψ can be determined by peak flow.

2) The parameters obtained in process 1) and section 6.4.1 were applied to CPW and APW, while assuming that the subsurface properties are identical in the experimental watersheds.

3) Daily calculations were conducted throughout the observation period. The state variables of every grid cell in the model, which were root zone storage (S_r), unsaturated zone storage (S_u), deficit to saturation (D_s), and ponding depth of paddies (H_{pad}), for every rainfall event were saved.

4) The state variables obtained in process 3) were used as the initial conditions for the short-term calculations.

6.4.3 Model application to experimental watersheds

Grid cells of 100 m^2 in size were used for the application of DWCM-AgWU; and the grid cells including the watershed boundaries were assigned the actual area included in each grid cell. The number of grid cells was 125 for CPW and 81 for APW. Next, the average elevation for each grid cell was extracted using a digital elevation model of 50 m in spatial resolution, and determined flow directions following the steepest descent
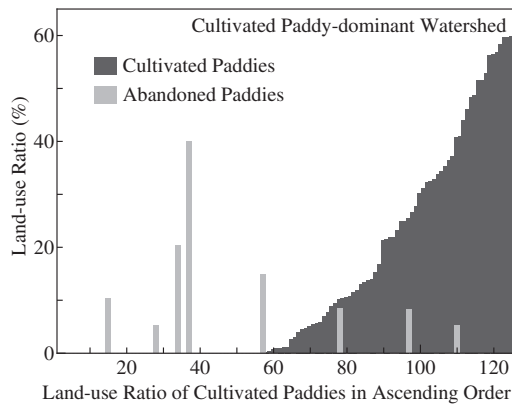
Fig. 123 Ratio of cultivated and abandoned paddy fields in each of the grids cells in the cultivated-paddy watershed (listed in ascending order of the ratio of cultivated paddy fields in each grid cell).
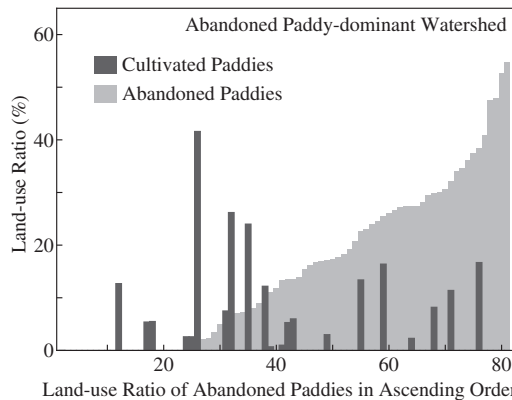

Fig. 124 Ratio of cultivated and abandoned paddy fields in each of the grids cells in the abandoned-paddy watershed (listed in ascending order of the ratio of abandoned paddy fields in each grid cell).

method. The areal ratios of cultivated and abandoned paddies in each of the grid cells for CPW and APW are shown in **Figs.123** and **124**.

Temporal resolution of the short-term calculation was set to 10 min, as the minimum flood concentration time of each watershed was 30 min. The land surface processes of evapotranspiration and snow melting were incorporated in the long-term calculation, but these processes were not incorporated in the short-term calculation because evapotranspiration during rainfall periods was negligible.

6.5 Results
6.5.1 Comparison of discharges and storage in unsaturated and saturated zones calculated at different time intervals

The results calculated at different time intervals (1 d and 10 min) were compared to assess the validity of the model. The results were those of two consecutive rainfall events, no. 9 and no. 10, in CPW; the calculation periods were 29 June to 7 July 2008 for rainfall no. 9 and 8 July to 13 July 2008 for rainfall no.10 (**Fig. 125**).

(a) Observed and calculated discharge

(b) Calculated storages in unsaturated and saturated zones
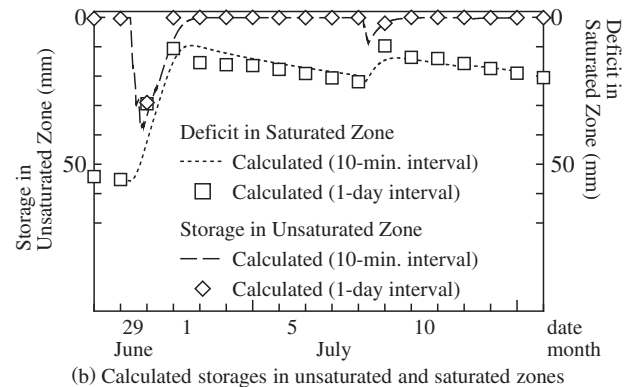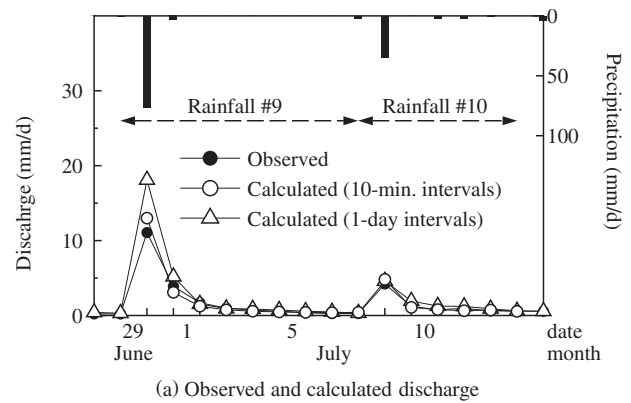
Fig. 125 (a) Discharges and (b) storage in unsaturated and saturated zones calculated at different time intervals. Discharges calculated at 10-min intervals shown in (a) represent aggregated discharges in a day.

First the calculated discharge of both time intervals were compared with the observed values (**Fig. 125** (a)). Both of the calculated discharges represented well the observed discharge except for the peak discharge in rainfall no. 9 on 29 June. This may be attributable to the sudden decrease of D_s in the calculation with the time interval of 1 h. The calculated decrease in D_s with the 1-d time interval was 10 mm larger than that of 10 min, which led to a larger volume of saturation excess overland flow. However, these discrepancies in peak discharge were not observed in rainfall no. 10, implying that they were limited to rainfall events with high intensity.

Then the calculated state variables D_s and S_u were compared in the same period (**Fig. 125** (b)). Because of the nonlinearity of the saturated zone calculation, there were some discrepancies between the results calculated at different time intervals. However, the discrepancies were negligible with regard to the estimation of initial conditions for short-term calculations, because differences in the initial conditions of D_s and S_u for rainfall no. 10 were 2.1 and 0.2 mm, respectively. Also, the overall representations of D_s and S_u were similar for both time intervals. These results indicate that the method is valid for estimating the initial conditions for short-term calculations utilizing the results from long-term calculations.
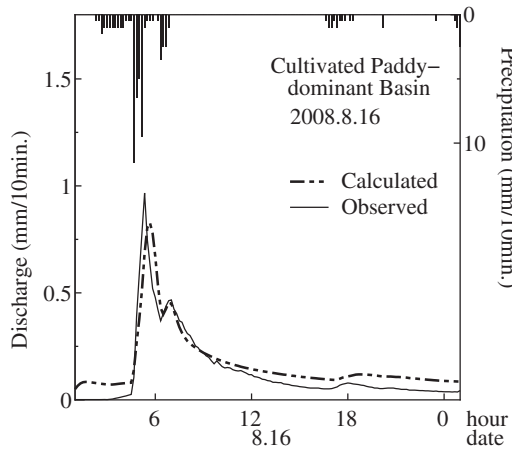
Fig. 126 Calculated discharge and observed precipitation in rainfall no. 13 (CPW)
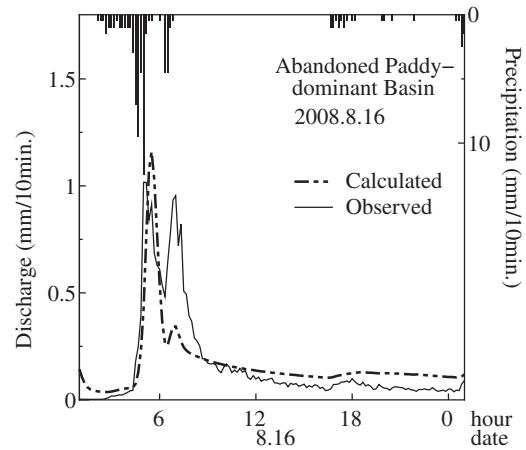

Fig. 127 Calculated discharge and observed precipitation in rainfall no. 13 (APW).
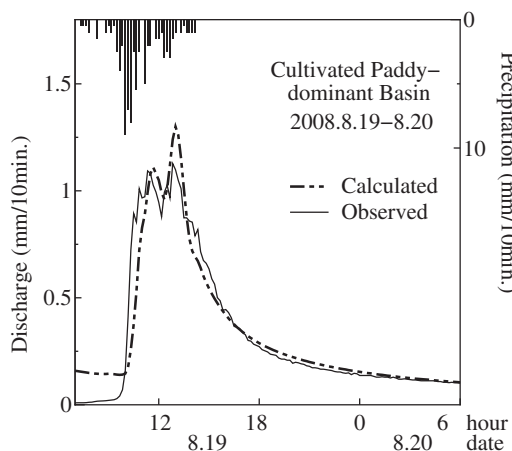

Fig. 128 Calculated discharge and observed precipitation in rainfall no. 14 (CPW)
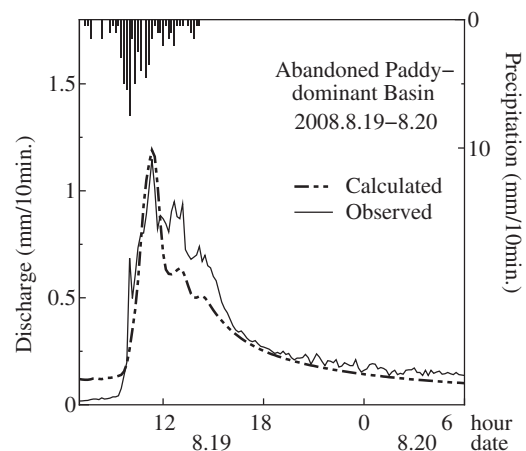

Fig. 129 Calculated discharge and observed precipitation in rainfall no. 14 (APW).
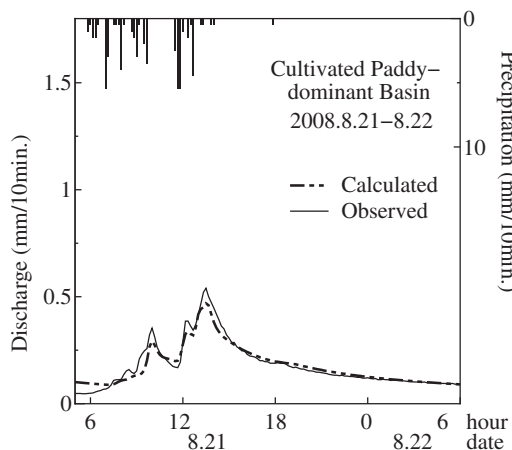

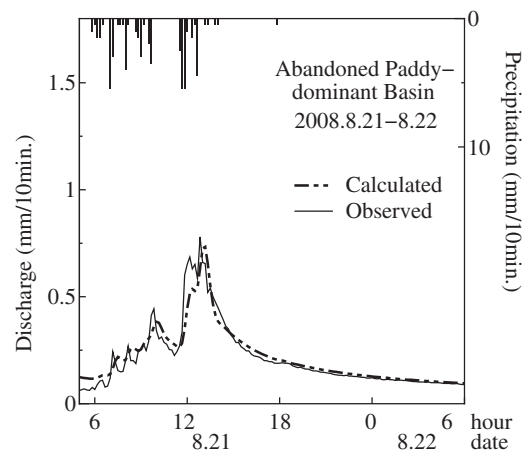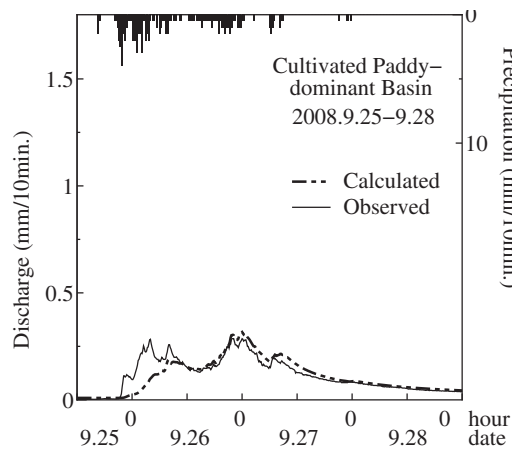**Fig. 130** Calculated discharge and observed precipitation in rainfall no. 15 (CPW)

Fig. 131 Calculated discharge and observed precipitation in rainfall no. 15 (APW)

6.5.2 Results of short-term runoff calculations and comparison with observed values

The calculated results for the selected rainfall events that exceeded the threshold described in section 6.4.2 are summarized in **Table 5**. The relative error in the table was calculated by using the following equation:

$$RE = \frac{1}{N} \sum_{t=1}^{N} \frac{|Q_{\text{obs}}(t) - Q_{\text{cal}}(t)|}{Q_{\text{obs}}(t)}, \tag{81}$$

where $Q_{\text{obs}}(t)$ and $Q_{\text{cal}}(t)$ are observed and calculated discharges, respectively, and N is the total time steps of the discharge data. The relative errors were calculated

Fig. 132 Calculated discharge and observed precipitation in rainfall no. 16 (CPW)
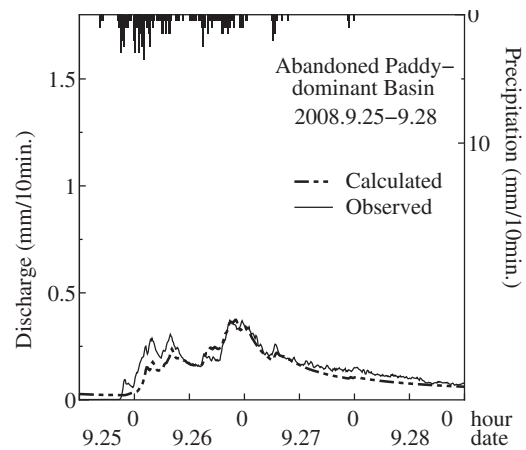
Fig. 133 Calculated discharge and observed precipitation in rainfall no. 16 (APW)

Table 5 Results of short-term runoff calculations for cultivated- and abandoned-paddy watersheds and comparison with the observed values.

| | | | Cultivated Paddy-dominant | | | | | | Abandoned Paddy-dominant | | | | | |
| | | | Observed | | | Calculated | | | Observed | | | Calculated | | |
No.	date	Ant.	Prc.	Peak	Roff	Peak	Roff	RE	Prc.	Peak	Roff	Peak	Roff	RE
	2007													
1	22 Aug.	6.5	37.0	0.213	3.2	0.015	1.8	25.1	32.5	0.206	3.1	0.050	2.3	33.2
2	28 Aug.	32.5	42.5	0.142	10.2	0.223	16.5	30.2	48.0	0.078	8.5	0.240	14.3	27.5
3	30 Aug.	30.0	48.0	0.145	16.2	0.054	11.1	28.4	48.0	0.149	10.8	0.053	9.5	25.3
4	5 Sep.	60.0	-	-	-	-	-	-	48.0	0.721	6.7	0.904	13.6	31.5
5	8 Oct.	19.0	44.0	0.043	5.2	0.034	5.1	25.4	50.0	0.056	12.3	0.036	6.2	29.3
6	26 Oct.	20.0	84.5	0.133	15.5	0.108	16.8	27.1	-	-	-	-	-	-
	2008													
7	20 May	4.5	22.5	0.008	0.5	0.004	1.7	36.5	22.5	0.014	0.9	0.022	2.9	32.6
8	23 Jun.	16.0	27.5	0.010	0.5	0.003	0.6	31.2	40.5	0.145	1.3	0.061	2.0	20.5
9	29 Jun.	40.0	82.5	0.239	14.7	0.285	14.6	27.6	82.5	0.267	23.5	0.104	21.4	30.4
10	8 Jul.	10.0	45.0	0.286	5.2	0.270	5.4	22.3	-	-	-	-	-	-
11	4 Aug.	5.0	27.5	0.055	0.4	0.117	2.4	20.4	27.5	0.406	2.4	0.230	3.6	24.5
12	15 Aug.	1.5	62.0	0.540	5.3	0.565	5.7	16.4	53.5	0.419	4.5	0.586	5.2	36.1
13	16 Aug.	55.0	64.5	0.967	29.4	1.106	21.2	14.2	70.0	1.017	37.5	1.227	56.6	23.6
14	19 Aug.	142.0	79.5	1.127	53.8	1.301	62.9	13.1	65.5	1.147	61.2	1.190	56.1	11.5
15	21 Aug.	223.5	51.0	0.540	41.6	0.466	42.5	15.8	54.5	0.780	45.6	0.807	42.5	19.8
16	25 Sep.	70.0	122.0	0.286	64.8	0.308	64.7	26.2	127.5	0.386	89.9	0.374	80.7	27.2
	2009													
17	17 May	16.0	24.5	0.040	0.8	0.015	0.7	35.3	24.0	0.053	0.9	0.002	0.3	21.3
18	31 May	10.0	20.5	0.007	4.3	0.003	1.5	45.2	20.5	0.008	2.5	0.026	2.0	36.2
19	22 Jun.	0.5	42.0	0.431	7.6	0.614	5.8	26.1	43.0	0.461	8.1	0.548	8.3	42.3
20	1 Jul.	7.5	46.0	0.139	7.8	0.036	8.3	23.9	57.5	0.209	13.4	0.063	15.4	36.1
21	9 Jul.	55.5	90.0	0.427	39.6	0.336	48.6	37.0	88.5	0.465	46.2	0.452	61.5	38.8
22	18 Jul.	23.0	47.0	0.497	30.0	0.438	43.1	33.9	44.5	0.423	29.1	0.301	33.6	27.5
23	8 Aug.	38.5	22.0	0.272	8.5	0.276	10.3	21.3	31.5	0.262	13.6	0.380	21.5	37.4
24	29 Aug.	6.5	22.5	0.077	2.5	0.114	5.9	34.9	26.5	0.096	1.8	0.124	6.5	34.2
25	3 Nov.	68.5	42.0	0.218	10.9	0.375	15.4	24.6	46.5	0.172	13.5	0.209	12.3	23.5
26	11 Nov.	0.0	58.0	0.275	15.9	0.453	35.1	30.8	52.5	0.145	13.8	0.119	20.5	43.5

Abbreviations and units:
　Ant.: Antecedent Precipitation for 7 days (mm/7d), Prc.: Total Precipitation (mm),
　Peak: Peak Discharge (mm/10min), Roff: Total Runoff (mm), RE: Relative Error (%)

during the period in which the observed discharge exceeded 0.02 mm/10min, to exclude relatively large errors associated with the low-flow data.

The evaluated relative errors ranged from 13.1% to 45.2% in CPW (mean, 25.7%) and from 11.5% to 42.3% in APW (mean, 29.6%). In terms of the volume of peak discharge, the larger events whose observed discharges exceeded 0.5 mm/10 min resulted in better representation; relative errors were 14.9%in CPW and 21.6% in APW (as depicted in **Figs. 126-131**).

Those events with smaller peak discharge, however, yielded relatively low accuracy. The relative errors were 29.2% and 31.4% for CPW and APW, respectively, which resulted from the smaller calculated discharges. As shown in **Fig. 132** and **Fig. 133**, the calculated discharges in the first half of rainfall no. 16 were underestimated, although the representation was improved in the latter half, when the cumulative precipitation exceeded 140 mm.

This underestimation for small events may be due to

the representation of saturated surface flow. This model generates both infiltration excess and saturation excess surface flows, and for small rainfall events in which infiltration excess does not occur, saturation excess surface flow is the dominant form. Despite the fact that small-scale saturated areas will emerge near river streams in the early stages of rainfall events, the model calculates the saturated area on a grid-cell basis, which is 100 m^2 here. For those small rainfall events in which the scale differences in saturated area were significant, calculated discharges tend to be underestimated for these reasons.

6.5.3 Initial conditions for short-term calculations

The calculated discharges in the long-term calculations are shown in **Fig. 134** to **Fig. 139**. The relative errors for the entire simulation period were 54%, 39%, and 38% for CPW, APW, and FW, respectively. The relative errors for the period without snow cover (i.e., excluding December to April) were 39%, 29%, and 29%, respectively. Thus, the errors in CPW were larger than those of the other watersheds in either case. These large errors in CPW were caused by the observation errors during low flows. The water level sensors in APW and FW were installed in artificial channels, whereas the sensor in CPW was in a natural stream, which was affected by sedimentation and natural fluctuation of stream lines. When the low-flow period (less than 0.5 mm/d) was eliminated from the evaluation period, a relative error of 31% was obtained in CPW.

As described in section 6.4.2, the model parameters for hydrogeological properties were calibrated using the long-term rainfall and runoff data observed in FW and applied the parameters to APW and CPW. The results of the calculations in both watersheds were acceptable in terms of long-term runoff, confirming the parameter transferability of the proposed model.

Here, the initial conditions were compared to assess how they affected the calculated runoff characteristics. **Fig. 140** illustrates the deficit in the saturated zone (D_s) from May through September 2008. The values shown in the figure are the maximum and average values over those grid cells in which paddies exist. The calculated D_s gradually decreased (i.e., water table was elevated) as the rainfall occurred in APW, whereas those in CPW remained relatively constant. Heavy rainfalls in late August brought sudden decreases in D_s, and the maximum D_s in APW approached zero, or complete saturation.

Fig. 142 shows the ponding depth in paddies (H_{pad}) for the same period illustrated in **Fig. 140**. Again, the values are the average over those grid cells in which paddies exist. The ponding depth was found to be remained fairly constant in CPW, whereas standing water disappeared in APW through infiltration and surface runoff from degraded levees.
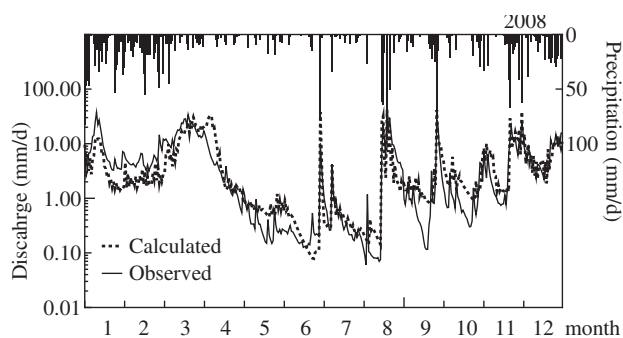
Fig. 134 Long-term observed and calculated hydrographs for cultivatedpaddy watershed (2008).
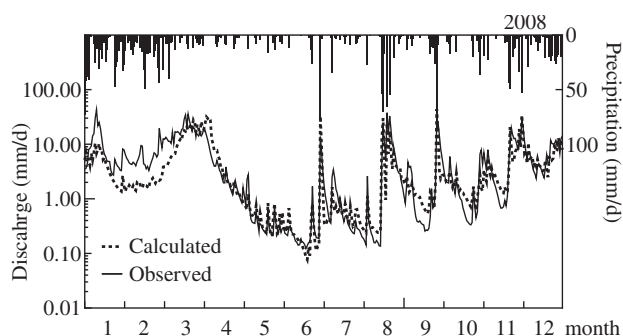
Fig. 135 Long-term observed and calculated hydrographs for abandoned-paddy watershed (2008).
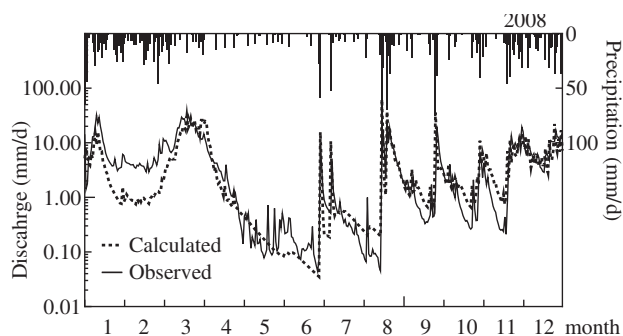
Fig. 136 Long-term observed and calculated hydrographs for forest watershed (2008).

6.5.4 Effects of initial soil wetness on short-term runoff characteristics

The initial soil wetness conditions differed, reflecting antecedent rainfall and catchment characteristics, as described in section 6.5.3. The effects of initial soil wetness on short-term runoff characteristics were investigated using two rainfall events: no. 14, which yielded the largest difference in peak runoff coefficients, and no. 13, whose peak runoff coefficients were similar in CPW and APW despite the rainfall intensity and amount being similar to those of rainfall no. 14.

The calculated peak coefficients for rainfall no. 13 were 0.12 for CPW and 0.14 for APW, whereas the observed peak coefficients were 0.15 and 0.16, respectively. The calculated peak coefficients for rainfall no. 14 were 0.18 for CPW and 0.23 for APW, whereas the observed peak coefficients were 0.24 and 0.30, respec-
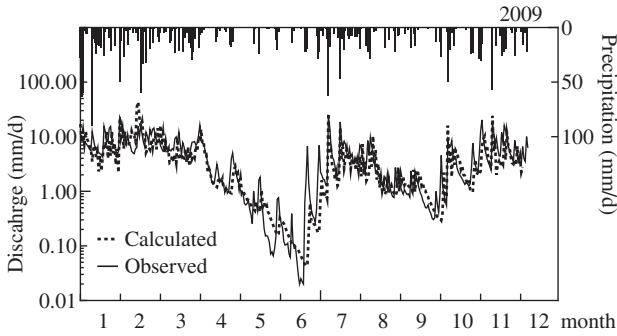
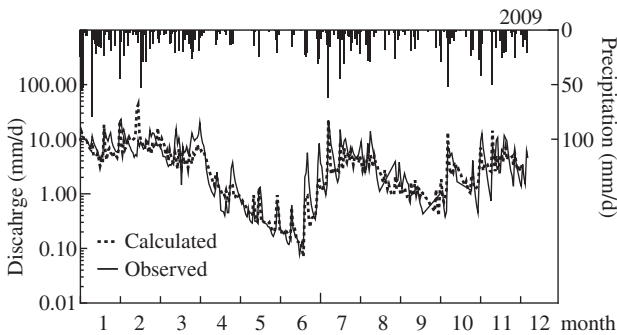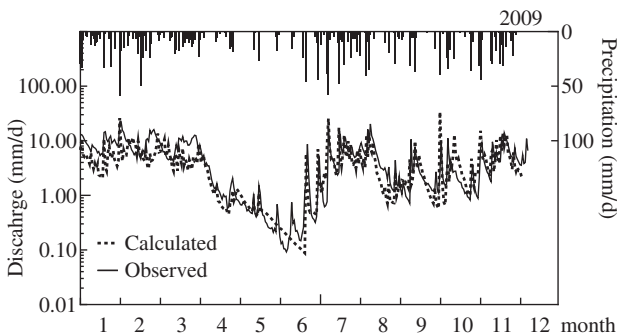**Fig. 137** Long-term observed and calculated hydrographs for cultivat-edpaddy watershed (2009).

Fig. 138 Long-term observed and calculated hydrographs for abandoned-paddy watershed (2009).

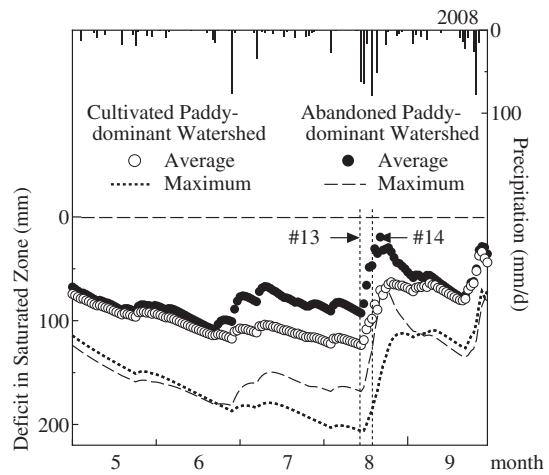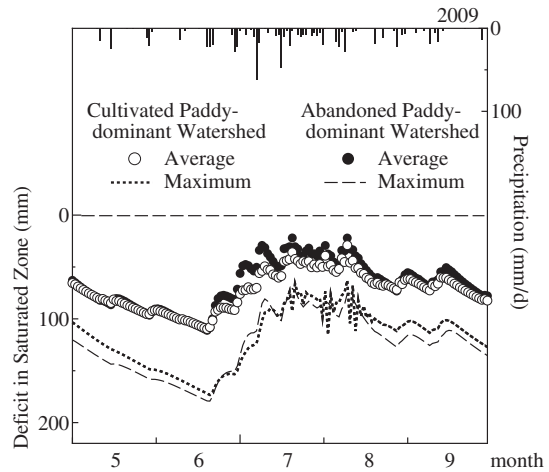**Fig. 139** Long-term observed and calculated hydrographs for forest watershed (2009).

Fig. 140 Time-series of storage deficit in saturated zone for the cultivated- and abandoned-paddy watersheds in 2008. 'Average' in the figure represents the average values of grid cells in which paddy fields exist.

Fig. 141 Time-series of storage deficit in saturated zone for the cultivated- and abandoned-paddy watersheds in 2009. 'Average' in the figure represents the average values of grid cells in which paddy fields exist.

tively. Thus, the model was able to represent the increasing trend of the peak runoff coefficient in APW for event no. 14.

The antecedent soil moisture conditions, as well as the topography and rainfall intensity, are important in governing the short term runoff processes. However, the effects of antecedent soil moisture conditions were discussed on short-term runoff characteristics observed in these two events, while neglecting the differences in topography (**Fig. 117**) and rainfall intensity. The D_s values averaged over grid cells with paddy fields were 123.5 mm in CPW and 83.6 mm in APW at the beginning of rainfall no. 13 (#13 in **Fig. 140**), whereas those at the beginning of rainfall no. 14 were 98.1 and 46.9 mm, respectively, or about 25-30 mm less.

The total precipitation in rainfall no. 13 (CPW, 64.5

mm; APW, 70.0 mm) was smaller than the estimated D_s (CPW, 123.5 mm; APW, 83.6 mm), whereas the precipitation in no. 14 (CPW, 79.5 mm; APW, 65.5 mm) was smaller than the estimated D_s in CPW (98.1 mm) but larger than that in APW (46.9 mm). The calculated saturated excess overland flow in APW was larger than that in CPW, indicating that the water table near the abandoned paddies affected the short-term runoff characteristics in the watershed. The primary reason for the difference in D_s is that only vertical flow in unsaturated zones was assumed in the model. Onishi et al. (2003) noted that by incorporating detailed topography of paddies and slopes in a small hill slope with terraced paddies, water infiltrated into the paddy surface could be modelled to emerge at the bottom of the slope. This implies the necessity of performing detailed water flow analysis of the unsaturated zone for watersheds with
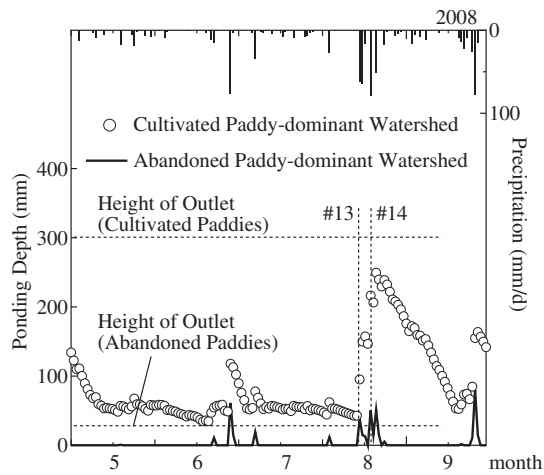
Fig. 142 Time-series of ponding depth for the cultivated- and abandoned-paddy watersheds (2008).
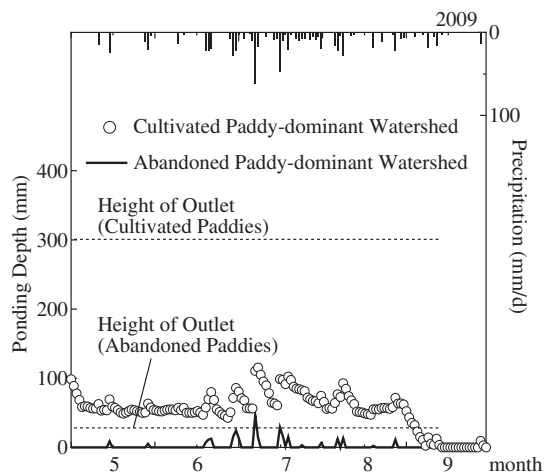
Fig. 143 Time-series of ponding depth for the cultivated- and abandoned-paddy watersheds (2009).

complex topography.

The proposed model is able to represent the mosaic of land uses in watersheds. Therefore, how flow regimes will be altered according to changes in land use and paddy cultivation conditions can be projected. In addition, the calibrated parameters can be transferred to watersheds of equivalent geological and topographical formations, which enables us to extend this watershed-scale evaluation to the regional scale.

6.6 Summary

In this section, the integrated model's ability was investigated to reproduce differences in runoff characteristics among watersheds. To assess the interaction between hydrological characteristics and paddy conditions, three small experimental watersheds were chosen, each of which was characterized by cultivated paddies, abandoned paddies, or forest.

1) The analysis revealed that the runoff ratios of APW were significantly higher than those of CPW under wet conditions, whereas no significant differences were observed between the watersheds under dry conditions. These results indicate that abandonment of paddies leads to larger peak discharges, suggesting that the presence of abandoned paddies increases the flood risk in a watershed.

2) The model parameters for hydrogeological properties were calibrated using the long-term rainfall and runoff data observed in FW and applied the parameters to APW and CPW.

   The results of the calculations in both watersheds were acceptable in terms of long-term runoff, confirming the parameter transferability of the proposed model.

3) Next, a submodel representing land surface process in abandoned paddies was developed and incorporated into the catchment-scale water circulation model, which was then applied to the three experimental watersheds. Before the calculation of the short-term runoff events, long-term calculations at 1-d intervals were performed to estimate the initial conditions or wetness in each experimental watershed.

   Then short-term runoff calculations were performed at 10- min intervals using the extracted state variables for CPW and APW.

4) The discharge calculations revealed higher flow peaks for APW than for CPW in wet conditions, whereas the flow peaks were equivalent in dry conditions. These results were in accordance with the observed runoff characteristics. Comparison of the initial conditions between the watersheds revealed that the storage Volumes of the saturated zones were greater in the abandoned paddies than in the cultivated paddies, suggesting that the water table was higher under the abandoned paddies. The modelling experiments showed that differences in groundwater storage may affect the short-term runoff characteristics of small watersheds

Appendix 6: Observed discharges and calculated discharges in the rainfall events listed in **Table 5**
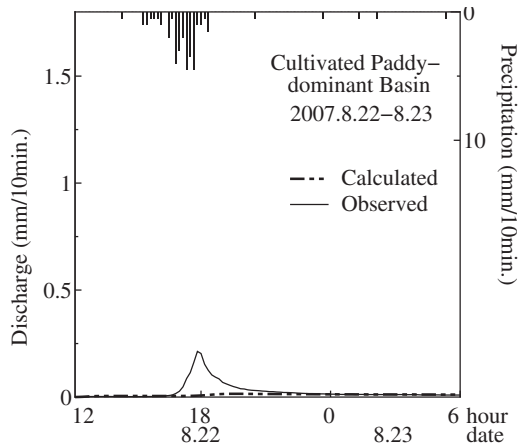
Fig. 144 Calculated discharge and observed precipitation in rainfall no. 1 (CPW).
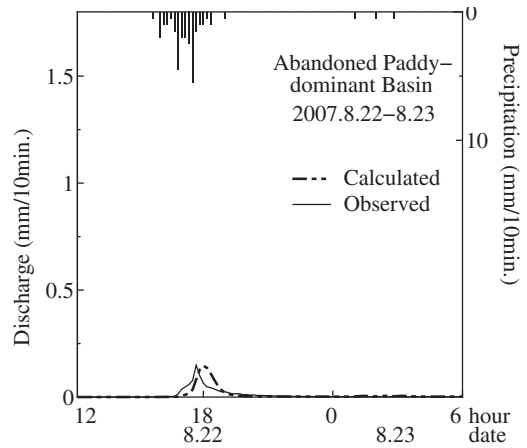
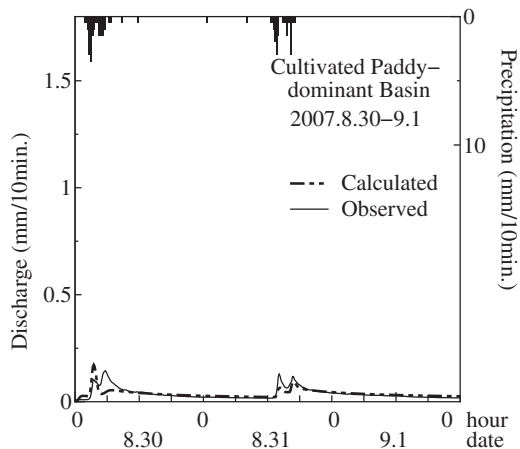**Fig. 145** Calculated discharge and observed precipitation in rainfall no. 1 (APW).
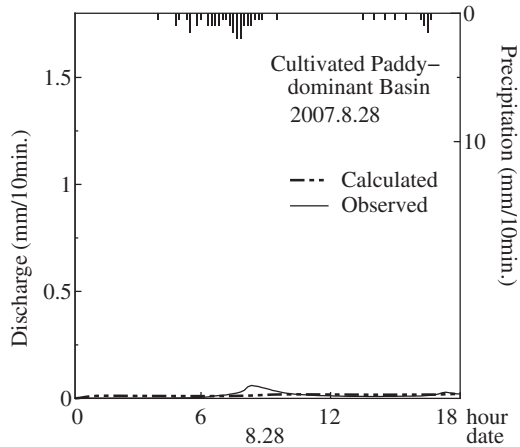
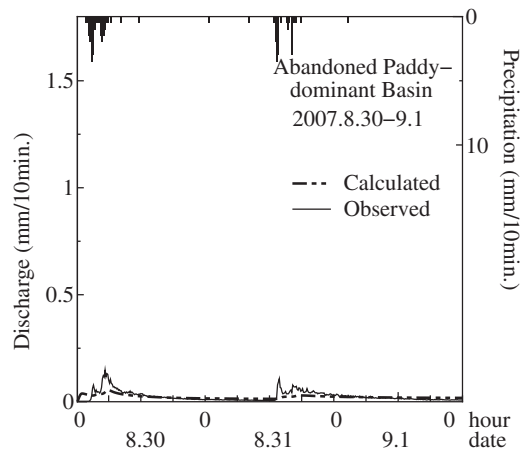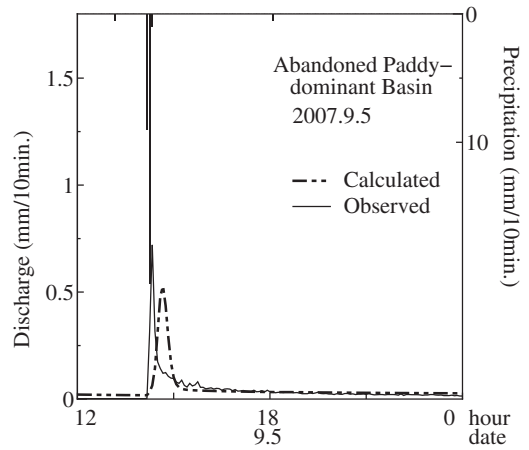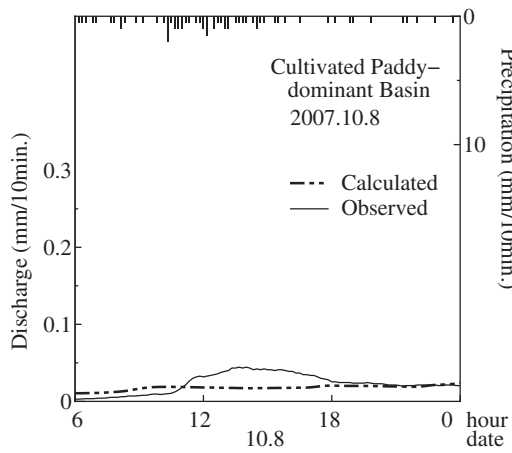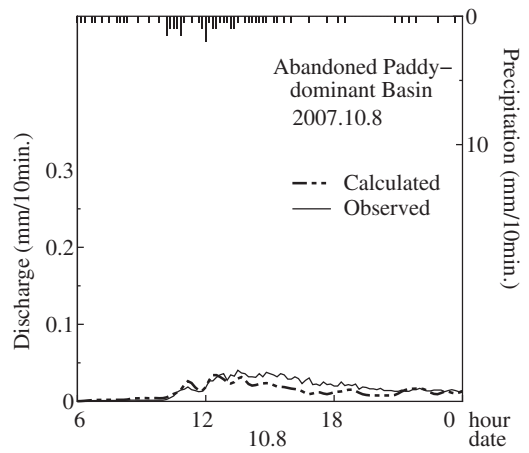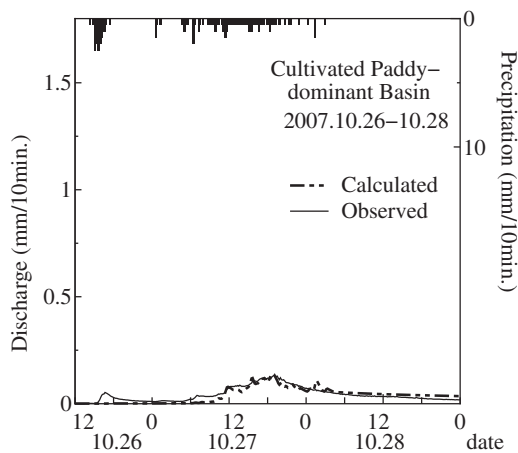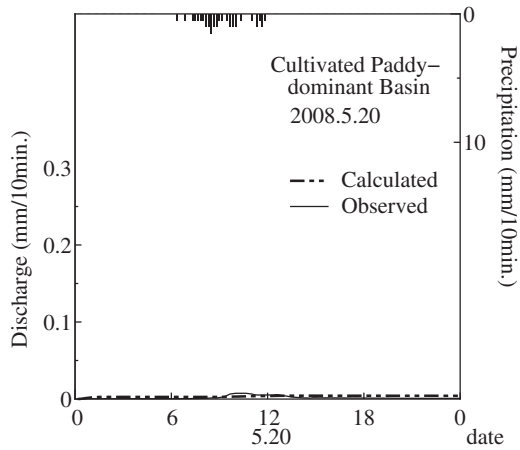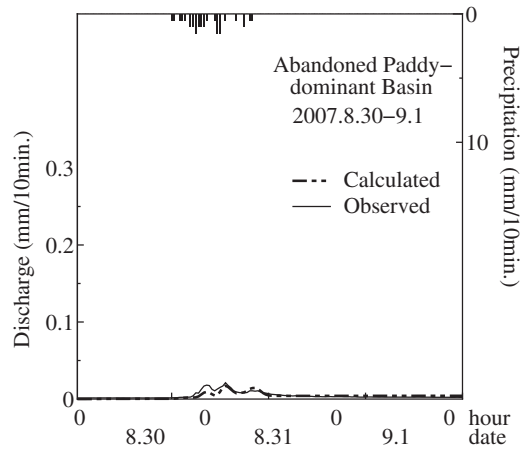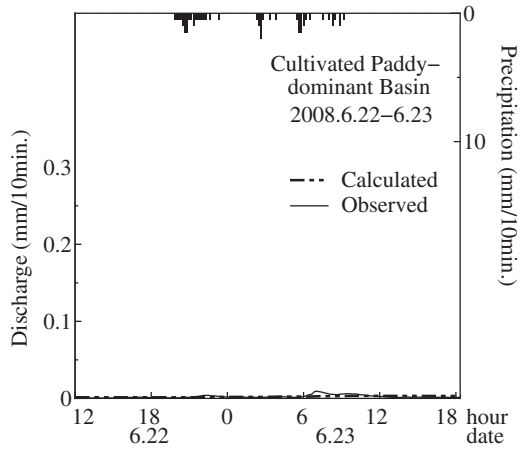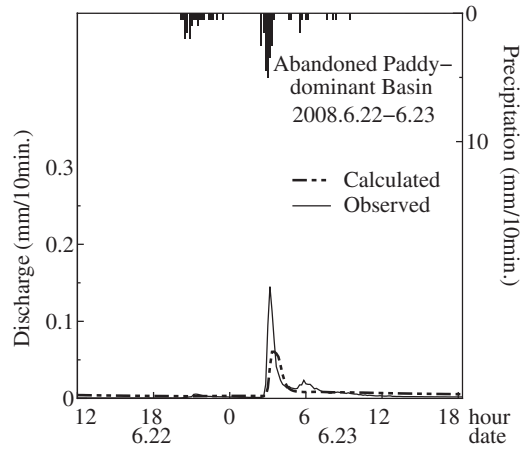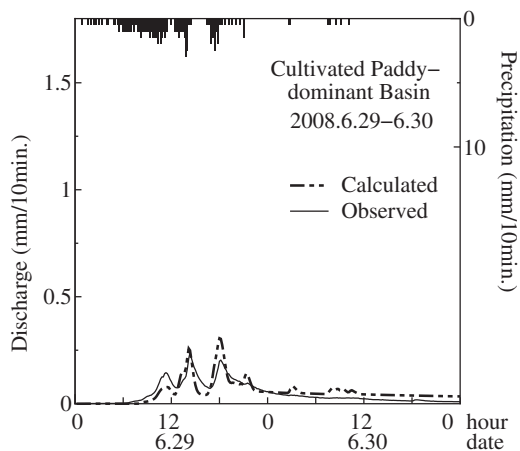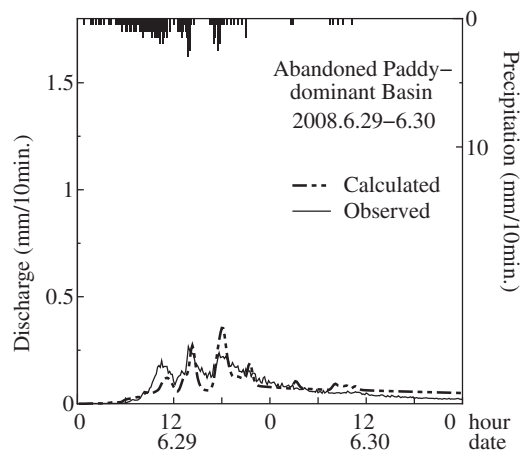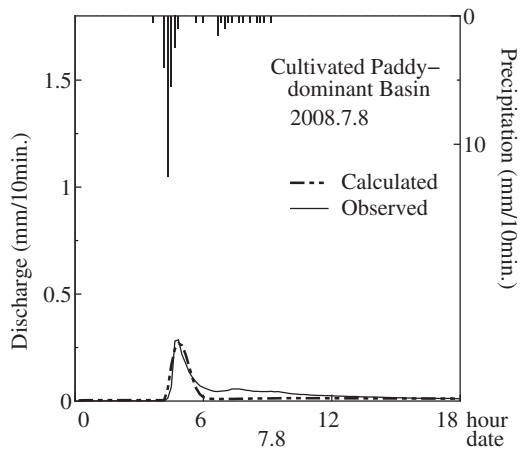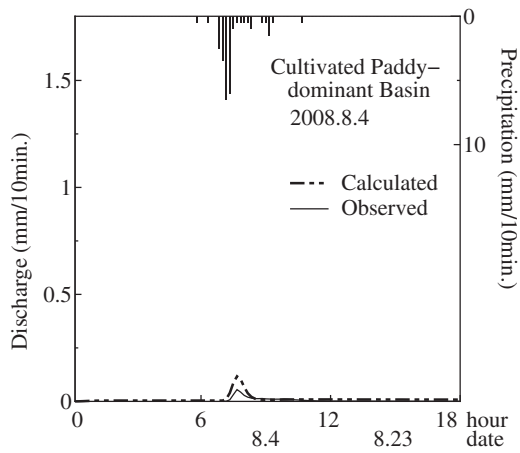**Fig. 146** Calculated discharge and observed precipitation in rainfall no. 2 (CPW).
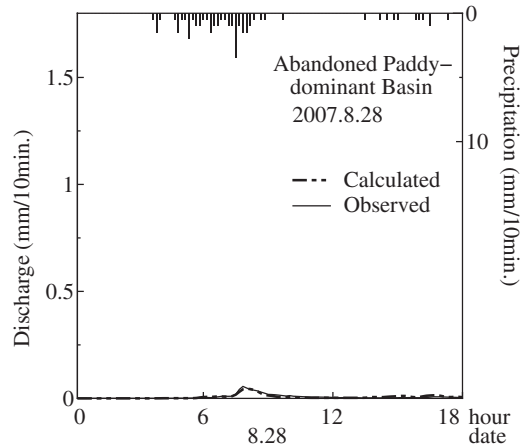
Fig. 147 Calculated discharge and observed precipitation in rainfall no. 2 (APW).
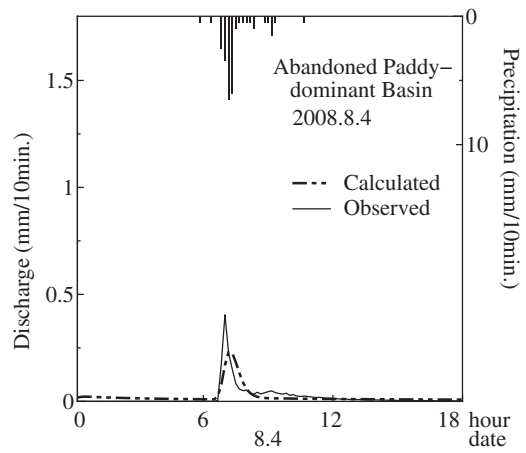

Fig. 148 Calculated discharge and observed precipitation in rainfall no. 3 (CPW).

Fig. 149 Calculated discharge and observed precipitation in rainfall no. 3 (APW).

Fig. 150 Calculated discharge and observed precipitation in rainfall no. 4 (APW).

Fig. 151 Calculated discharge and observed precipitation in rainfall no. 5 (CPW).

Fig. 152 Calculated discharge and observed precipitation in rainfall no. 5 (APW).
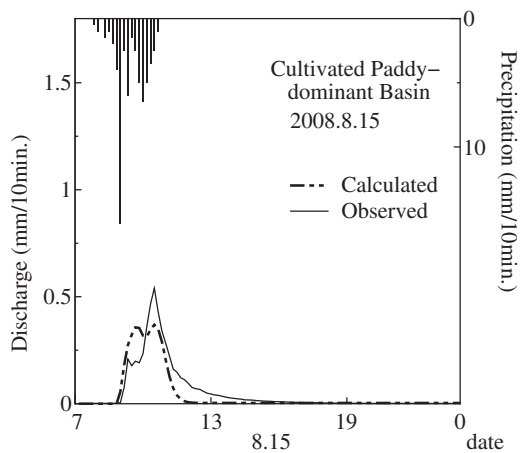

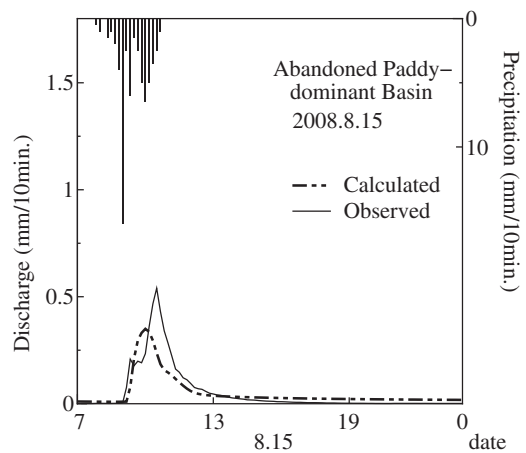**Fig. 153** Calculated discharge and observed precipitation in rainfall no. 6 (CPW).

Fig. 154 Calculated discharge and observed precipitation in rainfall no. 7 (CPW).

Fig. 155 Calculated discharge and observed precipitation in rainfall no. 7 (APW).

Fig. 156 Calculated discharge and observed precipitation in rainfall no. 8 (CPW).

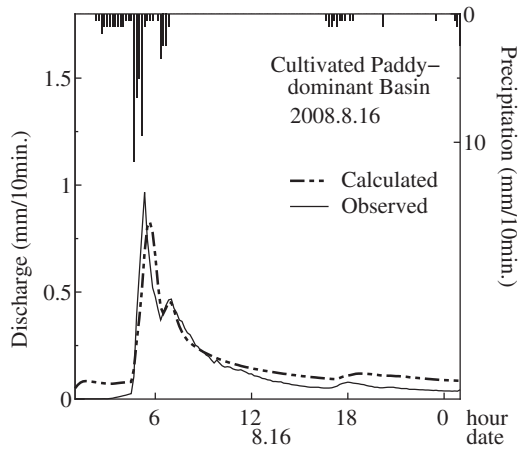**Fig. 157** Calculated discharge and observed precipitation in rainfall no. 8 (APW).

Fig. 158 Calculated discharge and observed precipitation in rainfall no. 9 (CPW).

Fig. 159 Calculated discharge and observed precipitation in rainfall no. 9 (APW).

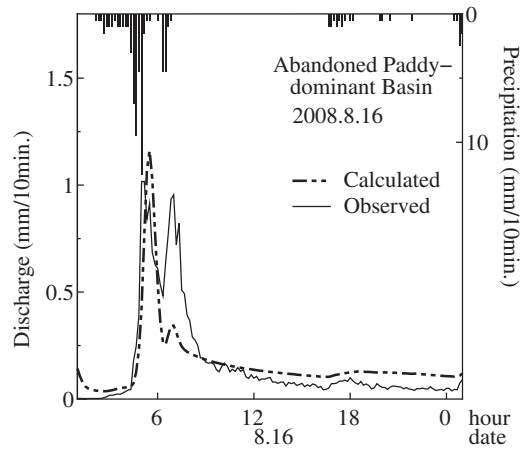**Fig. 160** Calculated discharge and observed precipitation in rainfall no. 10 (CPW).

Fig. 161 Calculated discharge and observed precipitation in rainfall no. 11 (CPW).

Fig. 162 Calculated discharge and observed precipitation in rainfall no. 11 (APW).
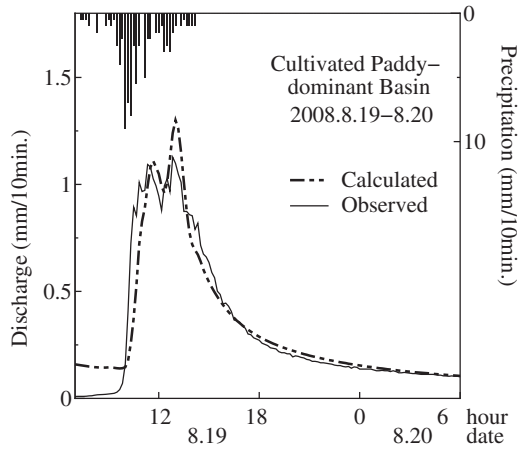

Fig. 163 Calculated discharge and observed precipitation in rainfall no. 12 (CPW).
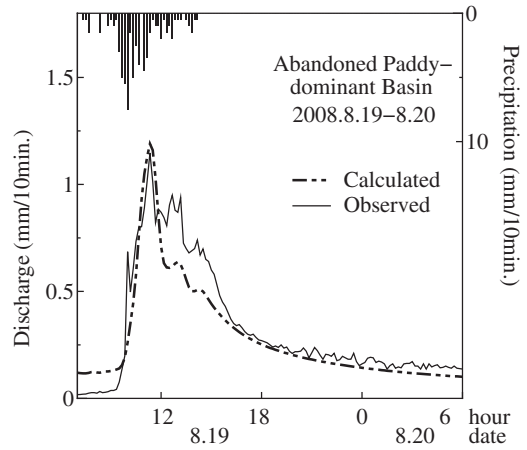

Fig. 164 Calculated discharge and observed precipitation in rainfall no. 12 (APW).

Fig. 165 Calculated discharge and observed precipitation in rainfall no. 13 (CPW).

Fig. 166 Calculated discharge and observed precipitation in rainfall no. 13 (APW).

Fig. 167 Calculated discharge and observed precipitation in rainfall no. 14 (CPW).

Fig. 168 Calculated discharge and observed precipitation in rainfall no. 14 (APW).
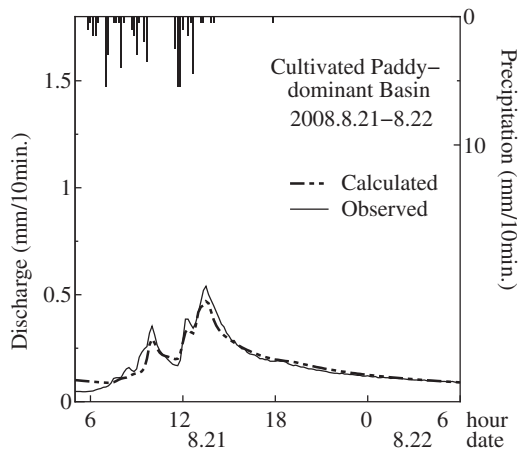

Fig. 169 Calculated discharge and observed precipitation in rainfall no. 15 (CPW).
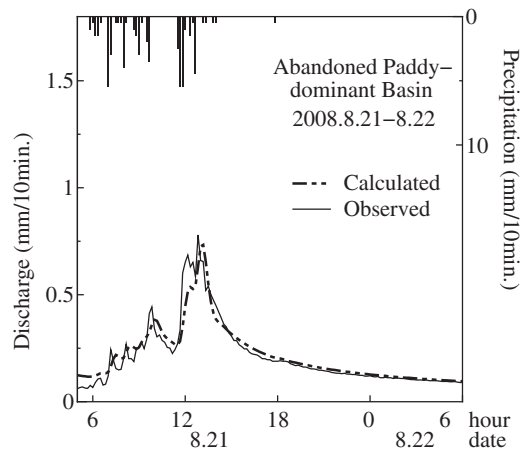

Fig. 170 Calculated discharge and observed precipitation in rainfall no. 15 (APW).
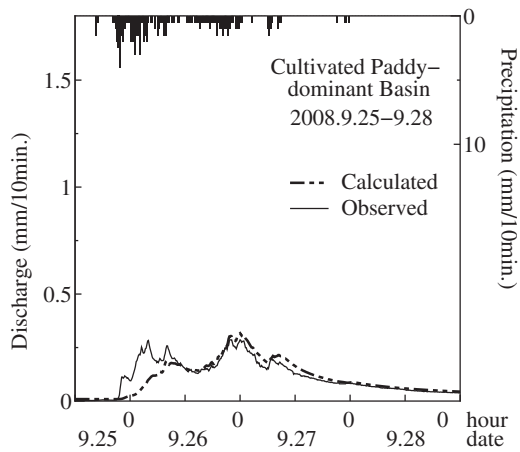
Fig. 171 Calculated discharge and observed precipitation in rainfall no. 16 (CPW).
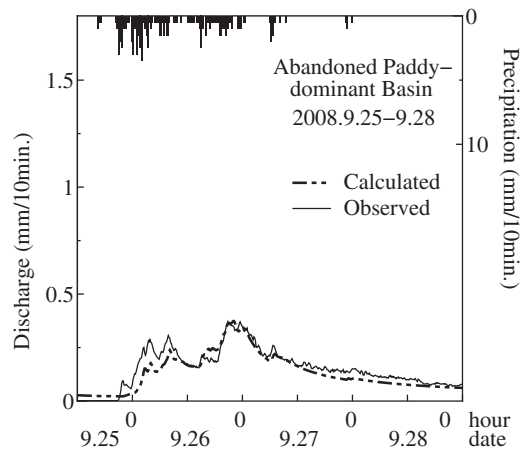
Fig. 172 Calculated discharge and observed precipitation in rainfall no. 16 (APW).

Fig. 173 Calculated discharge and observed precipitation in rainfall no. 17 (CPW).

Fig. 174 Calculated discharge and observed precipitation in rainfall no. 17 (APW).

Fig. 175 Calculated discharge and observed precipitation in rainfall no. 18 (CPW).

Fig. 176 Calculated discharge and observed precipitation in rainfall no. 18 (APW).

Fig. 177 Calculated discharge and observed precipitation in rainfall no. 19 (CPW).

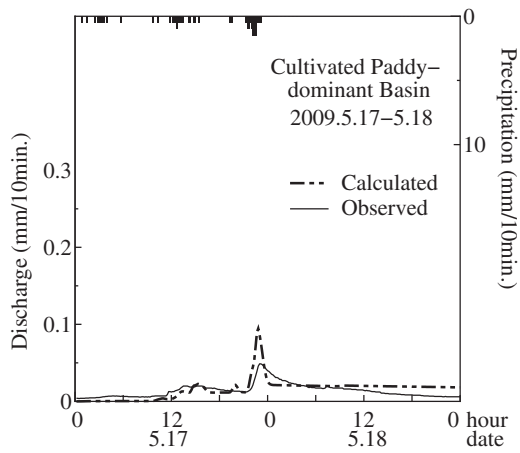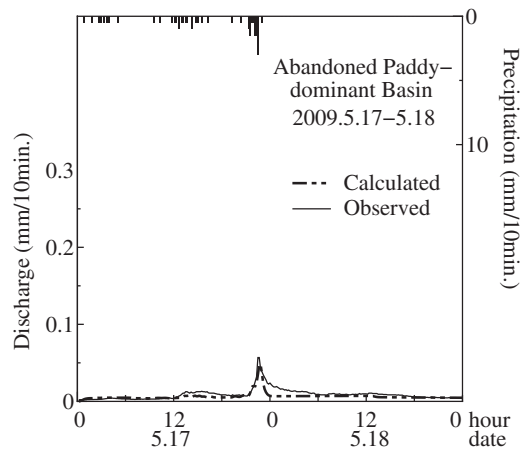**Fig. 178** Calculated discharge and observed precipitation in rainfall no. 19 (APW).

Fig. 179 Calculated discharge and observed precipitation in rainfall no. 20 (CPW).

Fig. 180 Calculated discharge and observed precipitation in rainfall no. 20 (APW).
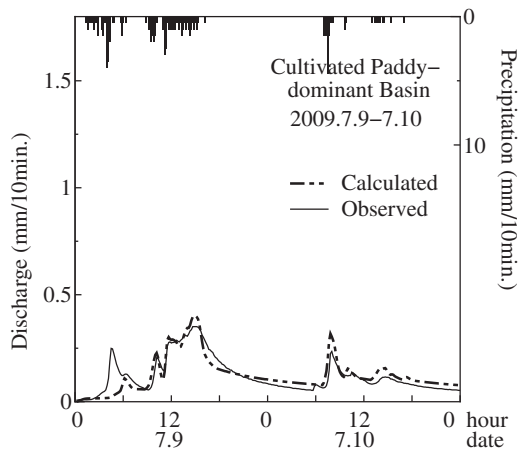
Fig. 181 Calculated discharge and observed precipitation in rainfall no. 21 (CPW).
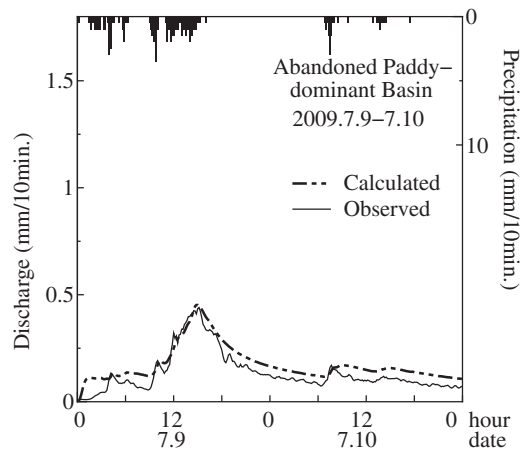
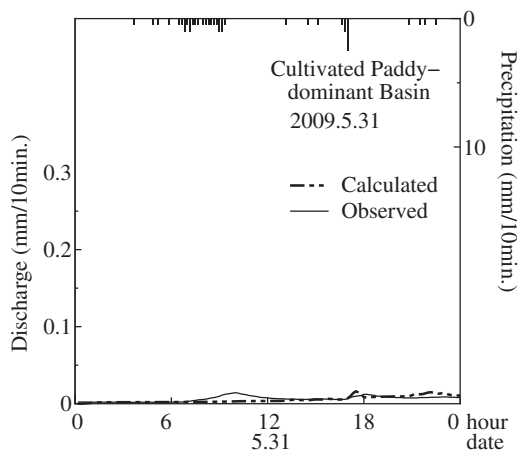**Fig. 182** Calculated discharge and observed precipitation in rainfall no. 21 (APW).
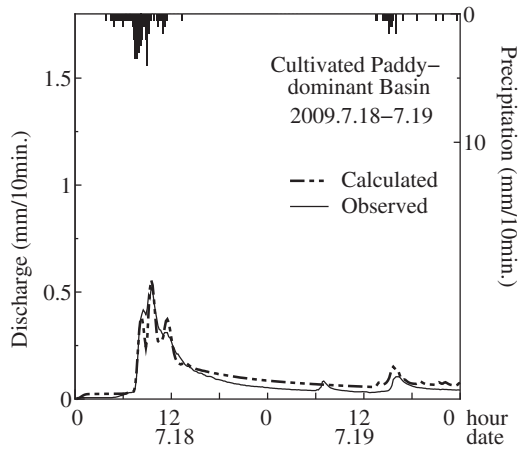
Fig. 183 Calculated discharge and observed precipitation in rainfall no. 22 (CPW).
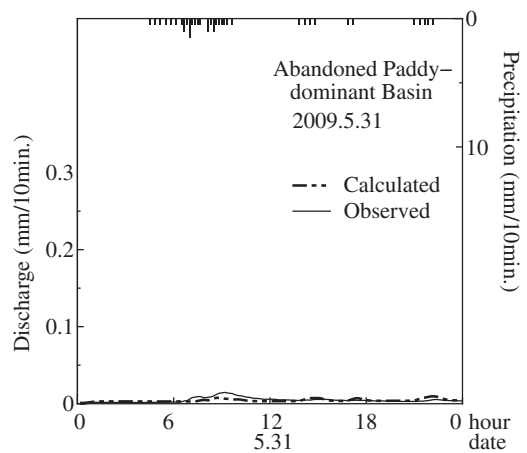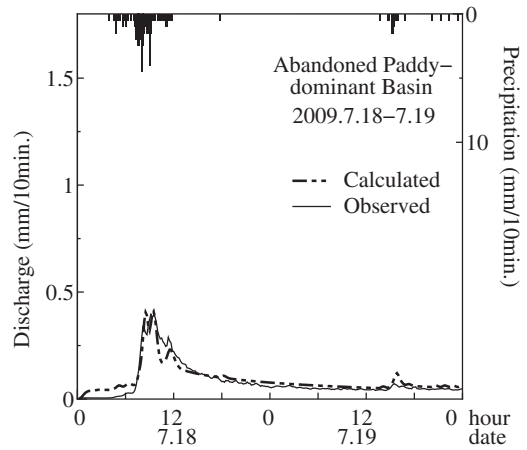
Fig. 184 Calculated discharge and observed precipitation in rainfall no. 22 (APW).
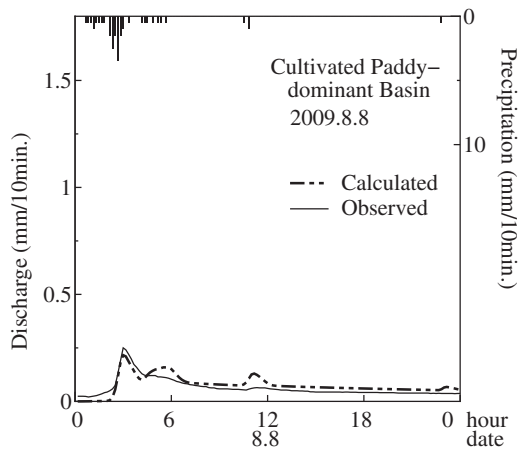
Fig. 185 Calculated discharge and observed precipitation in rainfall no. 23 (CPW).
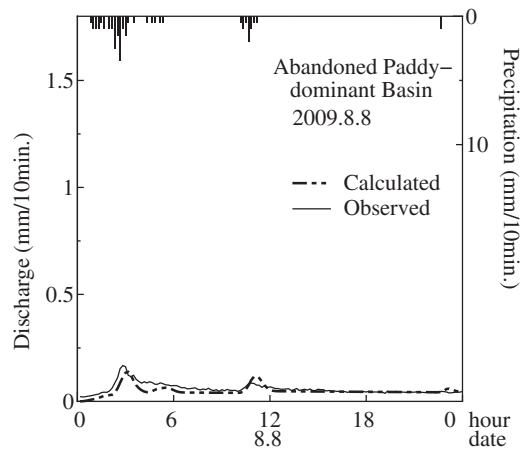
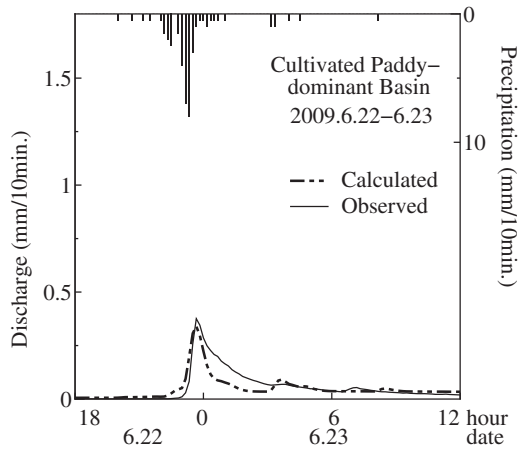**Fig. 186** Calculated discharge and observed precipitation in rainfall no. 23 (APW).

Fig. 187 Calculated discharge and observed precipitation in rainfall no. 24 (CPW).

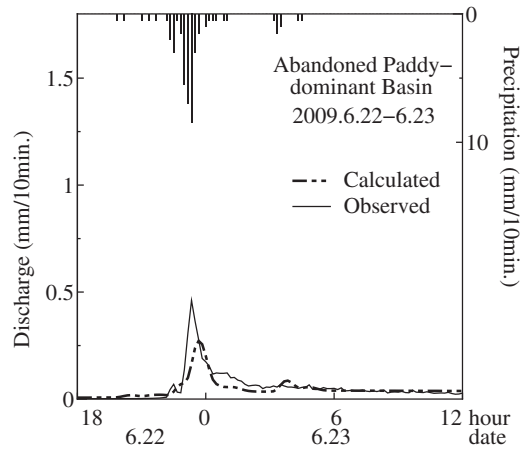**Fig. 188** Calculated discharge and observed precipitation in rainfall no. 24 (APW).

Fig. 189 Calculated discharge and observed precipitation in rainfall no. 25 (CPW).

Fig. 190 Calculated discharge and observed precipitation in rainfall no. 25 (APW).

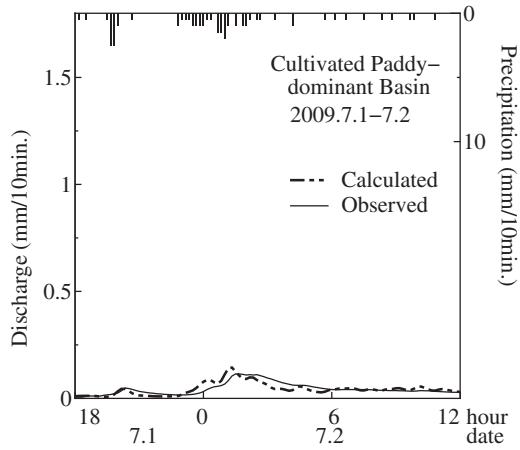**Fig. 191** Calculated discharge and observed precipitation in rainfall no. 26 (CPW).
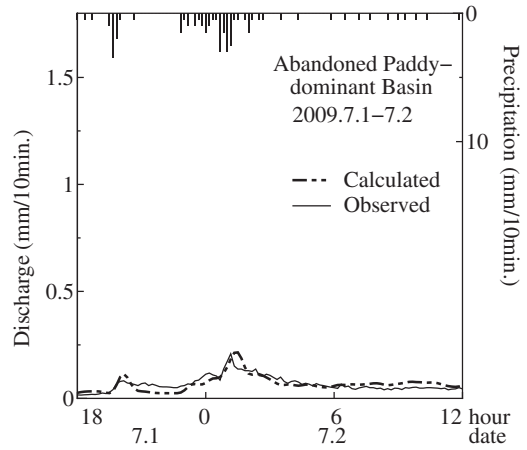
Fig. 192 Calculated discharge and observed precipitation in rainfall no. 26 (APW).
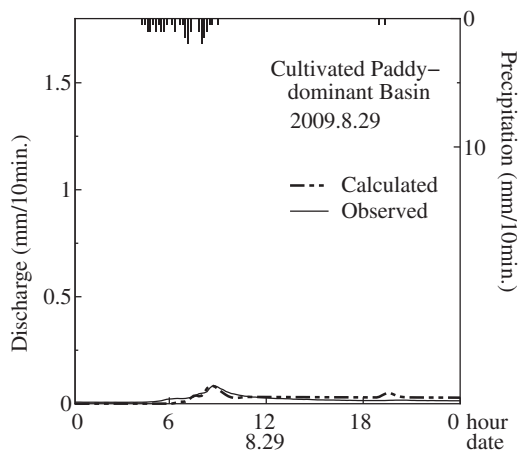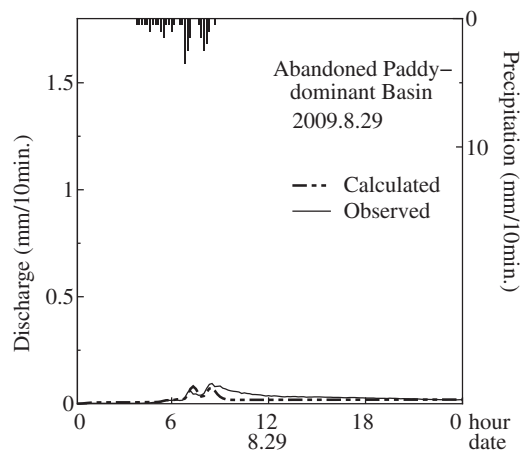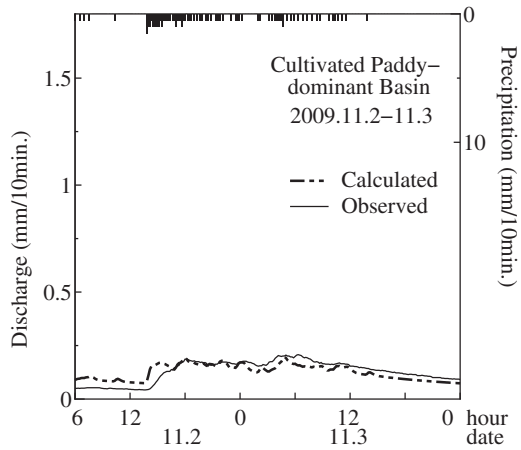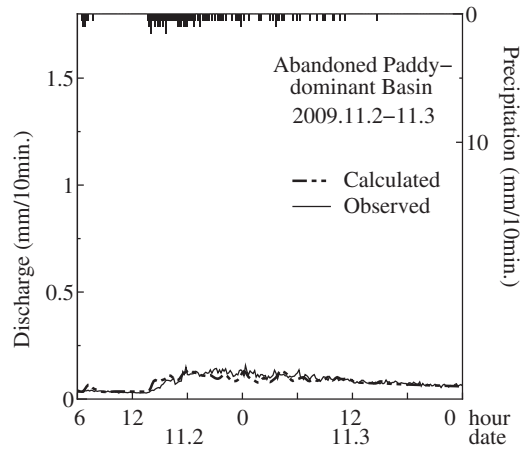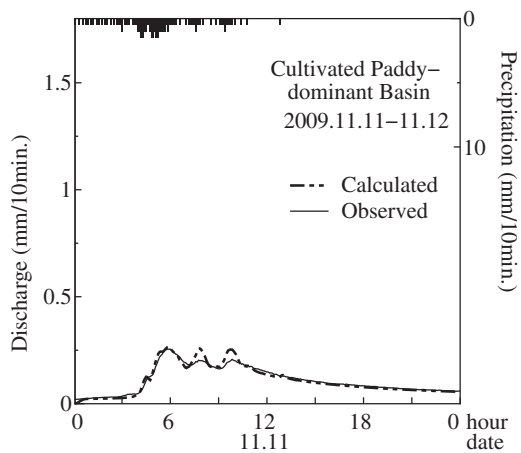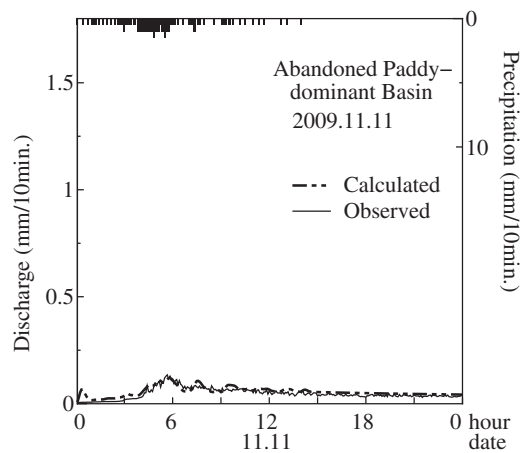
7. Conclusion

7.1 Main findings

In this thesis, the author presents an integrated model that couples catchment-scale natural hydrological cycles and human-related water cycles in irrigated paddy areas; hereafter the catchment-scale water circulation model. The main objective of model development is to assess the interaction between human-related and natural water cycles, especially in watersheds where densely irrigated paddies are dominant. In addition, to extend the applicability of the model to a broad range of hydrological conditions, several sub-models are developed for representing flood inundation and snow-melting processes. These sub-models are subsequently integrated into the catchment-scale water circulation model.

The new model consists of five modules: water allocation and management, planting pattern and area, paddy water use, actual evaporation, and runoff. The model simulates both natural and anthropogenic water flow on a grid-cell basis. In each grid cell there are three conceptual soil layers: root zone, unsaturated zone, and saturated zone storage. Each grid cell is associated with mixture of various land uses, and for each land use the model simulates the generation of surface runoff and actual evapotranspiration. The generated surface runoff is routed by using a one-dimensional kinematic wave for channel flow.

The model explicitly represents water cycles in paddy areas as well as representing natural hydrological cycles, thus enabling assessment of water management for irrigated paddies. To represent water management in paddy fields, two modules were employed from the base model, namely planting pattern and area, and paddy water use models. These sub-models simulate the spatial and temporal variation in planting areas and water use in watersheds dominated by rain-fed paddies. In contrast, a new part of the approach is the representation of water fluxes over multiple grid cells. Here, water fluxes include reservoir management for irrigation, allocation of diverted water to large irrigated paddies, and return flow from irrigated paddies to rivers. Representation of water flux over multiple grid cells is the core theme of this thesis.

The water allocation and management model is based on two major algorithms, namely, a reservoir operation scheme and a water allocation scheme. The reservoir operation scheme is used to estimate releases from the reservoir to irrigation weirs downstream. Typical water releases from a reservoir, such as releases for hydro-power generation or releases of excess water via a spillway, are calculated simply by evaluating the inflow and storage capacity of the reservoir. In contrast, irrigation releases need to consider the flow rates at diversion points downstream. In other words, the amount of water released should meet the water demand at the downstream diversion point.

The lack of precise data describing water-use facilities and channel networks inhibits the modeling of water flux over multiple grid-cells. Therefore, a recently configured GIS database of water-use facilities throughout Japan was used. The database contains specifications for each facility, as well as for irrigation channel networks and irrigation block polygons; these last two criteria have rarely been used for hydrological modeling. Instead of calculating detailed water flows with hyraulics, the model simulated water allocation according to priority orders of gridcells in each irrigated block. Thus, first the priority order were determined by assuming paddies in upper part in the irrigation block with channel have higher priority compared with those in lower part without channel. The priority order was determined by using the following attributes of each grid cell: 1) distance from weir, 2) distance from irrigation channels, and 3) elevation. Then, water was allocated on the basis of the water demand in each grid cell, following the priority order in each irrigation block. The modeled river networks were used to route the drainage from irrigated paddies.

As a case study, the catchment-scale water circulation model was applied to the Seki River Basin in Japan. The grid cell size was approximately 1km^2, and the catchment area was 1140 km^2. Three irrigated paddy areas extended along the sides of the main river; the total area of these paddies was 9200 ha. The model performance was first investigated by comparing the calculated discharges with those observed at two observation stations along the main river. One was located just downstream of the largest diversion weir, and the other was located at the outlet of the watershed. When the results from application of the water allocation schemes were incorporated, the calculated discharges during irrigation periods closely agreed with the observed data at both points. The results indicated that both of the observation points were strongly influenced by diversion and return flow processes, and that the water allocation and management model that we developed was highly capable of representing the interaction between water circulation in irrigated paddy areas and river flow systems. The results also suggested that a large portion of the diverted water was returned to the river and thus could contribute to stable flows for downstream water uses.

Two sub-models were developed and integrated into the main model to extend its applicability to a broad range of hydrological conditions. First, Section 4 presented a grid-cell-based snowfall/snowmelt model in which daily snow accumulation and snowmelt are calculated by using a simplified energy balance. Satellite images of snow-capped areas were used to estimate the spatial distribution of model parameters in regions where the observed meteorological data were sparse.

The model was applied to the Seki River Basin, a representative snowy basin in an area with a relatively warm winter climate in Japan. Comparison of the calculated and observed snow water equivalent (SWE) revealed that the model successfully represented the spatial distributions of SWE within a range of 200 mm, except in areas where locally intensive snowfalls occurred. In addition, the discharges during snow-melt periods, as calculated by using the catchment-scale water circulation model, represented flow peaks and flow regressions with high accuracy.

In Section 5, an inundation process model was also developed and integrated into the catchment-scale water circulation model. To assess flood hazard, a simple model that assumes that the inundated area is a reservoir was employed. In other words, no active water movement is assumed in the inundated area because the whole area is flat. In this model, the inundation volume is calculated by using a continuity equation with the relation between inundation depth and volume for the area: the excess rate of surface flow above the maximum conveyance capacity of the rivers is input by using a distributed water circulation model. To apply the inundation model, the high-resolution digital elevation model ASTER GDEM was used to extract detailed topographic features. High-resolution raster digital elevation models, which are becoming available at global scale, provide useful information on detailed topographical features within the grid cells of distributed hydrological models.

The model was applied to the Xebanfai River in the Laos PDR and performed daily calculations for 2004 through 2008. The Xebanfai River, a tributary of the Mekong River, drains an area of 10,330 km^2. Paddy fields, which account for 23% of the total catchment area, are found predominantly in the lower part of the watershed. Thus, prolonged flooding causes damage to extensive paddy areas. Incorporation of the inundation process model, markedly improved the performance of the catchment-scale water circulation model in terms of calculated discharges, including the timing of peak discharges. In addition, the model was rigorously validated by using the maximum area inundated in 2008, as determined from ALOS/PALSAR images. The comparison confirmed that the large-scale inundation processes in the lower reaches of the watershed were precisely represented by the model; hence, the model enables the agricultural damage caused by flooding to be evaluated.

The integrated model's ability to reproduce differences in runoff characteristics among watersheds was investigated. To assess the interaction between hydrological characteristics and paddy conditions, three experimental watersheds were set, each of which is dominated by either cultivated paddies, or abandoned paddies, or forest: namely cultivated-paddy-dominant watershed (CPW), abandoned-paddy-dominant watershed (APW),

and forest watershed. Each of the watersheds was approximately 1 km^2 in area. Rainfall and discharge were observed at 10-min intervals in each watershed. The short-term rainfall-runoff characteristics were analyzed in the case of rainfall events exceeding a daily precipitation of 20 mm and a rainfall intensity of 5 mm/h. The analysis revealed that the runoff ratios of APW were significantly higher than those of CPW under wet conditions, whereas no significant difference between the watersheds was observed under dry conditions. These results indicate that abandonment of paddies leads to larger peak discharges, suggesting that the presence of abandoned paddies increase the flood risk in a watershed.

Next, a sub-model representing land-surface process in abandoned paddies was developed and incorporated into the catchment-scale water circulation model. The model was applied to the three experimental watersheds. Before the calculation of the short-term runoff events, long-term calculations at 1-day intervals were performed to estimate the initial conditions, or wetness, in each experimental watershed. Then short-term runoff calculations at 10-min intervals were performed using the extracted state variables for CPW and APW. The discharge calculations revealed higher flow peaks for APW than for CPW in wet conditions, whereas the flow peaks were equivalent in dry conditions. These results were in accordance with the observed runoff characteristics. Comparison of the initial conditions between the watersheds revealed that the storage Volumes of the saturated zones were higher in the abandoned paddies than in the cultivated paddies, suggesting that the water table was higher under the abandoned paddies. The model experiments showed that differences in groundwater storage may affect the short-term runoff characteristics of small watersheds.

7.2 Outlook

In this thesis, the author presents a novel approach for assessing the interaction between natural and anthropogenic water cycles in irrigated-paddy-dominant watersheds. In addition to assessing this interaction, the proposed model is able to reproduce the changes in water circulation in watersheds by accounting for differences in paddy field management schemes. The concepts in the model should contribute to ongoing discussions on how to incorporate anthropogenic impacts into distributed hydrological models.

There are two potential beneficiaries of this model: the climate change impact-assessment community and managers of water resources in paddy-dominant watersheds. A number of studies have examined the impacts of climate change on water resources. However, the effects of anthropogenic water cycles in paddy-dominant watersheds have not yet been examined explicitly, and

thus the impact of climate change on paddy water-use systems is not fully understood. The proposed model calculates both natural and anthropogenic water cycles in watersheds. It thus provides not only stream flow changes, but also the potential effects of climate change on reservoir storages and the amounts of water diverted for paddy irrigation.

Although this model explicitly accounts for the water management associated with irrigation for rice paddies, the model simulates 'business as usual' water management. In other words, the model has limited abilities to predict the response of irrigation systems to extreme flood or drought, or to estimate threshold level to which watershed systems can withstand. Since the levels differ according to the natural hydrological characteristics and system properties, empirical studies to investigate (clarify) the threshold behaviors of the system are important for the model improvement.

Also, the model has the potential to contribute to water resources management, especially in watersheds undergoing rapid societal change. The expected societal changes in paddydominant watersheds in Japan will lead not only to an increase in the number of abandoned paddies, but also to increases in the number of crop varieties used and the length of irrigation periods, or increases in water demand due to changes in field water management. Moreover, in developing countries in the Asian Monsoon region, the area under irrigation and the number of reservoirs being developed are increasing at a tremendous rate. This model should be highly useful in the planning for optimum management of such watersheds.

Assessing the potential impacts of changes in the natural and social environments of watersheds on water resources is one of the main areas of study to which hydrological models can contribute. If such impacts on water resources are found to be negative, then it will be important to propose effective countermeasures. The model presented here, which accounts for multiple water uses in an integrated manner, is suitable for addressing these issues and for optimizing water-use regulations for whole watersheds and water sharing among water-use sectors.

Reference
Abbott M. B., Bathurst J. C., Cunge J. A., O'Connell P.E. and Rasmussen J. (1986): An introduction to the european hydrological system-Systeme Hydrologique Europeen,"SHE", 1: History and philosophy of a physically-based, distributed modelling system. *Journal of hydrology*, **87** (1), 45-59.

Adachi K., Tsuda Y., Bizen N. and Tamura H. (1994): Agriculture and rural environments in heavy snow and land slide are in Hokuriku region. *Journal of the Agricultural Engineering Society, Japan*, **62** (6), 515-520 (in Japanese).

Adachi K., Yoshida S., Masumoto T. and Itoh K. (1997): Method of measuring macropore volume contributed to underdrain discharge in clayey multi-purpose paddy field. *Trans. of JSIDRE*, **65** (6), 847-855 (in Japanese with English abstract).

Alcántara-Ayala, I. (2002) : Geomorphology, natural hazards, vulnerability and prevention of natural disasters in developing countries, *Geomorphology*, **47** (2), 107-124.

Allen, G.R., Pereira, L.S., Raes, D. and Smith, M. (1998) : Crop evapotranspiration -Guidelines for computing crop water requirements-, *FAO Irrigation and drainage paper*, **56**, p.15.

Bell V. A. and Moore R. J. (1998): A grid-based distributed flood forecasting model for use with weather radar data: Part 1. formulation. *Hydrology and Earth System Sciences*, **2**, 265-281.

Bell V. A., Kay A. L., Jones R. G., Moore R. J. and Reynard N. S. (2009): Use of soil data in a grid-based hydrological model to estimate spatial variation in changing flood risk across the UK. *Journal of Hydrology*, **377**, (3), 335-350.

Beven K. J. and Kirkby M. J. (1979): A physically based, variable contributing area model of basin hydrology, *Hydrological Sciences Journal Bulletin*, **24** (1), 43-69.

Beven, K. and Wood, E.F. (1983) : Catchment geomorphology and the dynamics of runoff contributing area, *Journal of Hydrology*, **65**, 139-158.

Beven K. J. (2011): Rainfall-runoff modelling: the primer, John Wiley & Sons, Ltd.

Boorman D. B., Hollis J. M. and Lilly A. (1995): Hydrology of soil types: a hydrologically-based classification of the soils of United Kingdom. *Institute of Hydrology*.

Calver A. and Wood W. L. (1995): The institute of hydrology distributed model. In: Singh V. P. (Eds.), *Computer Models of Watershed Hydrology*, chapter 17. 596-626. Water Resources Publications.

Chiba K., Koga K. and Baba H. (1997): Soil physical properties of uncultivated paddy fields located in semi-wet sloping land and the simulation of their response to heavy rain. *Trans. of JSIDRE*, **65** (4), 507-516 (in Japanese with English abstract).

Chow V. T.,Maidment D. R. and Mays L.W. (1988): Applied hydrology, 572 pp. Editions McGraw-Hill, New York, 1988.

Duan, Q.Y., Sorooshian, S. and Gupta, H.V. (1992) : Effective and efficient global optimization for conceptual rainfall-runoff models, *Water Resou. Res.*, **28** (4), 1015-1031.

Freeze R. A. and Harlan R. L. (1969): Blueprint for a physically based digitally-simulated hydrologic response model. *Journal of Hydrology*, **9** (3), 237-258.

Fujihara, Y., Tanaka, K.,Watanabe, T., Nagano, T. and Kojiri, T. (2008) : Assessing the impacts of climate change on the water resources of the Seyhan River Basin in Turkey: Use of dynamically downscaled data for hydrologic simulations, *Journal of Hydrology*, **353**, 33-48.

Green, W.H. and Ampt, G.A. (1911) : Studiese on Soil Physics -Part 1. The flow of air and water through soils, *Journal of Agric. Sci.*, **4**, 1-24.

Goto A. (1983): Long-term runoff analysis by a mesh-type simulation model. PhD thesis, The University of Tokyo (in Japanese with English abstract).

Hai, P.T.,Masumoto, T. and Shimizu, K. (2008) : Development of a twodimensional finite element model for inundation processes in the Tonle Sap and its environs, *Hydrological Processes*, **22** (9), 1329-1336.

Hanasaki, N., Kanae, S., Oki, T., Masuda, K., Motoya, K., Shirakawa, N., Shen, Y. and Tanaka, K. (2008a) : An integrated model for the assessment of global water resources - Part 1: Model description and input meteorological forcing, *Hydrol. Earth Syst. Sci.*, **12**, 1007-1025.

Hanasaki, N., Kanae, S., Oki, T., Masuda, K., Motoya, K., Shirakawa, N., Shen, Y. and Tanaka, K. (2008b) : An integrated model for the assessment of global water resources - Part 2: Application and assessments, *Hydrol. Earth Syst. Sci.*, **12**, 1027-1037.

Hayase Y. and Kadoya M. (1977): Numerical method for flood routing contained with junctions-Runoff analysis in low-lying drainage basin composed mainly of paddy field (II). *Trans. of JSIDRE*, 37-44 (in Japanese with English abstract).

Hayase Y. (1994): Evaluation of paddy field's function for flood control and a proposal of their enhancing project. *Journal of the Agricultural Engineering Society, Japan*, **62** (10), 1-6 (in Japanese with English abstract).

Horikawa N., Kudo R., Yoshida T. and Masumoto T. (2011): Development of a reservoir simulation model for evaluation of water resources management. *Applied Hydrology*, **23**, 58-66 (in Japanese with English abstract).

Inoue S. and Yokoyama K. (1998): Estimation of snow fall, maximum snow depth and snow cover condition in Japan under global climate change. *Journal of the Japanese Society of Snow and Ice*, **60** (5), 367-378. (in Japanese with Engslish abstract)

Inoue S., Yokoyama K., Ohno H. and Kawashima S. (2001): Estimation of snowfall, maximum snow depth and snow-cover condition in Japan under the global climate change (Follow-up) - Estimating water equivalents of snowfall in major Japanese catchments. *Journal of the Japanese Society of Snow and Ice*, **63** (6), 367-378. (in Japanese with Engslish abstract)

Ishizuka M. and Egusa N. (2008): Runoff analysis using distributed hydrological model with irrigation water use model in the Kinokawa river. *Proceedings of Hydraulic Engineering*, **52**, 391-396 (in Japanese with English abstract).

Kato K. and Yamazaki F. (2010): Detection of flooded areas using ALOS/PALSAR images for the 2008 Iwate-Miyagi inland earthquake. *Journal of Japan Association for Earthquake Engineering*, **10** (3) ,1-11 (in Japanese with English abstract).

Kadoya M. and Fukushima A. (1976): Concentration time of flood in small or medium river basin. *Disaster Prevention Research Institute Annuals*, **19**, 143-152.

Kazama S. and Sawamoto M. (1994): Estimation of snow volume in Tohoku district by using satellite data. *Proceedings of Hydraulic Engineering*, **38**, 102-112 (in Japanese with English abstract).

Koga K., Chiba K. and Baba H. (1997): Evaluation of one-plot intake rate of uncultivated paddy field by the observation of ponding process. *Trans. of JSIDRE*, **65** (1), 103-109 (in Japanese with English abstract).

Koike T., Takahashi Y. and Yosino S. (1985): Estimation of basin-wide snow water equivalent using snow covered area. *Proceedings of JSCE*, 159-165 (in Japanese with English abstract).

Koike T., Takahashi Y. and Yosino S. (1985): A study on modeling of snowmelt distribution. *Proceedings of JSCE*, 165-174 (in Japanese with English abstract).

Kondo, J. and Yamazaki, T. (1990) : A prediction model for snowmelt, snow surface temperature and freezing depth using a heat balance method, *J. Appl. Meteor.*, **29**, 1104-1110.

Kondo J., Nakamura T. and Yamazaki T. (1991): Estimation of the solar and downward atmospheric radiation. *TENKI*, **38** (1), 41-48.

Kudo R., Masumoto T., Yoshida T. and Horikawa N. (2012): Development of quantitative impact assessment method of

climate change on agricultural water use in irrigation-dominant basins. *Journal of the Japanese Society of Irrigation, Drainage and Rural Engineering*, **80** (1), 31-42 (in Japanese with English abstract).

Lee, J.S. (1980) : Digital Image Enhancement and Noise Filtering by Use of Local Statistics, *IEEE Transactions on Pattern Analysis and Machine Intelligence*, **PAMI-2**, 165-168.

Li, R-M., Simons, D.B. and Stevens, M.A. (1975) : Nonlinear kinematic wave approximation for water routing, *Water Resour. Res.*, **11**(2), 245-252.

Lowry, J., Hess, L. and Rosenqvist, A. (2009) : Mapping and Monitoring Wetlands Around theWorld Using ALOS PAL-SAR: The ALOS Kyoto and Carbon Initiative Wetlands Products, In: Jones, S. and Reinke, K. (Eds.), *Innovations in Remote Sensing and Photogrammetry, Lecture Notes in Geoinformation and Cartography*, 105-120, doi:10.1007/978-3-540-93962-7_9.

Lu M., Koike T. and Hayakawa N. (1998): Development of a distributed snowmelt analysis system using AMeDAS data and Digital geographic information. *Proceedings of Hydraulic Engineering*, **42**, 121-126 (in Japanese with English abstract).

Lu M., Koike T. and Ishidaira H. (2002): Development of a simulation model of water utilization based on a distributed hydrological model. *Proceedings of Hydraulic Engineering*, **46**, 277-282 (in Japanese with English abstract).

Masumoto T. and Kadoya M. (1995): Function fitting to flood runoff hydrographs and its application to the design of a retarding basin. *Trans. of JSIDRE*, 63 (2), 241-251 (in Japanese with English abstract).

Masumoto T., Takaki K., Yoshida S. and Adachi K. (1997): Effects of abandoned paddies in hilly rural areas on runoff *Trans. of JSIDRE*, **65** (3), 389-398 (in Japanese with English abstract).

Masumoto T., Nozoe M., Yoshimura A. and Matsuda S. (2003): A paddy runoff model in hilly rural areas for evaluating runoff change due to abandoned rice cultivation. *Trans. of JSIDRE*, **71** (2), 175-184 (in Japanese with English abstract).

Masumoto, T., Taniguchi, T., Horikawa, N., Yoshida, T. and Shimizu, K. (2009) : Development of a distributed water circulation model for assessing human interaction in agricultural water use, In: Taniguchi, M., Burnett, W.C., Fukushima, Y., Haigh, M. and Umezawa, Y. (Eds.), *From Headwaters to the Ocean: Hydrological Changes and Watershed Management*, Taylor and Francis, 195-201.

Mekong River Commission (2006) : *MRC Annual Flood Report 2005*, Vientiane, Lao **PDR**, p.82.

Mekong River Commission (2009) : *MRC Annual Flood Report 2008*, Vientiane, Lao **PDR**, p.84.

Milly P. C. D., Julio B., Malin F., RobertM. H., ZbigniewW. K., Dennis P. L. and Ronald J. S. (2997): Stationarity is dead. *Ground Water News & Views*, **4** (1). 6-8.

Motoya K., Yamazaki T. and Yasuda N. (2001): Evaluating the spatial and temporal distribution of snow accumulation, snowmelts and discharge in a multi basin scale: an application to the Tohoku region, Japan., *Hydrological Processes*, **15** (11), 2101-2129.

Nakagiri T., Watanabe T., Horino H. and Maruyama T. (1998): Development of a hydrological system model in the Kino river basin - Analysis of irrigation water use by a hydrological system model (I) -. *Trans. of JSIDRE*, **66** (6), 899-909 (in Japanese with English abstract).

Nakagiri T., Watanabe T., Horino H. and Maruyama T. (2000): Analysis of sufficiency and reuse of irrigation water in the Kino river basin - Analysis of irrigation water use by a basin hydrological model (II) -. *Trans. of JSIDRE*, **68** (1), 35-42 (in Japanese with English abstract).

Otsuki K., Mitsuno T. and Maruyama T. (1984): Comparison between water budget and complementary relationship estimates of catchment evapotranspiration. - Studies on the estimation of actual evapotranspiration (II). *Trans. of JSIDRE*, **112**, 17-23 (in Japanese with English abstract).

Onishi T., Horino H., Nakamura K. and Mitsuno T. (2003): Evaluation of groundwater properties in terraced paddy fields using transient unsaturated-saturated water flow analysis. *Trans. of JSIDRE*, **71** (5), 657-664 (in Japanese with English abstract).

Quinn P. F., Beven K. J., Chevallier P., and Planchon O. (1991): The prediction of hillslope flow paths for distributed hydrological modelling using digital terrain models. *Hydrological Processes*, **5** (1), 59-79.

Rost, S., Gerten, D., Bondeau, A., Lucht, W., Rohwer, J. and Schaphoff, S. (2008) : Agricultural green and blue water consumption and its influence on the global water system, *Water Resour. Res.*, **44**, W09405, doi:10.1029/2007WR006331.

Sanders, B.F. (2007) : Evaluation of on-line DEMs for flood inundation modeling, *Advances in Water Resources*, **30** (8), 1831-1843.

Satoh M., Sakata H., Tuan D. D. and Fujiki T. (1998): Runoff characteristics of return flow from a paddy field area. *Trans. of JSIDRE*, **66** (6), 985-991 (in Japanese with English abstract).

Shiraishi H., Oonish R. and Ito Y. (1976): Analysis of water balance in the Iwaki basin - Control of water resources and estimation of water balance-. *Bull. Nat. Res. Inst. Agric, Eng. Japan*, 49-116 (in Japanese with English abstract).

Sugaya H. (1990): Micrometeorological studies on the snowpack evolution in the Hokuriku region: Measurements and modeling. *Bull. Hokuriku Natl. Agric. Exp. Stn*, **32**, 43-64 (in Japanese with English abstract).

Suizu S. (2001): A snowmelt and water equivalent of snow model based on a simplified heat balance method. *Journal of the Japanese Society of Snow and Ice*, **63** (3), 307-318 (in Japanese with English abstract).

Suizu S. (2002): A snowmelt and water equivalent snow model applicable to an extensive area. *Journal of the Japanese Society of Snow and Ice*, **64** (6), 617-630 (in Japanese with English abstract).

Takahashi Y., Koike T. and Tahara I. (1987): Synthesizing the model for estimation of basin-wide snow water equivalent using LANDSAT data. *Proceedings of the Japanese Conference on Hydraulics*, **31**, 227-232. (in Japanese with English abstract)

Tanakamaru H and Kadoya M. (1994): Runoff and water budget characteristics of reclaimed farm land - Effects of land reclamation on hydrological cycle (I) -. *Trans. of JSIDRE*, 91-97 (in Japanese with English abstract).

Tanakamaru H and Kadoya M. (1994): Examination of runoff characteristics of reclaimed farm land by long and short terms runoff model - Effects of land reclamation on hydrological cycle (II) -. *Trans. of JSIDRE*, 99-105 (in Japanese with English abstract).

Taniguchi T., Masumoto T., Shimizu K., Horikawa N. and Yoshida T. (2009): Development of a distributed water circulation model incorporating various paddy water uses, Part 1: A model for estimating cropping pattern and area. *J. Japan Soc. Hydrol. and Water Resour*., **22** (2), 101-113 (in Japanese with English abstract).

Taniguchi T., Masumoto T., Horikawa N., Shimizu K. and Yoshida T. (2009): Development of a distributed water circulation model incorporating various paddy water uses, Part 2: Estimation of water requirements on the basis of classification of paddy water use and water management. *J. Japan Soc. Hydrol. and Water Resour*., **22** (2), 114-125 (in Japanese with English abstract).

Taniguchi T., Masumoto T., Yoshida T., Horikawa N. and Shimizu K. (2009): Development of a distributed water circulation model incorporating various paddy water uses, Part 3: Structure of the total model and estimation of agricultural water circulation. *J. Japan Soc. Hydrol. and Water Resour*., **22** (2), 126-140 (in Japanese with English abstract).

Tanji H. and Oonishi R. (1986): Improved water management of agricultural facilities in Iwaki river basin - Water balance analysis aimed at improved water management. *Bull. Nat. Res. Inst. Agric, Eng. Japan*, 93-151 (in Japanese with English abstract).

Yamazaki, D., Kanae, S., Kim, H. and Oki, T. (2011) : A physically based description of floodplain inundation dynamics in a global river routing modell, *Water Resources Research*, **47**, W04501, doi:10.1029/2010WR009726.

Yamazaki T., Taguchi B. and Kondo J. (1994): Estimation of the heat balance in a small snow-covered forested catchment basin. *TENKI*, **41** (2), 71-77.

Yokoyama K. (2000): Snow in the Hokuriku region under global climate change. *Hokuriku Crop Science*, **35**, 73-74 (in Japanese with English abstract).

Yokoyama K., Ohno H., Kominami Y., Inoue S. and Kawakata T. (2003): Performance of Japanese precipitation gauges in winter. *Journal of the Japanese Society of Snow and Ice*, **65** (3), 303-316 (in Japanese with English abstract).

Yoshida S., Takaki K., Adachi K. and Masumoto T. (1997): Change of soil physical properties in abandoned paddies under the alternating meteorological condition. *Trans. of JSIDRE*, **65** (5), 655-663 (in Japanese with English abstract).

(Following references are available only in Japanese)

Earth Remote Sensing Data Analysis Center (2008): 資源•環境観測解析センター，Aster　全球 3　次元地形データ，オンライン，入手先<http://gds.aster.ersdac.jspacesystems.or.jp/gds www2002/indexj.html>.

Hayase (1992): 早瀬吉雄，中山間水田域の洪水防止評価，応用水文，**4**，81-99.

Hokuriku Regional Agricultural Administration (1984): 北陸農政局関川農業水利事業所，事業誌関川，渡辺印刷所.

Hokuriku Regional Agricultural Administration Office (2006): 北陸農政局農村計画部資源課，多面的機能維持増進調査報告書東頸城地区.

Japanese Agricultural System Society (2007): システム農学会，農業リモートセンシング•ハンドブック，佐藤印刷.

Japan Institute for Irrigation and Drainage (2010): 日本水土総合研究所（参照2010.5.13）：日本水土図鑑（オンライン），入手先<http://www.nngis.jp/>.

Japan Meteorological Agency (2003): 気象庁観測部，メッシュ気候値2000，測候時報，2003.

Japanese Society of Snow and Ice (1990): 日本雪氷学会（1990）：雪氷辞典，古今書院，p.71.

Kadoya (1980): 角屋睦(1980):流出解析法（その 6 ）　－雨水流法–表面流出モデルによる洪水流出解析－，農業土木学会誌，**48**(6)，419-425.

Koide (1973): 小出博，日本の国土: 自然と開発（下），東京大学出版会.

Kondo (1994): 近藤純正，水環境の気象学: 地表面の水収支・熱収支，朝倉書店，1994.

Maruyama et al.(1979): 丸山利輔，富田正彦，小林慎太郎，複合タンクモデルによる広域水収支解析－1－複合タンクモデルの特徴とその構成，農業土木学会誌，**47**(2)，97-102.

Motoya (2008): 本谷研,東北地方における積雪水量の27 年平均値と豪雪•寡雪，日本雪氷協會雜誌，**70**(6)，561-570.

Niigata Prefecture (1985): 新潟県，笹ケ峰ダム管理規程新潟県訓令第 1 号，オンライン，1985，入手先 <http://www1.greiki.net/niigataken/reiki honbun/ae40107311.html>.

Niigata University (1987): 新潟大学東頸城地域地質調査グループ，新潟県東頸城地域の中新–鮮新統の層序，地球科学，**41** (3)，165-181.

Okamoto (1973): 岡本雅美，水田農業用水の計画需要量の推定法，水利科学，**17** (2)，54-65.

Ono et al. (1994): 小野延雄，石川信敬，新井正，若土正暁，青田昌秋，雪氷水文現象，基礎雪氷学講座 VI，古今書院.

Shinzawa (1962): 新沢嘉芽統，河川水利調整論，岩波書店.

Takahashi (2007): 高橋俊二（2007）：日本の天候の特徴，"本田明治，楠昌司編著，2005/06　日本の寒冬•豪雪"，日本気象学会，p.3.

Takeuchi (1974): 竹内常行，棚田の水利–頸城丘陵と猿ヶ石川下流部丘陵地の棚田を例として，早稲田大学教育学部学術研究 地理学・歴史学・社会科学編，23，1-24.

Tomita et al. (1979): 富田正彦，小林慎太郎，丸山利輔,複合タンクモデルによる広域水収支解析－2－複合タンクモデルの運用， 農業土木学会誌，47，No. 3，189-194，1979.

Yokoyama (2006): 横山宏太郎（2006）：平成18 年豪雪:上越地方の雪と農業への影響，雪氷，**68**，323-325.

Yokoyama (2007): 横山宏太郎，小南靖弘，中野聡史，宮崎伸夫，水津重雄. 上越地方の山地積雪2006 冬と2007 冬，雪氷北信越，**27**，69.

水田灌漑卓越流域の水循環モデル開発に関する研究

吉田武郎

　日本における農業用取水量は河川からの全取水量の約7割に相当し，河川の流況を決定づける要因の一つに挙げられる．本研究では，灌漑水田における人為的な水循環系を表現し，流域の自然的水循環と一体的に解析する流域スケールの分布型水循環モデルを開発した．開発したモデルにより，ダムの貯水量，各施設の取水量の推定や，水田灌漑の人為的な取水・還元に起因する河川流量の変化を定量的な評価ができることを示した．また，耕作放棄に伴って湿潤時にピーク流出量が増大することを観測から明らかにするとともに，耕作放棄水田の物理特性をモデルに反映させることで，観測された流出の変化をモデルで再現できることを示した．さらに，積雪・融雪，氾濫・湛水過程をモデルで同時に計算する手法を構築し，開発したモデルを水田が広く分布するアジアモンスーン地帯の多様な水文特性の流域へ適用可能にした．構築した一連のモデルにより，水田地帯の人為的な水循環が流域スケールの水循環に及ぼす影響を定量的に評価することができ，流域を取り巻く自然的・社会的条件の変化が水資源の脆弱性や洪水危険度に及ぼす影響評価に有用である．

　キーワード：流域水循環，分布型水文モデル，水田灌漑，水資源，土地利用